REPORT DOCUMENTATION PAGE

Public reporting burden for this collection of information is estimated to average 1 hour per response, including the time for reviewing instructions, searching existing data sources, gathering and maintaining the data needed, and completing and reviewing the collection of information. Send comments regarding this burden estimate or any other aspect of this collection of information, including suggestions for reducing this burden, to Washington Headquarters Services, Directorate for Information Operations and Reports, 1215 Jefferson Davis Highway, Suite 1204, Arlington, VA 22202-4302, and to the Office of Management and Budget, Paperwork Reduction Project (0704-0188), Washington, DC 20503.

1. AGENCY USE ONLY *(Leave blank)*	2. REPORT DATE 10 Jul 97	3. REPORT TYPE AND DATES COVERED

4. TITLE AND SUBTITLE
SPECTRAL SIGNATURE OF THE EARTH'S NIGHT AIRGLOW OBSERVED
FROM THE SPACE SHUTTLE

5. FUNDING NUMBERS

6. AUTHOR(S)
PAUL JOHN BELLAIRE JR

7. PERFORMING ORGANIZATION NAME(S) AND ADDRESS(ES)
UNIVERSITY OF ARIZONA

8. PERFORMING ORGANIZATION REPORT NUMBER

97-017D

9. SPONSORING/MONITORING AGENCY NAME(S) AND ADDRESS(ES)
DEPARTMENT OF THE AIR FORCE
AFIT/CI
2950 P STREET
WRIGHT-PATTERSON AFB OH 45433-7765

10. SPONSORING/MONITORING AGENCY REPORT NUMBER

11. SUPPLEMENTARY NOTES

12a. DISTRIBUTION AVAILABILITY STATEMENT

DISTRIBUTION STATEMENT A

Approved for public release;
Distribution Unlimited

12b. DISTRIBUTION CODE

13. ABSTRACT *(Maximum 200 words)*

19970716 137

DTIC QUALITY INSPECTED 3

14. SUBJECT TERMS

15. NUMBER OF PAGES
220

16. PRICE CODE

17. SECURITY CLASSIFICATION OF REPORT	18. SECURITY CLASSIFICATION OF THIS PAGE	19. SECURITY CLASSIFICATION OF ABSTRACT	20. LIMITATION OF ABSTRACT

SPECTRAL SIGNATURES OF THE EARTH'S NIGHT AIRGLOW
OBSERVED FROM THE SPACE SHUTTLE

by

Paul John Bellaire Jr.

_____

A Dissertation Submitted to the Faculty of the

DEPARTMENT OF ATMOSPHERIC SCIENCES

In Partial Fulfillment of the Requirements
For the Degree of

DOCTOR OF PHILOSOPHY

In the Graduate College

THE UNIVERSITY OF ARIZONA

1 9 9 7

THE UNIVERSITY OF ARIZONA ®
GRADUATE COLLEGE

As members of the Final Examination Committee, we certify that we have

read the dissertation prepared by Paul John Bellaire Jr.

entitled SPECTRAL SIGNATURES OF THE EARTH'S NIGHT AIRGLOW

OBSERVED FROM THE SPACE SHUTTLE

and recommend that it be accepted as fulfilling the dissertation

requirement for the Degree of Doctor of Philosophy

Dr. A. Lyle Broadfoot	6/25/97 Date
Dr. Donald M. Hunten	6/25/97 Date
Dr. E. Philip Krider	6/25/97 Date
Dr. Nilton O. Renno	6/25/97 Date
Dr. William D. Sellers	6/25/97 Date

Final approval and acceptance of this dissertation is contingent upon
the candidate's submission of the final copy of the dissertation to the
Graduate College.

I hereby certify that I have read this dissertation prepared under my
direction and recommend that it be accepted as fulfilling the dissertation
requirement.

Dissertation Director Dr. E. Philip Krider   6/25/97
                                                   Date

STATEMENT BY AUTHOR

This dissertation has been submitted in partial fulfillment of requirements for an advanced degree at the University of Arizona and is deposited in the University Library to be made available to borrowers under the rules of the Library.

Brief quotations from this dissertation are allowable without special permission, provided that accurate acknowledgment of the source is made. Requests for permission for extended quotation from or reproduction of this manuscript in whole or in part may be granted by the head of the major department or the Dean of the Graduate College, when in his or her judgment the proposed use of the material is in the best interests of scholarship. In all other instances, however, permission must be obtained from the author.

SIGNED: *Paul J. Bellaire Jr.*

ACKNOWLEDGMENTS

This work would not have been possible without the help of many. I will attempt here to provide recognition for those whose impact has been most immediate. For the others, my appreciation is just as deep and heartfelt.

Of course, without the LPL West spaceflight program and GLO instrument designed by Dr. A. Lyle Broadfoot, this manuscript would not exist! My many thanks for his guidance, advice, and efforts to keep me on the right track. Dr. Richard Schotland's assistance and direction are also deeply appreciated. He was a supportive influence when the "going got rough." Dr. Jeffrey Johnston, Dr. D. Brooke Hatfield, Dr. Emmet Anderson, Dr. Bill Sandel, Jesse Ramirez, Tom Stone, and Terry Forrester were all invaluable mentors and expert problem solvers. They were consistent and cheerful in providing "remedial tuition," computer systems support, answers to endless questions, moral support, and friendship when it was most needed. Thanks, guys -- see you on the next Shuttle mission! I give special thanks to Dr. Bill Bickel of the Department of Physics and his wife Barbara -- just for being themselves!

The support of faculty and staff at the Department of Atmospheric Sciences and LPL West was top notch. There are too many to thank individually, but you all know who you are. Surely the members of my Examining Committee deserve thanks for reading this heavy tome! You also have my gratitude.

My Air Force program managers deserve praise and commendation for their efforts to help me get through the tough times. My personal thanks and salute to Major Tom Neu and Captain James Ulman for jobs well done. Colonel Terence N. Thompson and his staff at USAF ROTC Detachment 20 also made me feel like a member of the team. I will take fond memories of my Air Force friends in Arizona to my next assignment in Washington D.C.

Dr. Cameron Dasch graciously provided his inversion model in Lotus spreadsheet form for use in this research. His assistance is gratefully noted.

Finally, my love and respect go to my wife, Major Mary L. Peters, for her support, forbearance, suffering, and fortitude throughout this long ordeal!

DEDICATION

Mankind looks up
Into the dark starry sky
Defiantly
And vows its children
Shall touch those stars

PJB, 1969

For "Molybdenum Mary" -- definitely several sigmas outside the norm!

TABLE OF CONTENTS

TABLE OF CONTENTS - *Continued*

LIST OF FIGURES

LIST OF FIGURES - *Continued*

LIST OF FIGURES - *Continued*

LIST OF FIGURES *- Continued*

LIST OF FIGURES - *Continued*

LIST OF TABLES

ABSTRACT

This research extends an observation program that recorded the night airglow from a Tucson ground station using an imaging spectrograph known as GLO. GLO was designed at the Lunar and Planetary Laboratory of the University of Arizona to observe auroral and airglow emissions, and recorded midlatitude airglow data near equinox during Space Shuttle mission STS-69 in September 1995.

GLO observations from the shuttle recorded the night airglow layer seen edge on at the Earth's limb. These observations from orbit exhibit a fundamentally different picture of the night airglow compared to observations from the ground. GLO data also represent the first simultaneous optical measurements of airglow emissions over the spectral range from 1150 to 9000 Å, showing global emission variations in the night sky. Intensity variations are not correlated among emitting species, implying greater dynamism and more complex chemical interactions in the airglow than previously assumed.

Although other researchers have described observations of organized waves and tides in the night airglow, these prior observations are sporadic or averaged over long time periods. The night sky intensity variations recorded by GLO do not exhibit any obvious relationship to atmospheric tides. They may instead be the result of a chaotic superposition of upward and downward vertical motions. This upwelling and subsidence may cause the decoupling of airglow emissions in the O_2 Atmospheric band, the OH Meinel band, and the atomic oxygen green line at 5577 Å. Emission enhancements with maxima-to-minima ratios of 4 to 12, depending on emitting species, have been observed in the GLO data. Emissions in the O_2 Atmospheric band system and the OI (5577 Å) green line show a greater dynamic range of variation than the OH Meinel band system. The chemistry along a limited line-of-sight can be explained by classical airglow chemistry, but only over a limited altitude range. Dynamic effects in the 80 to 100 km region are sufficiently chaotic to present mixed results when inferring chemical processes as a function of altitude.

RESEARCH OBJECTIVES

The Earth's mesosphere, thermosphere, and ionosphere (MTI) are coupled by a complex set of physical and chemical processes. Airglow emissions are a key signature of phenomena in the MTI region (from about 60 km up to several hundred km), and spectroscopic measurement of these emissions can constrain atmospheric models. Hydrodynamic waves have been predicted and described in detail for the MTI region and have been detected by ground-based and airborne observations. These waves include thermal tidal oscillations, planetary waves, and gravity waves. The global coverage provided by observations from orbit may help validate models describing gravity wave saturation and dissipation in the mesosphere. Such observations may also provide evidence of dynamic coupling between the E and F regions of the ionosphere, predicted by modelers but not yet unequivocally observed in the night airglow. From GLO observations, useful constraints to current chemistry models of the night airglow may also be inferred.

Objectives of this research include the identification and classification of atmospheric waves, if any, in the night airglow and the evaluation of airglow chemistry models by observing variations in night airglow emissions. Wave structure will be inferred directly from temporal and spatial intensity changes in the night airglow layer along the orbital track of the Shuttle. Chemistry model output will be compared to spectral signatures recorded by GLO under nearly solar minimum conditions for the O_2 Atmospheric $(0,0)$ and $(0,1)$ bands, the OH Meinel $(6,2)$ band, and the OI (5577 Å) green line, covering the altitude range from 65 to 125 km in the terrestrial night airglow.

The Johnston-Broadfoot night airglow model (Johnston and Broadfoot, 1993) will be used to predict vertical number density profiles for solar minimum conditions. This model utilizes vertical profiles of atmospheric constituents from the 1976 US Standard Atmosphere and seasonally averaged upper atmospheric models compiled in the Air Force Geophysics Laboratory's Handbook of Geophysics and Space Physics (1985). These profiles are consistent with those widely used by the aeronomy community (e.g, Hedin's 1987 MSIS model). Computer-assisted spectral analysis using

GLO observations of the Earth's limb will provide calibrated data for emitting species of interest. An Abel inversion algorithm for cylindrically symmetric geometry (Hassani, 1991; Dasch, 1992) will be used to infer volume emission rate profiles from observed integrated line-of-sight intensities in a simple spherical shell model of the atmosphere. These volume emission rate profiles are directly proportional to vertical density profiles for the emitting species in question. Inferred vertical density profiles will then be compared to the predictions of the Johnston-Broadfoot model. This procedure will help characterize the actual spatial and temporal behavior of atmospheric vertical structure, as well as improve the utility of the models.

Today's night airglow models have been developed primarily from ground-based observations, which have good temporal resolution but poor spatial resolution in the vertical. Top side observations from orbit have been sparse. Comparison of model output with profiles inferred from GLO data will either validate the model physics or suggest improvements to the theoretical descriptions. Airglow models include complex interrelated subroutines which calculate, for example, excitation rates for atomic and

molecular species, excited state production and transport, diffusion and temperature effects, number densities of excited species, and volume emission rates. The Johnston-Broadfoot model was developed at the University of Arizona and is available at LPL West. It is representative of most of the models in use today (Garcia and Solomon, 1983; Allen et al., 1984; Solomon et al., 1988; Rodrigo et al. 1986, 1991; Hedin, 1987, 1991; McDade, 1991; Mlynczak et al., 1993). Such models can only be refined and validated by considering data with the widest possible temporal, spatial, and spectral coverage.

1. INTRODUCTION

Until recently, models of the Earth's mesosphere, thermosphere, and ionosphere (MTI) have depended on observing airglow and auroral emissions, primarily using ground-based remote sensing, short-duration rocket flights, and a limited number of satellites. Such observations are limited in temporal, spatial, and spectral coverage. To address this difficulty, the National Science Foundation has created a program known as the Coupling, Energetics, and Dynamics of Atmospheric Regions (CEDAR). CEDAR is a key part of initiatives aimed at creating a global observation and modeling capability for the entire depth of the Earth's atmosphere. However, until permanent orbital platforms exist (such as the International Space Station) dedicated to such continuous global coverage, data collected on Space Shuttle flights can help to fill the gaps in our knowledge and improve our models.

Researchers at the University of Arizona's Lunar and Planetary Laboratory West (LPL West) have designed an imaging spectrograph that

useful for studying the MTI region from orbit. The Arizona Airglow Instrument (GLO) is a modified version of the Arizona Imager Spectrograph (AIS) previously built under contract to the U.S. Air Force (Broadfoot et al., 1992; Viereck et al., 1990). GLO has already flown on several Shuttle missions and additional flights are planned over the next few years. Some of the future missions will be augmented by coordinated ground-based observations under the CEDAR program. GLO data can be accessed by the CEDAR and space science communities via the Internet.

1.1 Historical Background

The history of aurora and airglow physics has been summarized by Chapman (1967). The aurora has been known since antiquity, but a scientific description distinguishing aurora from airglow is more recent. Ångström was the first to study the aurora's spectrum; in 1867, he found a prominent yellow-green line with a simple spectroscope, but did not accurately determine the wavelength. In 1901, Newcomb observed the faint non-auroral light of the night sky (the night airglow) and hypothesized the source to be multitudes of stars too dim to be seen. In 1913, Vegard identified bands of molecular nitrogen in auroral spectra that were also found to be characteristic of airglow spectra. The faint light of the night sky identified by Newcomb was studied further by Slipher, beginning in 1915 and for many years thereafter, at the Lowell Observatory in Flagstaff, Arizona. Babcock determined the 5577 Å wavelength of Ångström's prominent auroral yellow-green line in 1923. Using a Fabry-Perot interferometer, Babcock unknowingly observed the light of the airglow and *not* the aurora, as he had intended! In 1924, McLennan and Shrum proved that the 5577 Å line was caused by an

electronic transition between the metastable $^1D_2$ and $^1S_0$ levels of atomic oxygen. Slipher identified the red lines of atomic oxygen at 6300 Å and 6364 Å in airglow spectra, and also noted that the 5577 Å line was always present in such spectra. (The 6300 Å and 6364 Å lines are also prominent in auroral spectra and correspond to the $^1D_2$ to $^3P_1$ and $^1D_2$ to $^3P_1$ "forbidden" transitions, respectively). Observations of these three lines in both the aurora and airglow created some confusion initially. Researchers eventually distinguished airglow from auroral emissions using the fact that excitation potentials exhibited by airglow spectra were much smaller than those in auroral spectra. They established that the aurora was the result of more energetic processes than the airglow, but was otherwise very similar.

In 1931, the fourth Lord Rayleigh described the airglow as the "non-polar aurora." This terminology was gradually superseded by "airglow," first introduced by Elvey in the 1960's following a suggestion by Struve. The absolute intensity or surface brightness of the airglow 5577 Å line, expressed in millions of photons per second per column cross-sectional area (in cm^2)

along the line-of-sight, was first measured by Rayleigh in 1930. In his honor, the rayleigh (symbol R) has been adopted as the unit of sky brightness.

The airglow in the sunlit sky is referred to as the dayglow. In 1932, Dauvillier proposed that dayglow emissions are caused by a continuous flux of high-energy solar electrons (10^{10} eV) interacting with the Earth's atmosphere. Chapman's earlier theory of 1931, generally accepted today, states that airglow photons are emitted during recombination processes among electrons, ions, and dissociated atoms and molecules created by solar UV flux during the day. Airglows have also been observed in the atmospheres of other planets, including Mercury, Venus, Mars, and Jupiter, and perhaps recently even in the atmospheres of Jupiter's satellites.

In many cases, differentiating between the aurora and the dayglow is not a simple matter. A good but imperfect working definition (O'Brien et al., 1960) is: "If excitation results from direct bombardment by energetic charged *particles*, it is aurora. Otherwise, it is airglow." (The italics are mine). Thus, the aurora is primarily caused by energetic particles, while the dayglow is

mainly caused by the deposition of solar energy. In the dayglow, photoelectrons can compete with photoionization and UV photons, depending on the atmospheric constituent and the characteristic energies in question. On the other hand, the night airglow results from the chemical relaxation of the dayglow atmosphere when the solar influx is removed. Ultimately, the production of atomic oxygen by the photodissociation of molecular oxygen during the day is critical to creating the night airglow.

1.2. Daytime Chemistry

The following review is based primarily on the work of Tohmatsu (1990) and gives the background for the discussion of night airglow chemistry in the next section, as well as the Johnston-Broadfoot model outlined in Appendix F.

The photodissociation of molecular oxygen and ozone by daytime solar flux produces atomic oxygen, which persists after sunset and dominates the primary reactions in night airglow chemistry. Molecular oxygen is dissociated during the day by the absorption of solar radiation in the Herzberg continuum, the Schumann-Runge bands, and the Schumann-Runge continuum. As a result of this absorption, the following photochemical reactions ensue, creating various states of atomic oxygen (Tohmatsu, 1990; Chamberlain and Hunten, 1987):

- in the Herzberg continuum:

$O_2\ (X^3\Sigma_g\text{-}) + h\nu\ (\lambda < 2424\ \text{Å}) \rightarrow O\ (^3P_1) + O\ (^3P_1);$

- in the Schumann-Runge bands:
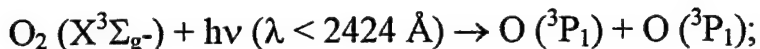
$O_2\ (X^3\Sigma_g\text{-}) + h\nu\ (1750\ \text{Å} < \lambda < 2060\ \text{Å}) \rightarrow O_2\ (B^3\Sigma_u\text{-},\ v') \rightarrow O\ (^3P_1) + O\ (^3P_1)$
for $v' \geq 2$ [v' are the vibrational levels];

- in the Schumann-Runge continuum:

$O_2\ (X^3\Sigma_g\text{-}) + h\nu\ (\lambda < 1750\ \text{Å}) \rightarrow O\ (^3P_1) + O\ (^1D_2).$
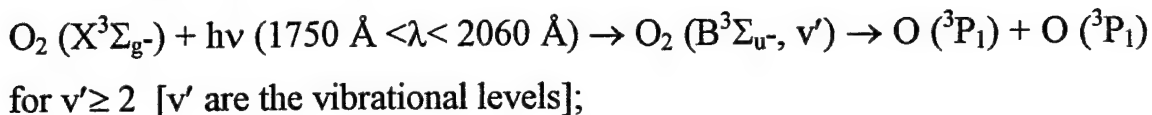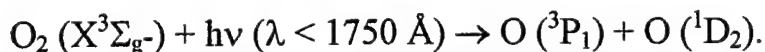
Weak absorption occurs in the Herzberg bands for $\lambda > 2424$ Å, corresponding to the forbidden transition $O_2\ (X^3\Sigma_g\text{-}) \rightarrow O_2\ (A^3\Sigma_u\text{+})$. The absorption cross section of O_2 in these bands is typically less than 10^{-24} cm^2. Since this absorption is not accompanied by dissociation, it is neglected.

Absorption in the Herzberg continuum is also weak. However, with O_2 abundance in our atmosphere being so high and this absorption occurring where the solar flux is large, the Herzberg continuum is the main source of atomic oxygen below 65 km altitude, where it is important in the formation of the ozone layer (Tohmatsu, 1990).

In the Schumann-Runge bands (1750 Å$<\lambda<$2060 Å), dissociation into atomic oxygen occurs for O_2 vibrational levels v′ greater than or equal to 2. This process is a prime source of atomic oxygen in the mesosphere at altitudes between 60 and 90 km.

The lower thermosphere absorbs almost all incoming solar flux between 1350 and 1750 Å in the Schumann-Runge continuum, at altitudes between 90 and 130 km. This absorption is the major source of atomic oxygen in the ionosphere. The atomic oxygen so produced is in an excited electronic state and plays a very important part in the chemistry of the neutral atmosphere at these altitudes. Less important is absorption by ozone in the Hartley continuum ($\lambda < 3100$ Å), producing excited states of atomic and molecular oxygen which participate in the chemistry of the mesosphere. Additionally, absorption of solar Lyman-α flux at 1216 Å causes about ten percent of the total O_2 dissociation between 70 and 90 km (Tohmatsu, 1990). The net effect of the processes described here is to establish an "atmospheric cutoff" near 3000 Å. All solar flux shortward of this wavelength is ultimately absorbed by the atmosphere.

1.3 Night Airglow Chemistry

Night airglow emissions at about 60 to 120 km altitude depend on the nighttime vertical distribution of chemically active atomic and molecular species established during the day. Atomic oxygen dominates the chemical reactions involving NO, NO_2, O_2, and OH that create the features of the night airglow spectrum, but the variability of atomic oxygen in the thermosphere has yet to be measured systematically. Ground state atomic oxygen, O ($^3P_1$), is generally believed to be the prime agent in creating the night airglow through its participation in three-body association reactions forming excited O_2 states. Atomic oxygen is created at altitude by photodissociation during the day and diffuses downward into the thermosphere and mesosphere, where it takes part in reactions with other species, such as OH and O_2. The chemical reactions coupled in the night airglow are schematically depicted in Figure 1.1 on page 30 (Johnston and Broadfoot, 1993).
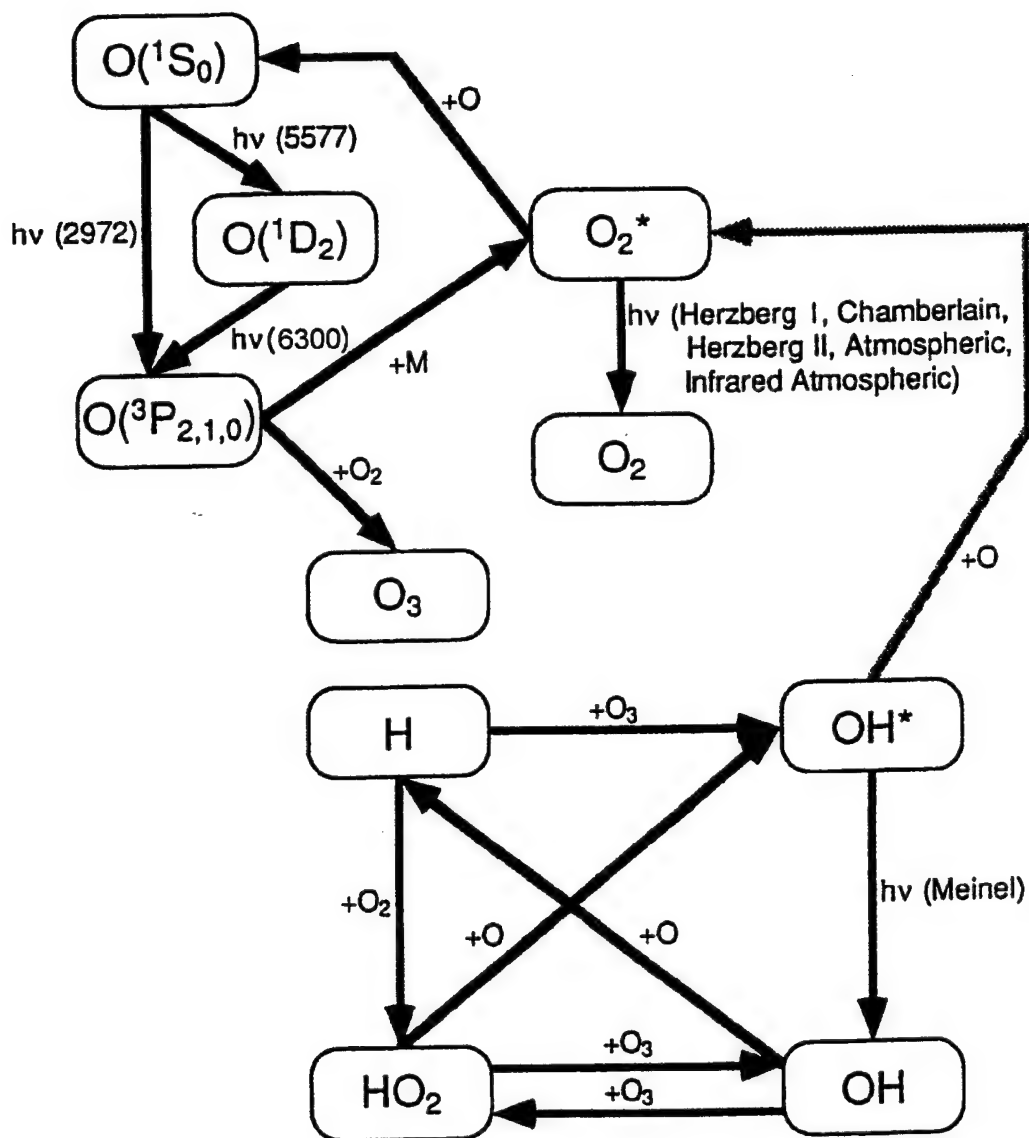
Figure 1.1. The chemistry of the night airglow.

The two-part Barth process creates the excited states of O and O_2 in the night airglow (Chamberlain and Hunten, 1987; Rees, 1989).

Step One of the Barth process is:

$$O\,(^3P_1) + O\,(^3P_1) + M \rightarrow O_2\,(c\,^1\Sigma_u\text{-},\ A'\,^3\Delta_u,\ A\,^3\Sigma_u\text{+},\ b\,^1\Sigma_g\text{+},\ a\,^1\Delta_g) + M,$$
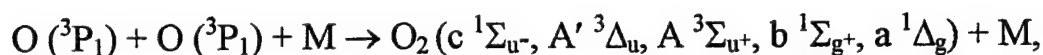
which is followed by Step Two:

$$O_2\,(c\,^1\Sigma_u\text{-}) + O\,(^3P_1) \rightarrow O_2\,(X\,^3\Sigma_g\text{-}) + O\,(^1S_0).$$
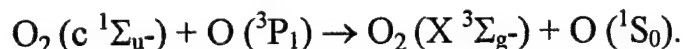
(Some losses of $O\,(^3P_1)$ to the O_3 and O_2 ground state occur; see Figure 1.1).

Step One creates the O_2 excited states, which then emit as follows:

$$O_2\,(A\,^3\Sigma_u\text{+}) \rightarrow O_2\,(X\,^3\Sigma_g\text{-}) + h\nu \ \text{(Herzberg I, 3000 Å} < \lambda < 5000 \text{ Å)};$$

$$O_2\,(c\,^1\Sigma_u\text{-}) \rightarrow O_2\,(X\,^3\Sigma_g\text{-}) + h\nu \ \text{(Herzberg II, 3000 Å} < \lambda < 5000 \text{ Å)};$$

$$O_2\,(A'\,^3\Delta_u) \rightarrow O_2\,(X\,^3\Sigma_g\text{-}) + h\nu \ \text{(Herzberg III, 3000 Å} < \lambda < 5000 \text{ Å)};$$

$$O_2\,(b\,^1\Sigma_g\text{+}) \rightarrow O_2\,(X\,^3\Sigma_g\text{-}) + h\nu \ \text{(Atmospheric, } \lambda > 7600 \text{ Å)};$$

$$O_2\,(a\,^1\Delta_g) \rightarrow O_2\,(X\,^3\Sigma_g\text{-}) + h\nu \ \text{(IR Atmospheric, } \lambda > 1 \ \mu m)};$$

$$O_2\,(A'\,^3\Delta_u) \rightarrow O_2\,(a\,^1\Delta_g) + h\nu \ \text{(Chamberlain, 3300 Å} < \lambda < 4400 \text{ Å)}.$$
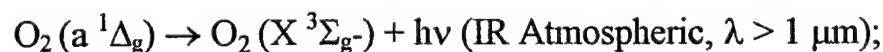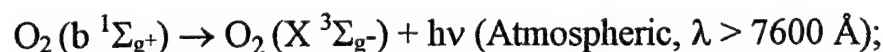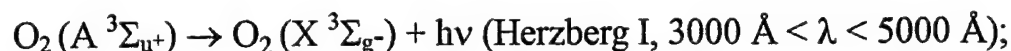
Step Two is quickly followed by the reactions

$O(^1S_0) \rightarrow O\ (^1D_2) + h\nu\ (5577\ \text{Å})$ and $O(^1S_0) \rightarrow O\ (^3P_1) + h\nu\ (2972\ \text{Å})$.
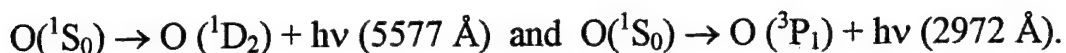
The metastable transition $O\ (^1D_2) \rightarrow O\ (^3P_1) + h\nu\ (6300\ \text{Å})$ is possible, but strongly quenched at altitudes below 200 km due to its long radiative lifetime of 110 seconds (Rees, 1989). The 6300 Å emission is insignificant in the airglow layer at 100 km.

Ozone chemistry dominates the night sky's OH Meinel band emissions (which are caused by vibrational transitions in the ground electronic state of the OH radical):

$$H + O_3 \rightarrow OH\ (X\ ^2\Pi_{3/2,1/2},\ v' \leq 9) + O_2 + 3.3\ \text{eV}.$$
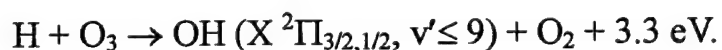
This vibrational excitation is followed by the reaction:

$OH\ (X\ ^2\Pi_{3/2,1/2},\ v' \leq 9) \rightarrow OH\ (X\ ^2\Pi_{3/2,1/2}) + h\nu\ (\text{Meinel},\ 5000\ \text{Å} < \lambda < 4\ \mu m)$.

No OH vibrational band emissions from levels above $v'=9$ are observed in the night airglow (Rees, 1989). The rotational intensity distribution of the OH Meinel system can be used as a measure of mesopause temperature and its

variability, but the vibrational distribution of this system is not yet fully quantified.

The Johnston-Broadfoot model simulates night airglow chemistry from 60 to 120 km altitude, dividing the atmosphere into 30 finite plane-parallel layers, each of 2 km depth, and using a time step of 300 seconds (Johnston and Broadfoot, 1993). Each layer is homogeneous with a constant particle number density for the major constituents O_2 and N_2, based on the assumption of negligible diurnal variation of these constituents at the altitudes in question (Rodrigo et al., 1991). Output consists of vertical number density profiles, integrated vertical column densities, and altitudes of peak emission for the lines and bands of O_2, OH, and the various species of O (Johnston, 1992).

The number densities of the minor constituents are calculated using the equation of continuity:

$$\frac{\partial N_i}{\partial t} = -\frac{\partial}{\partial z}(N_i w_i) + P(N_i) - L(N_i),$$

where the number density of the minor constituent is N_i, the chemical production and loss terms for the minor constituent are $P(N_i)$ and $L(N_i)$, respectively, t is time, z is altitude, and the term $\partial/\partial z\ (N_i\ w_i)$ represents diffusion. The upward diffusion velocity w_i of a minor constituent is given by

$$w_i = -D\left(\frac{1}{N_i}\frac{\partial N_i}{\partial z} + \frac{M_i g}{kT} + \frac{1}{T}\frac{\partial T}{\partial z}\right) - K\left(\frac{N_i}{N}\frac{\partial}{\partial z}\left[\frac{N_i}{N}\right]\right),$$

where D and K are the molecular and eddy diffusion coefficients, respectively, T is temperature, k is Boltzmann's constant, M_i is the molecular or atomic mass of the minor constituent, z is altitude, g is the acceleration of gravity, and the number densities of the major and minor constituents are N and N_i, respectively (Johnston, 1992).

In summary, dissociation provides the atomic oxygen needed to form excited states of O_2, which in turn help create the excited state O ($^1S_0$). In the night airglow, the excited states of O_2 emit in the Herzberg, Atmospheric, and Chamberlain bands, while the excited state of atomic oxygen, O ($^1S_0$), emits at 2972 Å and 5577 Å. It is noteworthy that all these emissions of the night

sky are measured simultaneously by GLO (see Figure 1.2). The OH radical

reacts with atomic oxygen to form O_2, and this product is cycled to create

ozone. Since ozone is formed in the three-body association $O + O_2 + M \rightarrow$

$O_3 + M$, OH exists in a complex balance with ozone creation and destruction,

mediated by the presence of H, HO_2, O, and O_2. Quenching dominates the

rotational and vibrational distributions of night airglow species and has been

qualitatively modeled. However, a *quantitative* description is still lacking.

The Johnston-Broadfoot model is among the best models yet available to

simulate the complex chemistry of the night airglow.

1.4 Recent Observations

Weill (1967) summarized the early history of ground-based airglow observations in equatorial regions, which had already established the existence of an equatorial minimum in 5577 Å emission and seasonal variations in sodium and OH emissions. Many other researchers in the last twenty years have described latitudinal variations in the 5577 Å emission of atomic oxygen inferred from both ground-based and satellite observations. Brenton and Silverman (1970) and Takahashi et al. (1989) described strong midnight minima in 5577 Å emission measured from ground stations in equatorial South America. In the 1970s, Donahue et al. (1973) and Reed and Chandra (1975) found deep equatorial minima in 5577 Å emission from their analyses of data taken by the OGO series of satellites. Cogger and Khaneja (1979) also reported a persistent equatorial minimum in 5577 Å emission inferred from data collected by the ISIS-2 satellite. Using observations of the 5577 Å emission from the Atmospheric Explorer satellite, Yee and Abreu (1987) found a post-local sunset emission maximum and a post-local midnight minimum for latitudes within 20° of the equator in the spring, and they

inferred these effects were connected to atmospheric tides. Modelers, such as Akmaev and Shved (1980) and Forbes et al. (1993), have seen that diurnal and semidiurnal atmospheric tides can create variations by factors of 4 or more in 5577 Å emission and induce atomic oxygen density reductions on the order of 30% at airglow altitudes.

Observations from the Upper Atmosphere Research Satellite (UARS) in the last few years have provided interesting clues to the nature of the night airglow. Shepherd et al. (1995a; 1995b) and Ward et al. (1995) have used the Wind Imaging Interferometer (WINDII) on UARS to observe nightglow emissions in 5577 Å and the O_2 Atmospheric band. They infer vertical motions in the MTI region and spatial variability in the two emissions. These UARS researchers believe their data indicate that the two emissions are well correlated in space and time (Ward et al., 1995). They also intend to report findings for the OH Meinel band in the near future.

The persistent emissions of the night sky that dominate this study are the O_2 Atmospheric bands, the OH Meinel bands, and the OI (5577 Å) line of

atomic oxygen. Figure 1.2 shows the averaged night airglow spectrum obtained by the GLO instrument during Space Shuttle mission STS-53 in December 1992. Note that the complete spectral range shown was recorded *simultaneously* by the GLO spectrographs.

The GLO experiment described in the following chapters observed emission intensity variations and signatures of vertical motions in the night airglow. These signatures were recorded simultaneously in O_2 (0,0), O_2 (0,1), O_2 Herzberg, O_2 Chamberlain, OI 5577 Å, and OH Meinel emissions between 28.4° N and 28.4° S (geocentric latitude) under equinox conditions. In contrast with the conclusions of UARS researchers, the GLO data exhibit a distinct lack of clear correlation among night sky emissions.

Advances in detector and computer technology in the last decade have made comprehensive observations of the night sky possible. The night airglow spectrum by Broadfoot and Kendall (1968) required over 180 hours of exposure using a ground-based spectrograph. Their spectrum has remained the definitive standard for the aeronomy community, but the current version of
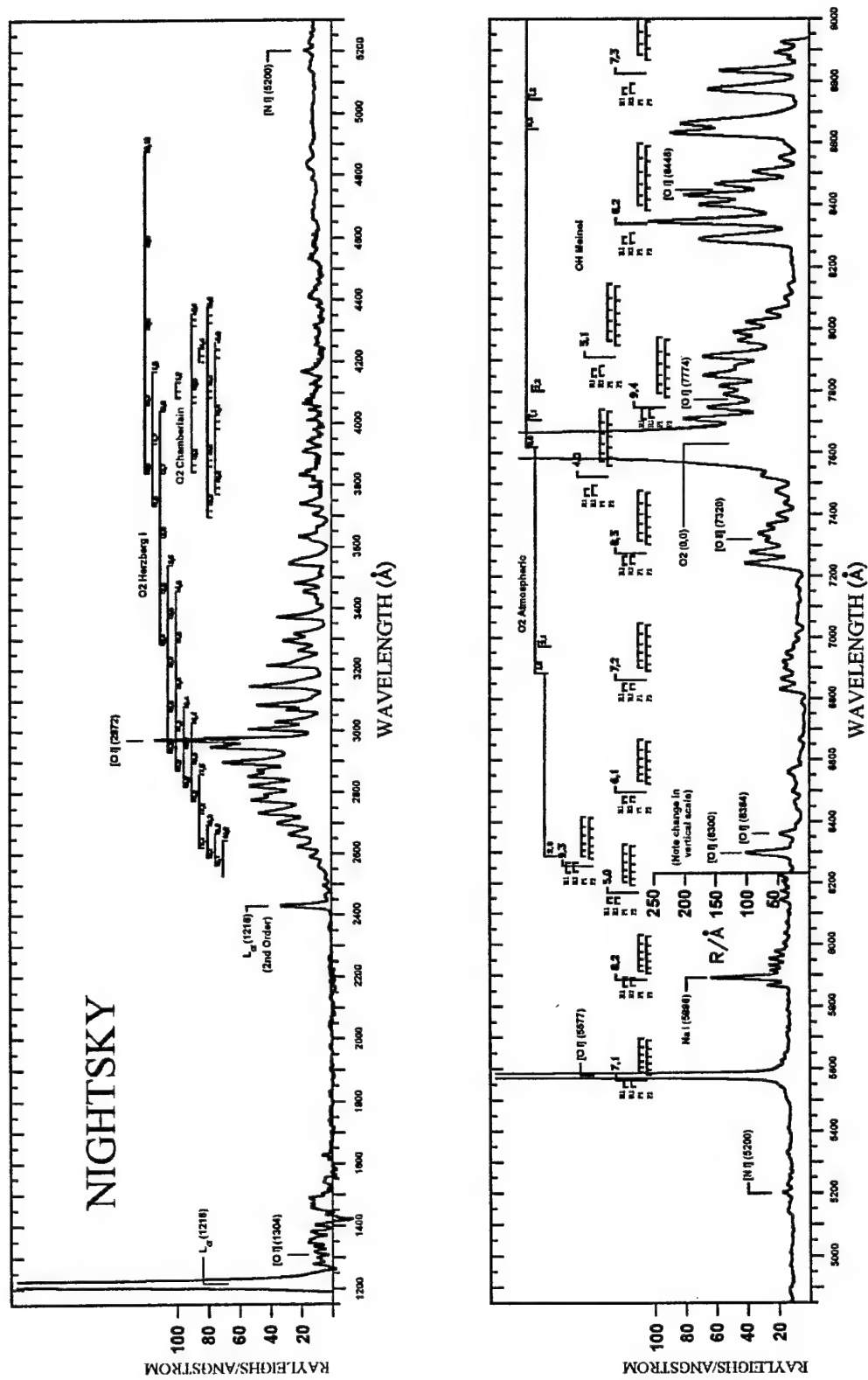
Figure 1.2. The night sky spectrum as recorded by the Arizona Imaging Spectrograph (GLO) on STS-53.

the GLO instrument can produce an airglow spectrum comparable to Broadfoot and Kendall's product in about 10 to 15 minutes! We are only beginning to systematically study the night sky from the "top side" with such a capability. No previous study has been able to accumulate continuous and simultaneous observations of the various airglow emissions on a global scale.

The data used in this research were obtained during Space Shuttle mission STS-69, which was launched on 7 September 1995 and remained on orbit for nearly 11 days. The orbital geometry of STS-69 was particularly useful for low latitude night airglow studies (Figure 1.3), and provided a nearly constant observation geometry for about 39 orbits (orbits 66 through 104) during solar minimum and under nearly equinox conditions. Figure 1.4 shows representative nighttime orbit tracks (71 through 80) to indicate STS-69 observational coverage. Note that each orbit track is 22.5° further west (for a separation of about 2500 km at 100 km altitude) than the track that preceded it, and proceeds from the southwest toward the northeast during a night pass.

LPL Arizona · **GLO Experiment** · *Unique Conditions on Each Flight* · **Phillips Lab USAF**

STS-69

Launched September 1995

Inclination: 28.4°

Altitude: 400 km
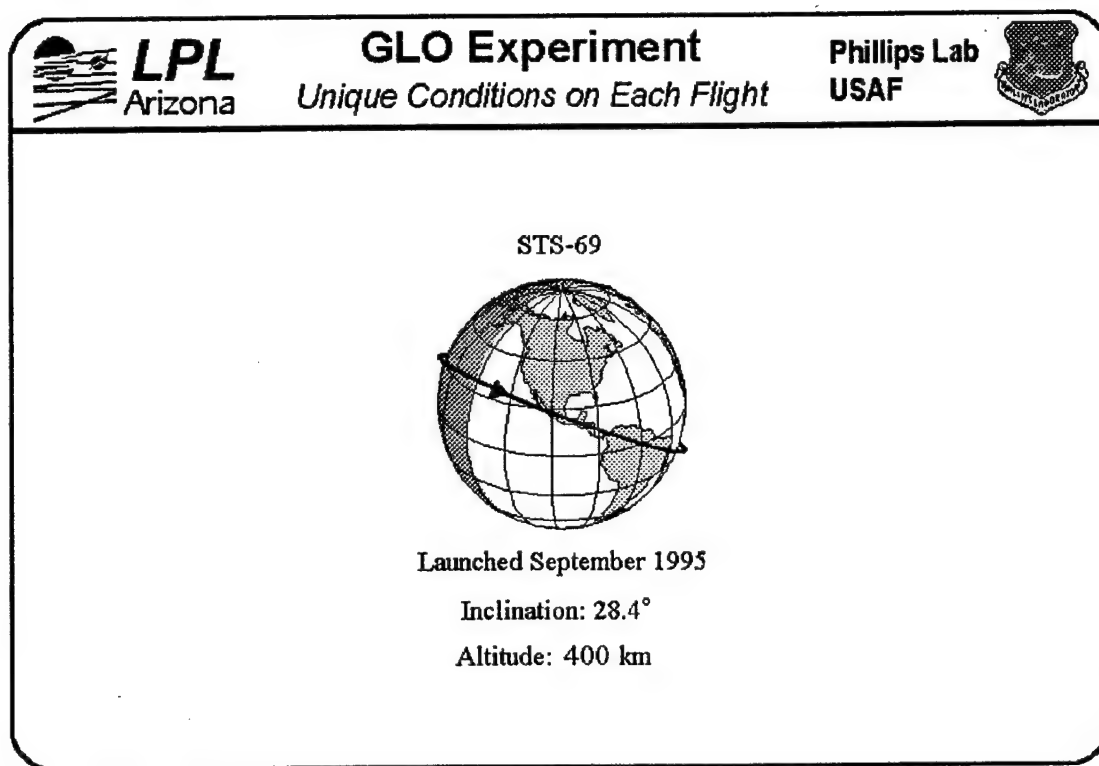
Figure 1.3. Orbital geometry for Space Shuttle flight STS-69.
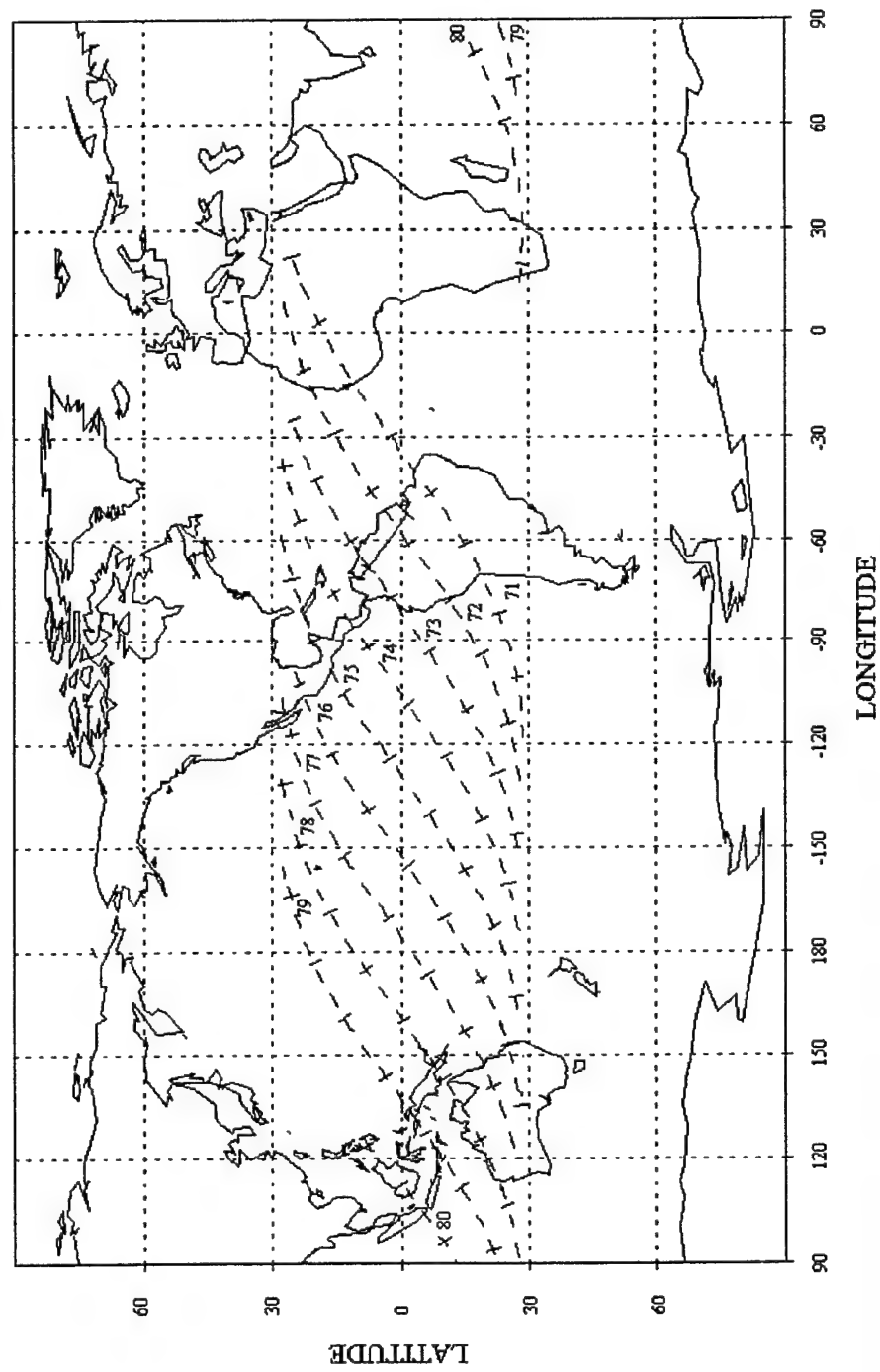
Figure 1.4. Representative orbital tracks for Space Shuttle flight STS-69.

2. THE GLO EXPERIMENT ON STS-69

The GLO instrument was designed to observe weak emissions, including aurora and airglow, from the Space Shuttle and satellites (Broadfoot and Sandel, 1992; Broadfoot, et al., 1992). On the fourth day of Mission Elapsed Time (MET) for STS-69, the Space Shuttle began an experiment which required a constant attitude for the next 40 orbits. The LPL West science team took this opportunity to continuously observe the Earth's limb. The GLO experiment proceeded for 39 orbits (orbits 66 through 104), and the night airglow data recorded for that period are examined in this research.

The pointing of the GLO instrument and the stability of the Space Shuttle platform are key to quantifying this data set. GLO can be pointed with an accuracy of $\pm0.005°$. GLO tracking errors and shuttle axes drifts contribute to altitude errors along the line-of-sight. Knowledge of the GLO observational geometry, the shuttle's attitude in space, and the pointing accuracy of the GLO instrument is necessary before the data recorded on STS-69 can be analyzed with confidence.

2.1 Overview of the GLO Instrument
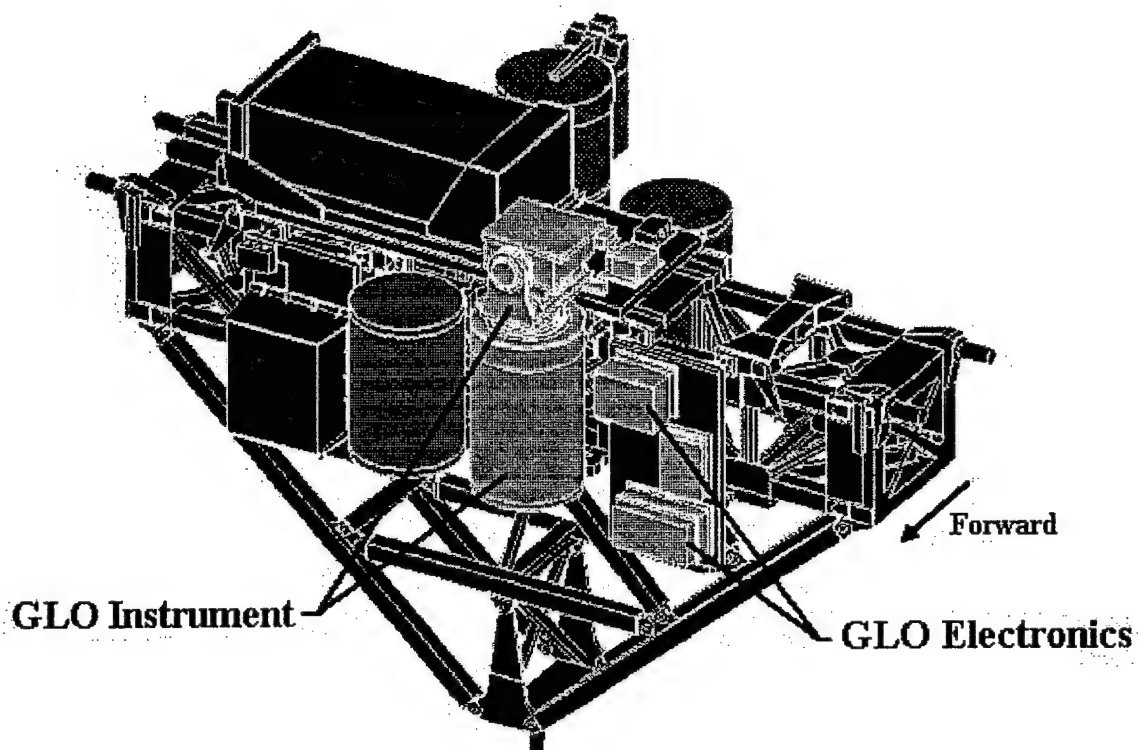
Figure 2.1. STS-69 payload bridge installed in the shuttle bay.

GLO spectrographs and imagers are housed in a sensor head that is mounted on a motor-driven scan platform, permitting motion of sensor boresight in elevation (EL) and azimuth (AZ) relative to the mounting surface of the spacecraft. The two stepping motors provide rotation in AZ and EL by

turning worm gears. The rate of sensor head movement in azimuth is 3° per second with 0.0082° resolution, and in elevation, 3° per second with 0.014° resolution. The total range of sensor head motion is -60° to +135° in elevation and -175° to +175° in azimuth from a predefined zero position.

Because of the fit of the worm gear, a "backlash," or position error, occurs whenever the stepping motors reverse direction. Backlash control compensates for this by positioning the scan platform by unidirectional rotation in the positive sense. For each commanded rotation in the negative sense, the platform is overdriven by an additional 0.5° rotation, followed by a positive rotation of 0.5° before stopping.

The GLO sensor head consists of nine spectrograph channels, as well as three imagers with coaligned optical axes. The GLO instrument has been previously described in detail by Broadfoot et al. (1992). GLO imager configuration for STS-69 was changed somewhat from that description, but the spectrographs remain the same (see Appendix A). GLO records airglow emissions using intensified charge coupled devices (ICCDs) as detectors in

the spectrographs. The application of ICCDs to instrumentation for observing the airglow has been outlined by Broadfoot and Sandel (1992). The spectrographs are paired so that two gratings are illuminated by a single entrance slit. The spectra from adjoining spectral regions are dispersed side-by-side onto a single ICCD. The nine gratings have spherically concave surfaces that have been holographically ruled to correct aberrations and provide a slit image on the flat ICCD surface.

The ICCD spectrographs measure spatial, temporal, and spectral emission signatures at wavelengths from 1150 to 9000 Å. Spectrograph resolution in the short wavelength region is about 4 Å, while it is about 10 Å at the long wavelengths. GLO foreoptics give all spectrographs a field-of-view (FOV) of 8.5° by 0.15°, and permit the measurement of brightness variations in all airglow emissions simultaneously. Simultaneous observation is important for understanding the relationships among the emissions.

Spatial information is recorded along the length of the spectrograph slit. The ICCD digital "readout" is adjusted electronically to give 24

contiguous spatial elements or "superpixels" of 8 pixels each along the slit, per spectral image. An IR imager assisted the observational program by tracking the airglow layer as it was viewed edge-on at the Earth's limb.

For the purpose of identifying the nine spectral images, the spectrographs have been labeled as A through E, from the longest wavelength to the shortest. The spectral images are then numbered one through nine as outlined in Table 2.1.

SPECTROGRAPH	SPECTRAL IMAGE	SPECTRAL RANGE
A	1	9000-11000 Å
B	2	7500-9000 Å
	3	6000-7500 Å
C	4	5250-6000 Å
	5	4500-5250 Å
D	6	3750-4500 Å
	7	3000-3750 Å
E	8	2100-3000 Å
	9	1100-2100 Å

Table 2.1. GLO spectrograph and spectral image assignments.

For spectrograph A, a single grating covered the spectral range for channel 1. This spectrograph was not sensitive enough to produce useful data. The emissions of interest here were recorded by spectrographs B, C, and E. The ICCD in spectrograph D failed shortly after launch. Intensified imager data was not examined in this work. The unintensified IR imager was used to assist in spectrograph pointing. In our case, it was also used for tracking the airglow limb and for GLO boresight calibration.

Broadfoot and Sandel (1992) have described the advantages of ICCDs over bare CCDs, scanning monochromators, and Ebert-Fastie spectrometers. ICCDs maximize throughput over a broad spectral range and exhibit much lower detector noise compared to historical spectrometers. The small size of ICCDs permits much smaller instrumentation, even while allowing a broader spectral range to be simultaneously recorded. The reduction in instrument size is typically an order of magnitude, and this reduces the sensitivity to interior scattered light by the same factor. GLO spectrographs contain no moving parts, while spectrometers contain rotating gratings and stepping motors. Within a GLO spectrograph, the geometry of the optics and ICCD detector is

fixed, giving a well defined wavelength scale, whereas in a spectrometer, accuracy of wavelength determination is dependent on the precision of the internal stepping motor that drives the rotating diffraction grating. The reduction in the size of the foreoptics and detector element means the ICCD spectrograph in GLO can have a much smaller mass and volume than a comparably performing spectrometer, a significant advantage in a space flight instrument.

2.2 Observational Geometry

The night airglow is known to originate in relatively thin emitting layers with thicknesses on the order of 10 km. Therefore, it is important to determine where the GLO boresight is pointing when a spectral image is recorded. Figure 2.2 shows the airglow viewing geometry for a typical night pass. Observations were taken looking into the shuttle wake, opposite the direction of motion, with the slit tilted about 30° to the limb. The 24 spatial elements along the slit are depicted.
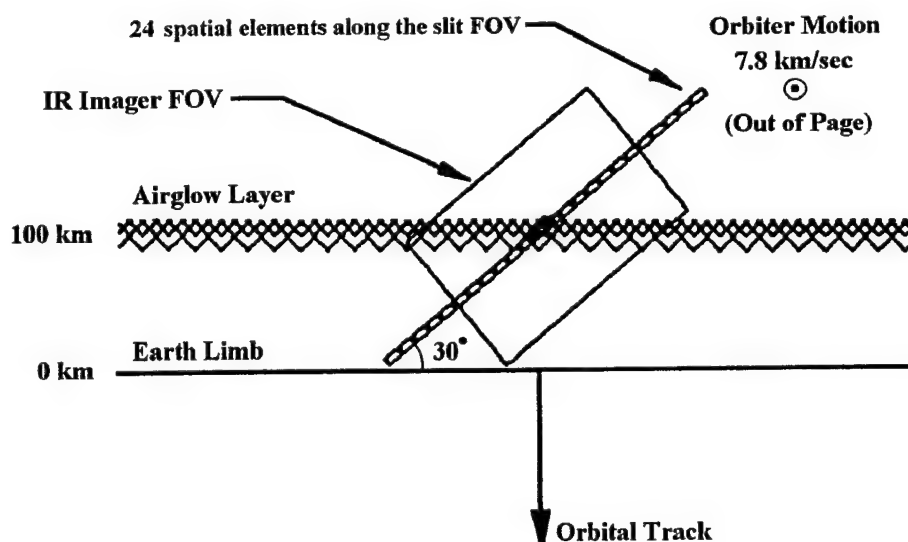
Figure 2.2. GLO airglow viewing geometry showing spectrograph slit and limb tracking imager Field Of View (FOV).

At a slant range of about 2000 km from the airglow layer, the field of view (FOV) of a spectrograph is about 296 by 5 km. The slit image has a length of 192 pixels on the ICCD and is divided into 24 subgroups (spatial elements or "superpixels") measuring 8 by 1 pixels (Figure 2.2). If the slit is tilted at an angle to the limb, vertical resolution when sampling the atmosphere is improved. At an angle of 10° to the horizontal and a slant range of 2000 km, a 51 km depth of the atmosphere is sampled. With a slit tilt of 30° and 2000 km slant range, GLO surveys a 148 km depth, while at 90°, a maximum altitude range of about 296 km can be imaged on the slit.

Resolution in the vertical depends on superpixel separation along the vertical dimension of the image. A horizontal slit will create no vertical separation for the spatial elements; this gives optimal signal strength, but only for a shallow layer about 5 km thick. Although vertical resolution cannot be smaller than the slit width (5 km at 2000 km slant range), signal strength is increased by minimizing the airglow depth over which the slit is imaged. A vertically oriented slit will provide maximum vertical spatial resolution, with each spatial element representing an altitude increment of about 12 km, but

since this covers a 296 km depth, signal strength at any given altitude is minimized. For the STS-69 altitude of 400 km, GLO slit tilt of 30°, and slant range to the tangent point of 2000 km, the vertical separation between the centers of spatial elements is about 6.8 km.

These factors show the importance of limb tracking of the airglow. Shuttle motions cause the spectrograph slit to sweep over the limb periodically by ±1° (±35 km at 2000 km slant range). The GLO limb tracker follows the brightest region of a strip through the imager FOV by moving the scan platform in AZ and EL, thus compensating for these motions. Limb tracking represents an important enhancement in GLO's capabilities.

Figure 2.3 shows the observation slant path across the Earth's limb to scale. Angular dimensions given are for the maximum vertical extent of the spectrograph and imager FOVs with the slit tilted at 30°. The dots along the airglow layer indicate imager exposures at 8 second intervals. Spectrograph exposures occurred at 20 second intervals, so there were two spectrograph exposures for every five dots indicated in the figure.
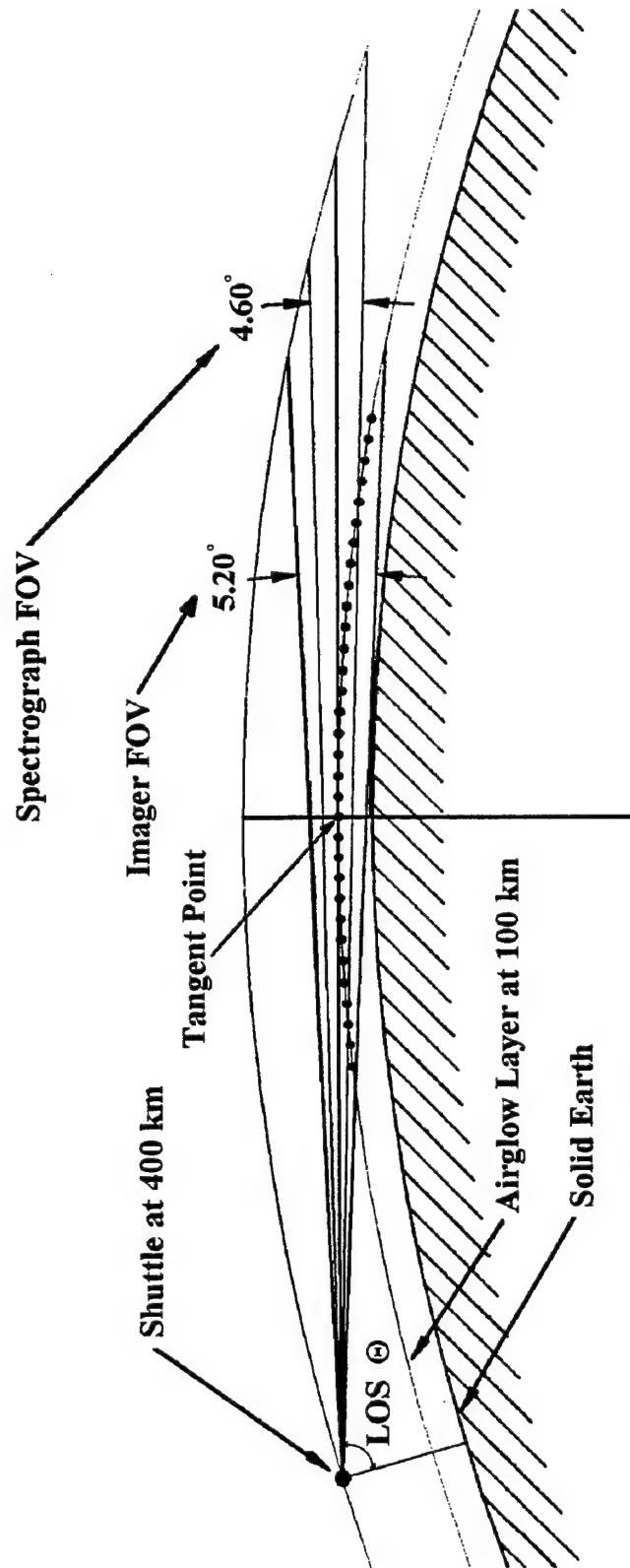
Figure 2.3. Fields-of-view for the GLO limb tracking imager and spectrographs with 30° slit tilt. Angular dimensions given are for maximum vertical extent with the tilted FOV. Dots along the airglow layer indicate spacing of IR imager exposures at 8 second intervals. Compare with Figure 2.4.

Figure 2.4 below shows a typical view of the night airglow layer using GLO's IR limb tracking imager.
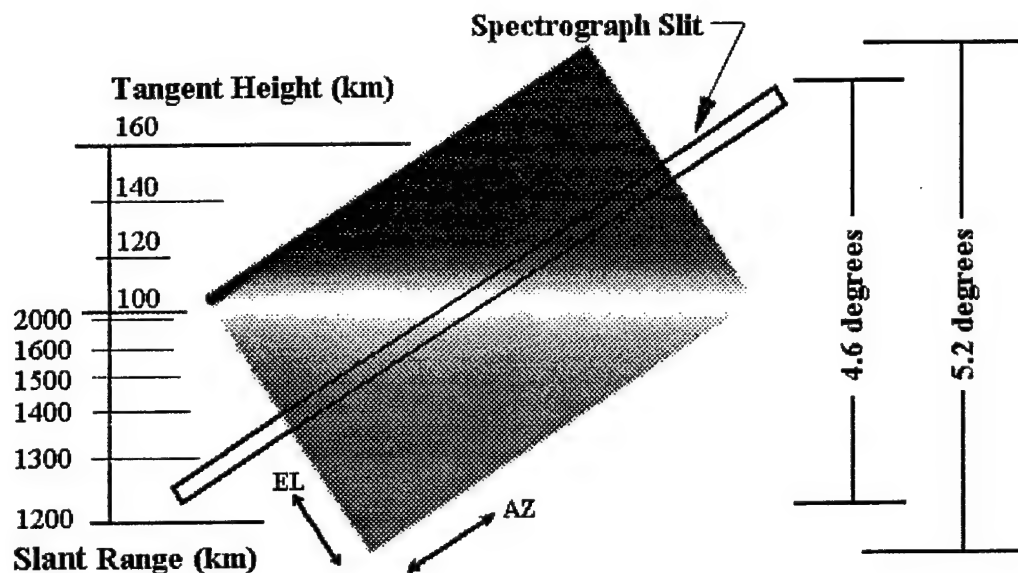
Figure 2.4. The night airglow in GLO's limb tracking imager. Tangent height, slant range, GLO AZ and EL, and vertical extent of the FOVs of the imager and spectrograph slit from STS-69 are indicated. A slit tilt of 30° is depicted. Compare with Figure 2.3.

The advantage of controlling the slit orientation is well illustrated by Figure 2.4. Note that half of the spectrograph slit is above the airglow layer and is therefore not collecting useful data. The optimum orientation would have had the topmost end of the slit just above the airglow layer. However, this first use of limb tracking by GLO required that the limb be near the center of the IR imager FOV. This will be modified for future flights.

The geometry used to collect this data set has been depicted in Figures 2.2 through 2.4. It is also important to understand the GLO coordinate system as depicted in Figure 2.5 on the next page. The GLO azimuth axis is along the "+Z" shuttle axis, where "-Z" points toward the velocity vector (see Figure 2.6 in the next section). Thus the azimuth axis points in the shuttle wake. The Earth limb seen from our 400 km altitude was depressed about 18° from this axis. Figure 2.5 shows that the slit, which is tangent to circles of constant elevation, can be oriented at any angle to the limb between 0° and 90° by the proper selection of GLO AZ and EL.

GLO AZ/EL COORDINATE SYSTEM
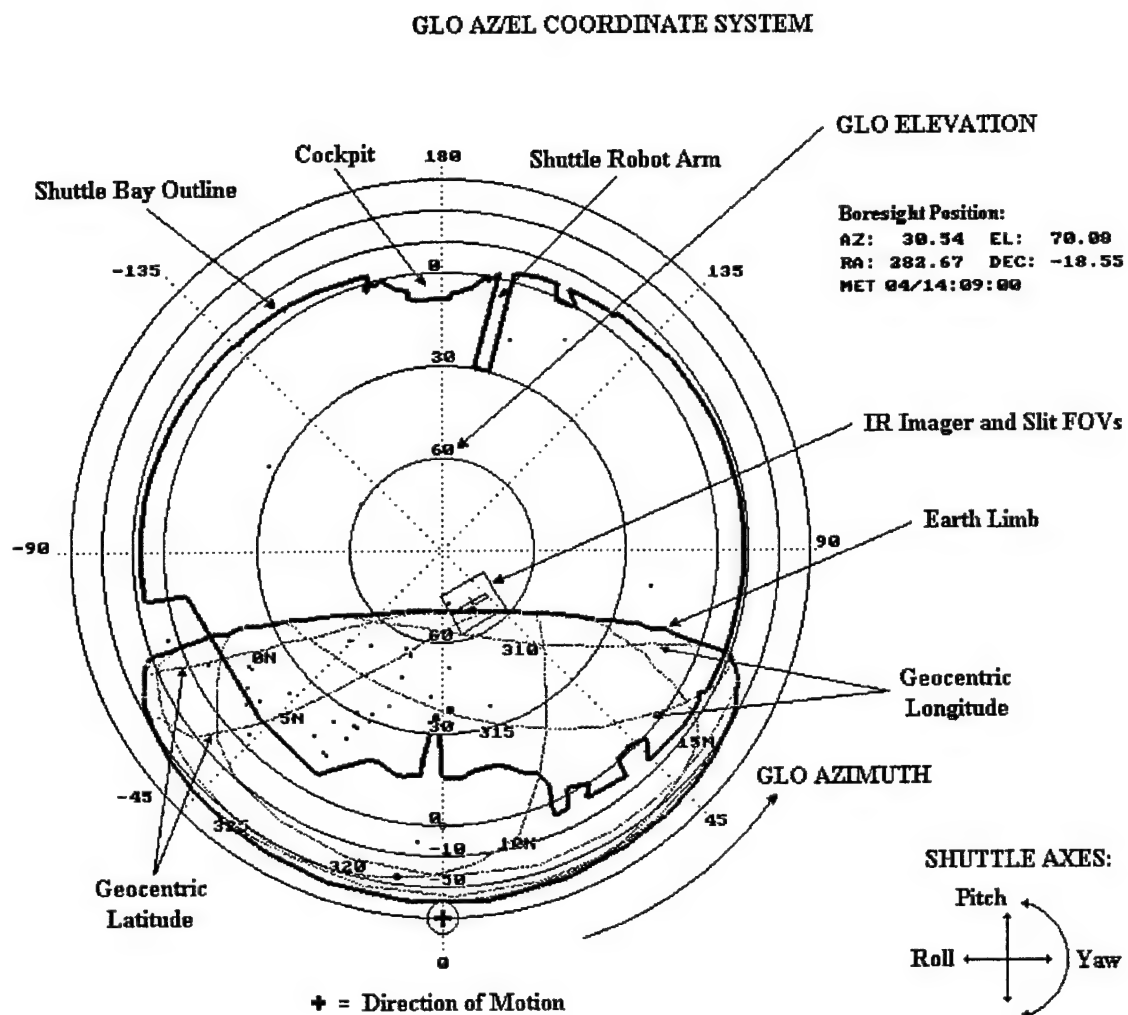
Figure 2.5. "Fish-eye" view of the GLO scan platform coordinate system showing the Earth and stars. The Earth limb is depressed about 18° from GLO zenith. Note the slit tilt of 30° at the limb, the orientation of the Shuttle axes, the star in the IR Imager FOV, and the outline of the shuttle bay as seen by GLO.

2.3 Space Shuttle Attitude and GLO Pointing Accuracy

The shuttle attitude, and hence the GLO observation line-of-sight (LOS), are referenced to a gyroscopic platform known as an Inertial Measurement Unit (IMU). Shuttle attitude is maintained by the IMU, which provides inertial attitude data used to control the shuttle flight surfaces, the thrust vector for the main engine, and the reaction control system verniers. The IMU permits very accurately shuttle attitude determination. Although the shuttle pitch, roll, and yaw axes drift between attitude limits called the "deadband," shuttle instantaneous attitude is well known (see Figure 2.6 on the next page for definitions of shuttle pitch, roll, and yaw). For STS-69, the deadband was ±1.0° in shuttle roll and pitch, and ±3.0° in yaw.

The shuttle also experiences slight attitude variations because of slow gyrocompass drift in the IMU. The IMU uses accelerometers, gyros, and electromechanical devices to maintain attitude. All are preflight calibrated to fine tolerances, but the gyros require periodic on-orbit alignment for drift. Typically, the IMU is recalibrated daily against the star field, but this is not
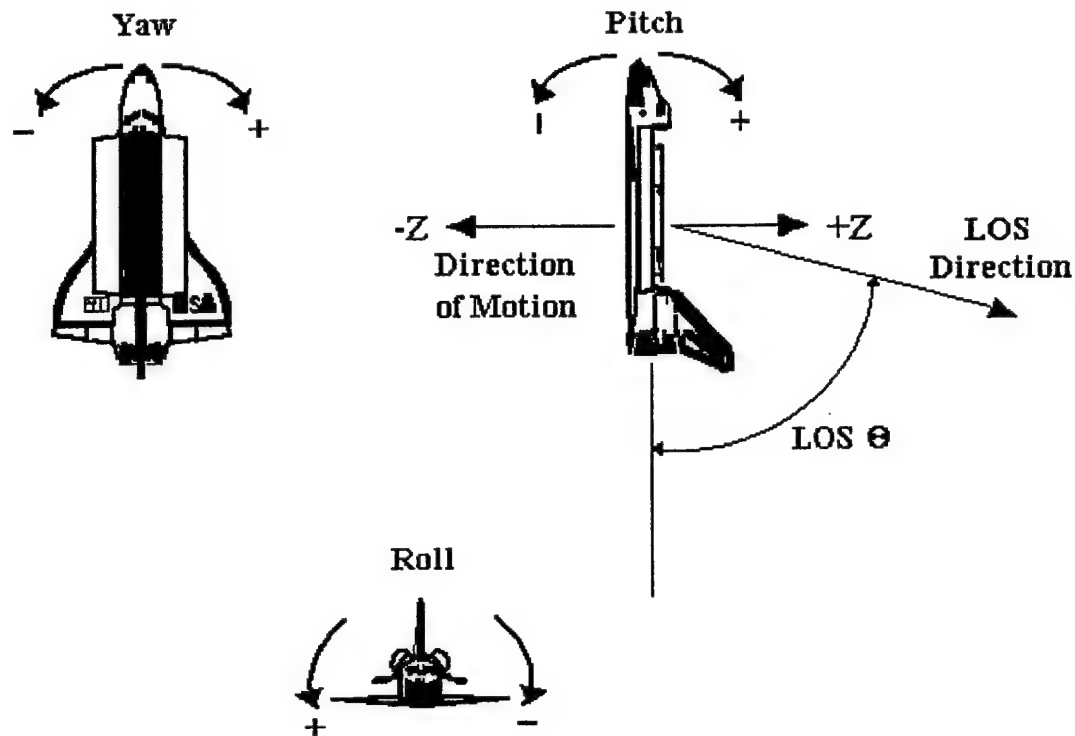
Figure 2.6. Shuttle pitch, roll, and yaw axes.

always possible. On the STS-69 mission, an uncorrected IMU gyrocompass drift of 0.14° occurred in a 47 hour period. This drift represented an error of about 5 km in some direction with respect to the Earth's limb (although not all of the drift would have been in the pitch direction to constitute an altitude error). The IMU was reset about midway through our 39 orbit run. NASA mission control provided the times of realignments during the mission, so the maximum error in pointing due to this drift is known as a function of time.

Four mounting gimbals isolate the IMU from shuttle rotations in pitch, roll, and yaw, in order to maintain inertial attitude. One IMU is sufficient for maintaining attitude, but three are installed for redundancy. They are intentionally *not* coaligned and *not* aligned with the shuttle pitch, roll, and yaw axes. This skewed arrangement provides redundancy for shuttle attitudes in which a single IMU's gimbals would not be effective and permits cross-checking of IMU failures. However, because of the skewed IMU axes arrangement and handovers among IMUs in real time, the *direction* of gyrocompass drift with respect to the pitch, roll, and yaw axes is not a parameter readily available from NASA. The worst case scenario would be for all IMU drift to occur in the pitch axis. Appendix C discusses the effects of shuttle pitch variations on GLO pointing and limb tracking.

The full excursion of axis drift within the deadband is known as the shuttle "limit cycle." Figures 2.7 and 2.8 show the STS-69 limit cycle over two full orbits, indicating the drift in roll, pitch, and yaw over two 90 minute periods. NASA provides post-flight attitude data with one second time resolution for precise determination of shuttle orientation. NASA data give

shuttle pitch, yaw, and roll in degrees to at least ±0.0001°. Previous flight experiments (Neupert et al., 1992) have shown that the overall accuracy of attitude determination along any axis is at least ±0.001°. Attitude variations on one second time scales are smooth to within seconds of arc.

During the collection of our 39 orbit data set, the shuttle velocity vector was in the direction of the -Z axis ("belly to ram") and GLO viewed out of the bay into the shuttle wake. The flight dynamics are shown by the limit cycle motion indicated in the previous two plots. Recall the limit cycle is the excursion of attitude drift with respect to the IMU. Perturbing forces in the pitch, roll and yaw planes are counterbalanced by vernier thruster firings whenever the pitch and roll axes vary ±1° from nominal and whenever the yaw axis varies ±3° from nominal. Dynamic imbalances in pitch and roll are greater than the imbalance in yaw. Cross-coupling of pitch and roll corrections causes the yaw motion to be irregular.

STS-69 LIMIT CYCLE FOR ORBIT 71
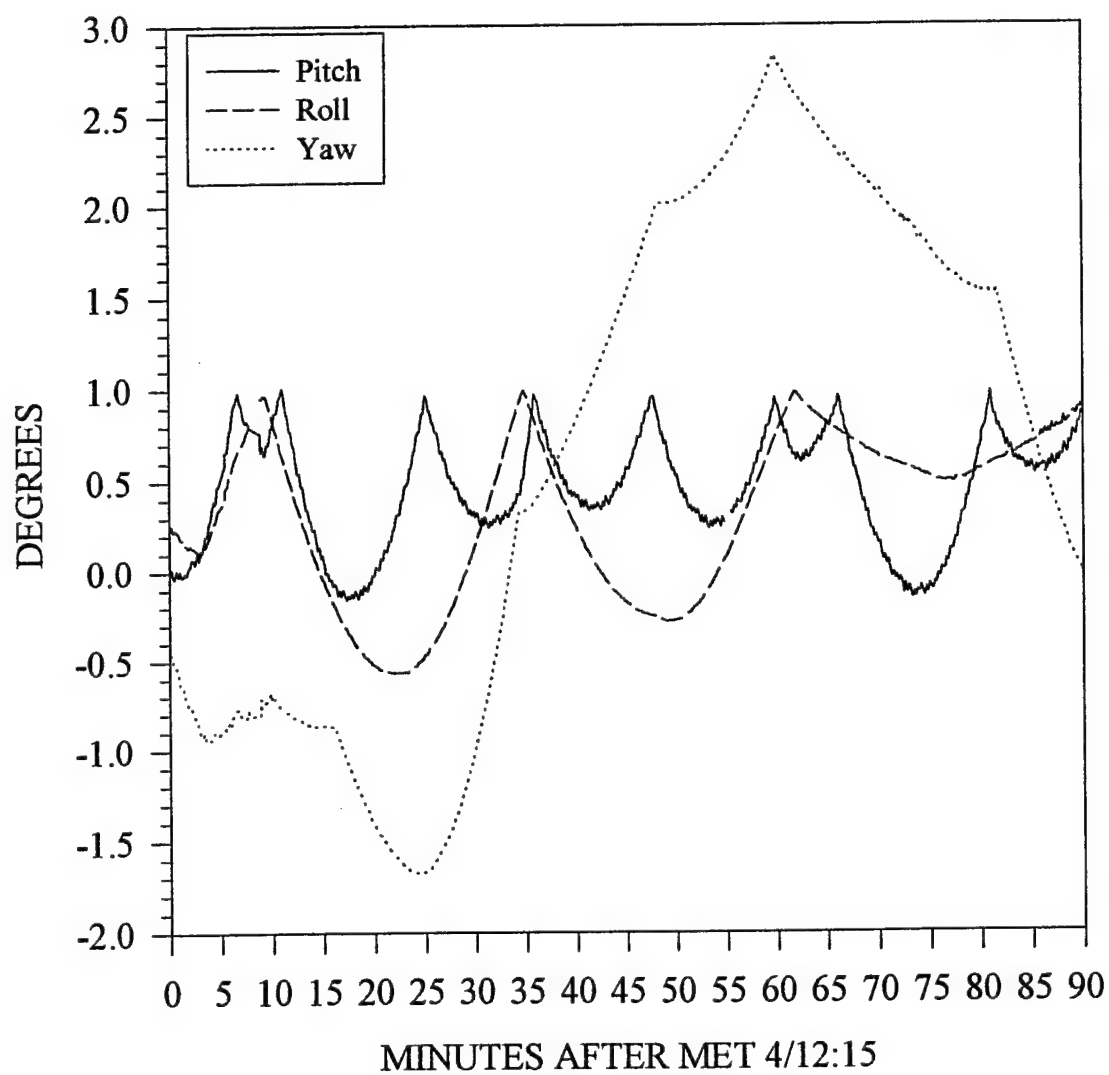
Figure 2.7. STS-69 attitude drift with respect to the IMU for orbit 71.
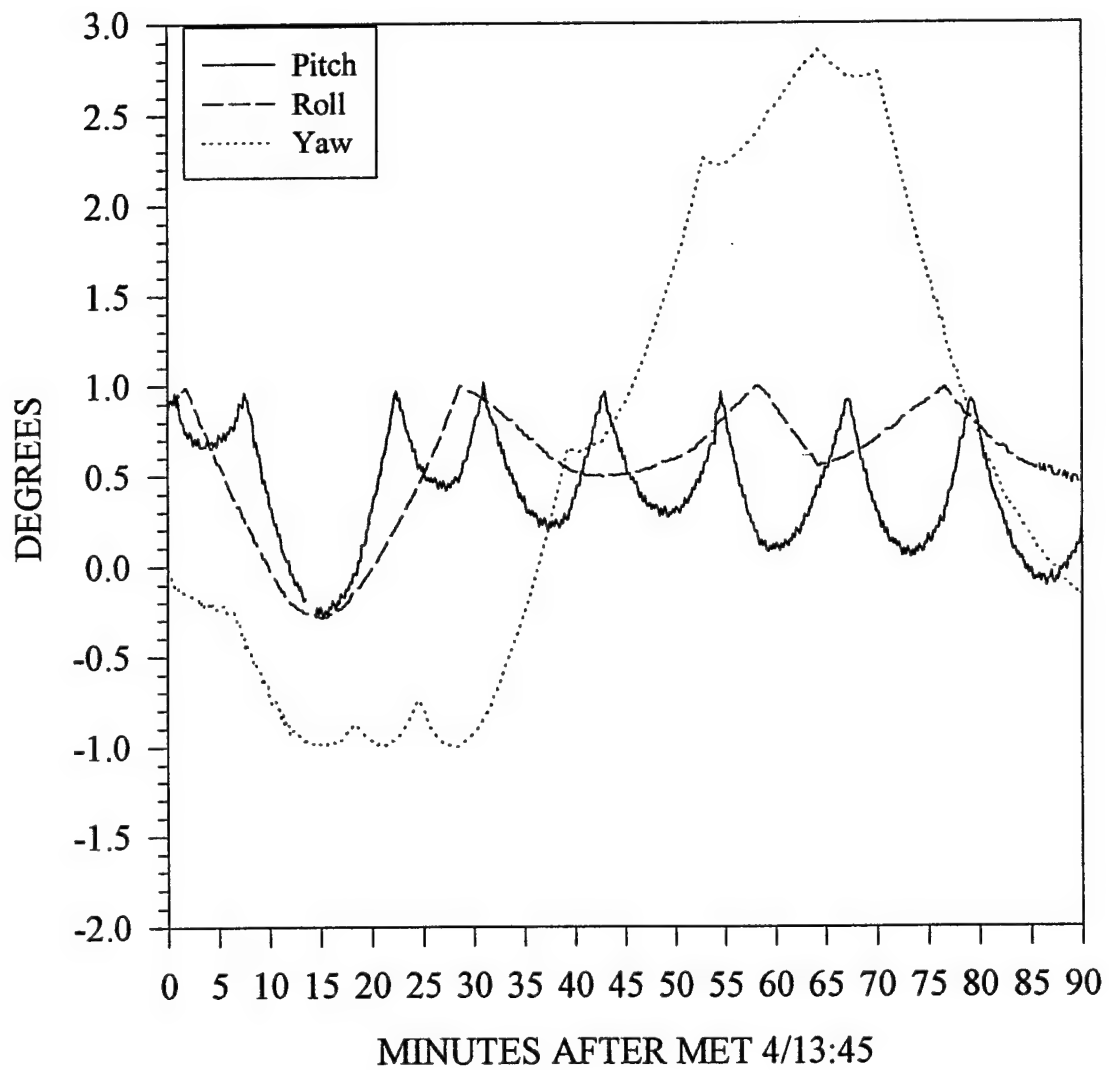
Figure 2.8. STS-69 attitude drift with respect to the IMU for orbit 72.

With the GLO scan platform motionless, changes in LOS pointing can be retrieved from knowledge of shuttle attitude to an accuracy of $\pm 0.005°$, or about ± 175 meters at the limb. However, removing uncertainty in the alignment of the shuttle axes and the GLO scan platform AZ/EL axes requires a calibration of the two systems with respect to the star field. The offset between actual GLO boresight pointing and the commanded AZ/EL position is obtained by the method described in the next section.

2.4 Pointing Calibration Against the Star Field

Many stars pass through the IR imager's FOV on each orbit. For pointing calibration, an IR imager frame containing a known star is chosen. Each image frame recorded by the IR imager contains header information giving the commanded boresight AZ and EL at the time of observation. Dr. Bill Sandel of LPL West prepared an algorithm to compute star position in "true" GLO AZ/EL coordinates, given a known star's astronomical right ascension (RA) and declination (Dec) coordinates. This is possible because the shuttle coordinate system and the RA and Dec system are related by a known rotation.

If a star is located *exactly* at the boresight position in the imager's pixel array, Dr. Sandel's program will immediately give an offset for the boresight position with reference to the Shuttle coordinate system, since the star's position is well known. Generally, a star's position will not be so fortuitous, and angular separation across the FOV must be calculated in both coordinate systems. If the FOV of the imager is near the GLO azimuth axis (or RA axis)

of the coordinate system, the strong curvature of lines of constant GLO

elevation (or Dec) prevents the simple determination of angular separation by

overlay of the grid system on the imager's rectangular pixel coordinates. Dr.

Emmet Anderson of LPL West provided a FORTRAN program to account for

this effect. Using the algorithms of Dr. Sandel and Dr. Anderson, the "true"

AZ/EL coordinates of the boresight pixel in the IR imager's CCD array can

be determined, since we know the AZ/EL pixel scale (57 pixels per degree in

this case) and we can measure the angular separation between the star and the

boresight. The difference between the "true" AZ/EL boresight position and

the commanded AZ/EL boresight position gives the pointing error between

the GLO AZ/EL coordinate system and the shuttle coordinate system. The

true boresight position at one specific time was determined, based on an IR

image with the stars ξ^2 Sgr, o Sgr, π Sgr, and one unnamed star in Sagittarius

(see Figure 2.9 on the next page; note that NASA uses celestial coordinates

for Julian epoch 1950).

However, comparison of this true value with the commanded boresight

position was not possible because of uncertainty in the precise timing of the

o Sgr
RA 285.42
Dec -21.82

π Sgr
RA 286.70
Dec -21.10

Boresight
RA 285.68
Dec -19.31

EL

AZ

All Coordinates
in Epoch J1950

ξ² Sgr
RA 283.69
Dec -21.17

Unnamed Star
RA 284.14
Dec -19.38
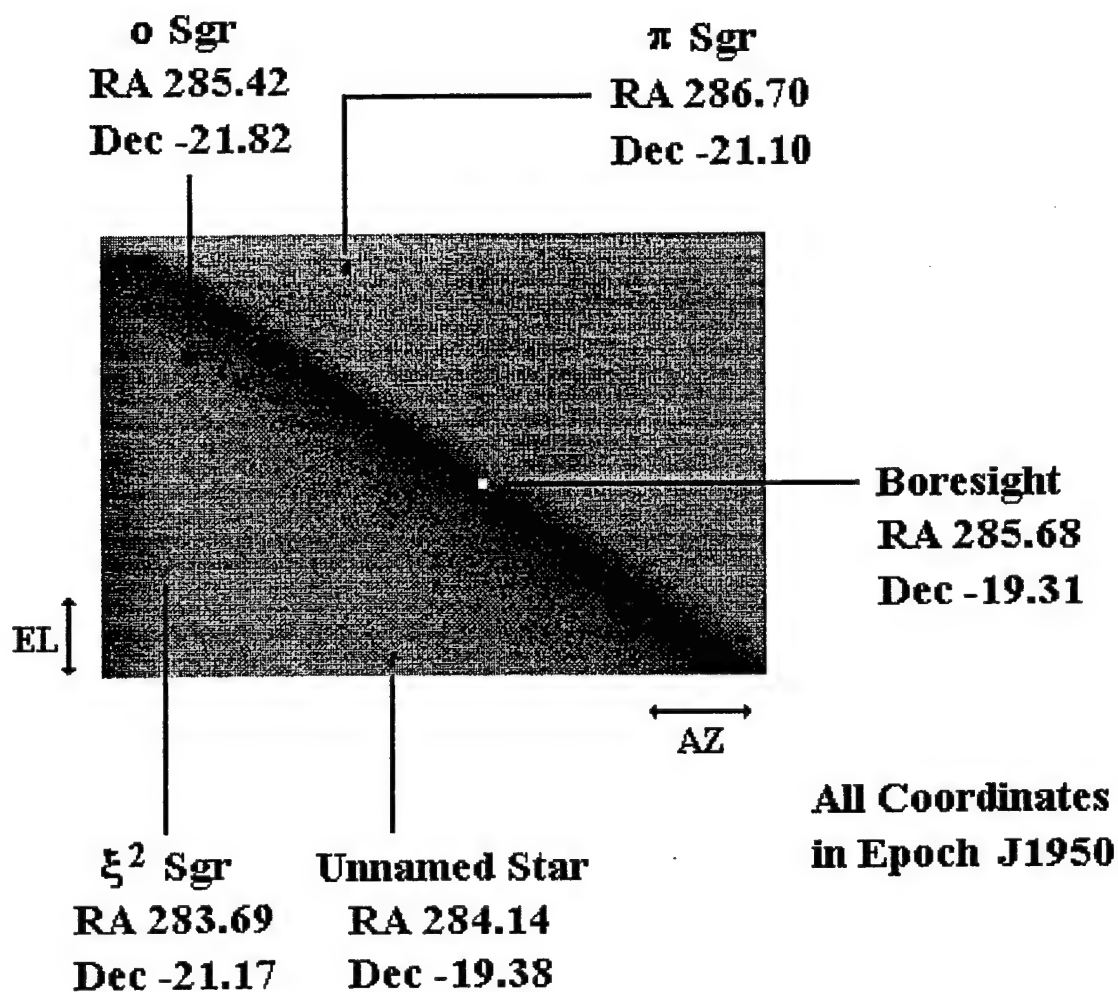
IR Image 4140936H.FIT

Figure 2.9. IR image used in boresight calibration.

exposure. GLO's internal clock labels spectrograph and imager exposures, but it lags behind the much more accurate orbiter clock. Orbiter mission time

is used to determine the position of the Shuttle and thus observation geometry and the tangent point height along the LOS direction. Only the GLO time label is known for a given imager exposure, not the orbiter mission time. A five second offset between GLO time and orbiter time, with GLO lagging behind, was typical over a 24 hour period. Since the tangent point height changes by about 2.4 km each second, a discrepancy of only 5 seconds between GLO time and orbiter time would amount to an altitude determination error of about 12 km. The GLO clock is ideally reset to mission time every 24 hours, but this was not always done during mission STS-69, and errors greater than 5 seconds were possible.

Thus, the most serious obstacle to determination of the absolute pointing accuracy of the GLO boresight in this data set is the GLO clock. With some effort, the drift of the clock can be estimated and propagated from the last clock reset. In the future, it is recommended that the GLO clock be reset to orbiter time on a regular basis so that the drift never exceeds one second. In this work, airglow altitudes have been corrected with respect to the sodium layer at 90 km, assumed to be a stable reference altitude.

3. DATA ANALYSIS AND OBSERVATIONS

Since GLO observes a wide spectral range simultaneously from a column of gas along the line-of-sight, a large amount of information is recorded in each exposure. Juxtaposing a series of spectrograph exposures as the instrument FOV sweeps along the orbit track creates a three-dimensional data array of column emission intensities in rayleighs as a function of wavelength, altitude, and elapsed time (or distance). Such an array is called a "monochromatic image." These arrays can be studied in many ways. The approach taken here is to extract monochromatic images of night sky emissions in the O_2 Atmospheric bands, the OH Meinel bands, and OI (5577 Å), showing the behavior of these emissions along the orbital track.

GLO spectra provide column emission intensities in rayleighs for various emissions in the airglow layer above the Earth's limb. An Abel integral inversion algorithm (Appendix D) is then applied to these column intensities in order to obtain volume emission rates in photons per cubic centimeter per second and to construct vertical emission profiles. Such

profiles show the behavior of the different airglow emissions as a function of altitude and time. From such profiles, we can infer how the airglow layer changes in intensity, height, and thickness, and by knowing the chemistry involved in the different emission processes, test proposed mechanisms to explain the observed variations.

In the discussion that follows, data reported or plotted in rayleighs has not been subjected to the Abel inversion process, while quantities reported or plotted in photons per cubic centimeter per second represent inverted data.

3.1 Spectral Imaging and Monochromatic Images
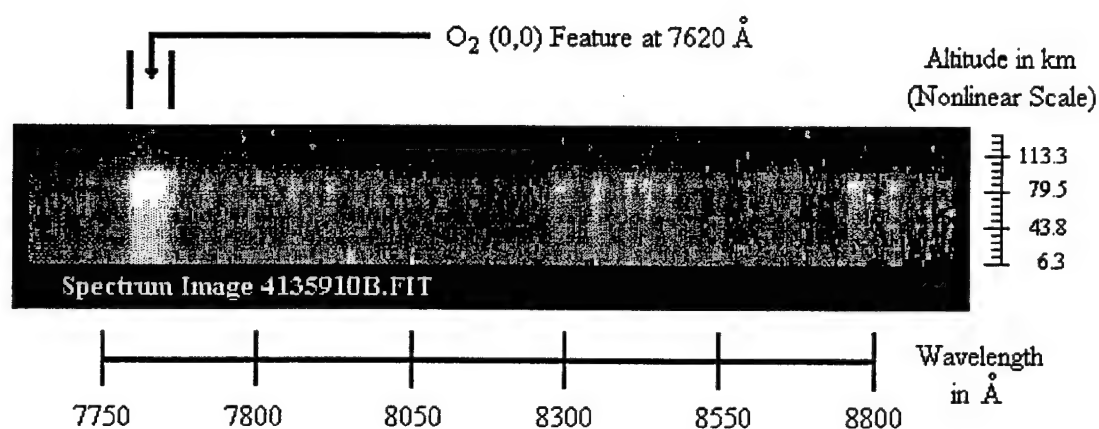
Figure 3.1. STS-69 GLO spectrum showing O_2 Atmospheric and OH Meinel bands.

The holographically ruled concave grating in each spectrograph forms an image of the entrance slit dispersed in the image plane of the detector. The ruling corrects aberrations and flattens the field on the detector, thus preserving spatial information along the slit. For the data recorded here, the slit accepts a one-dimensional portion of the image of the airglow layer produced by the foreoptics and from this, a spectrum is formed showing spectral intensity versus wavelength and altitude (Figure 3.1).

Figure 3.2 below shows a spectral image of O_2 Atmospheric and OH Meinel band emissions and a plot of the intensity versus wavelength. The two curves in Figure 3.2 are the same. One is given at full scale, and the other is reduced by a factor of 5 in order to show the relative intensity of the O_2 (0,0) band compared to other emissions.
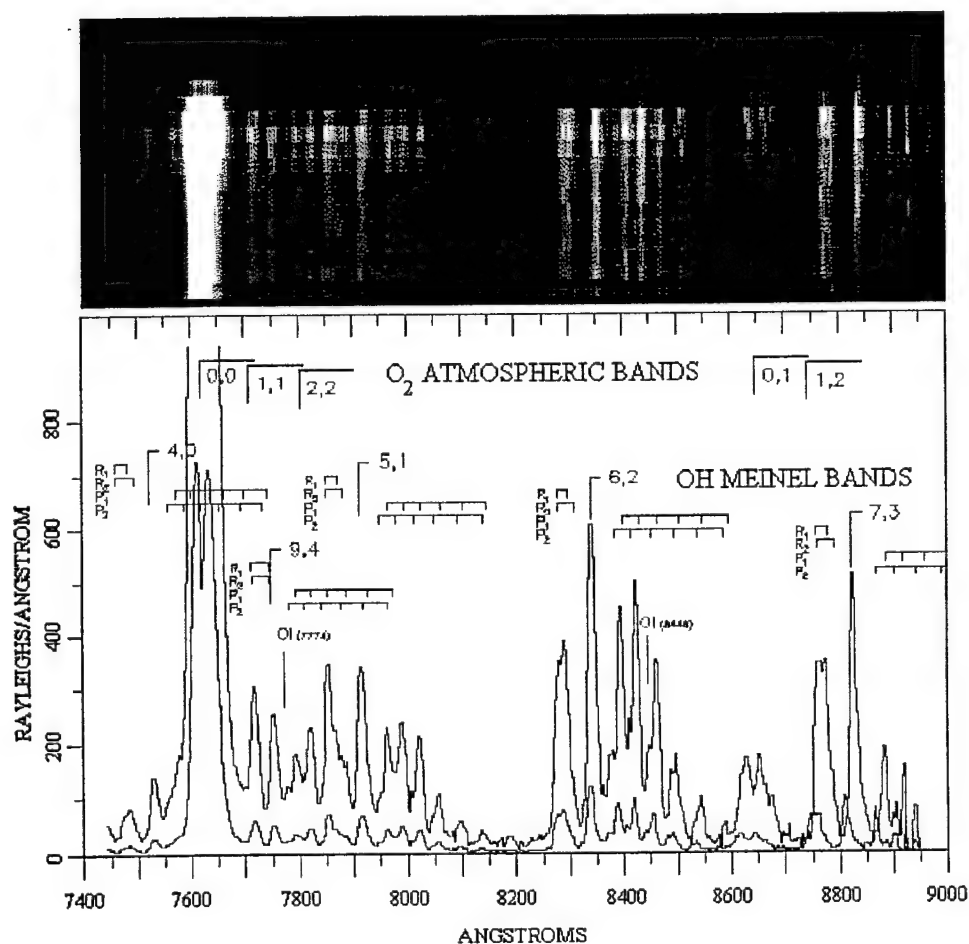
Figure 3.2. Plot of intensity versus wavelength for a typical spectral image from GLO spectrograph B (see Table 2.1).

Monochromatic altitude profiles of selected emissions can be constructed from the spectral images. Intensity for the specific spectral feature of interest is determined from the calibrated data. A spectral sample and background sample are illustrated in Figure 3.3. The defined spectral region is for the O_2 (0,0) band emission. The intensity is summed over the region. Then the background intensity region is defined, scaled, and subtracted from the O_2 (0,0) intensity region, resulting in the total band intensity in rayleighs for the O_2 (0,0) band. This procedure is equivalent to applying a monochromatic bandpass filter, except in this technique, the equivalent filter has an adjustable bandpass with very sharp edges, allows all emissions falling within the bandpass from the column of gas in view to be recorded simultaneously, and permits unwanted emissions and background intensity to be removed easily by defining the bandpass as one wishes.
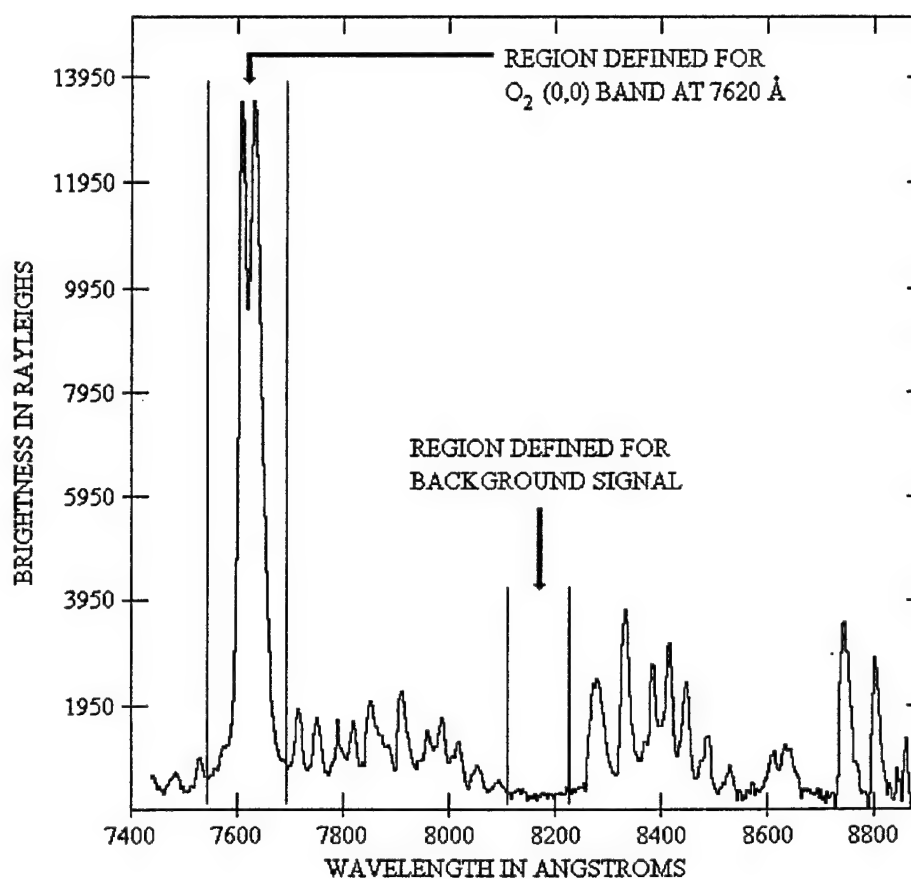
Figure 3.3. Digital separation of signal and background acts as a bandpass filter.

Vertical intensity profiles of a selected emission can be extracted from each spectral image. The sampling procedure above is performed on each of the 24 spectra in a spectral image, resulting in 24 monochromatic samples at 24 contiguous altitudes. These vertical intensity profiles of the original spectra can then be rearranged in a side by side format to create another

array, showing intensity of the selected monochromatic feature versus altitude and horizontal displacement (or equivalently, elapsed time) along the orbital track. This monochromatic image is effectively "three-dimensional" in altitude, intensity, and elapsed time.

Examples of monochromatic images created from STS-69 spectra are depicted in Figure 3.4, and in Figures 3.5 through 3.7 in negative format. The horizontal dimension of these monochromatic images is time along the orbit track. In the monochromatic images depicted here, each vertical intensity profile represents an integration of 20 seconds on the detector. The relative brightness of each sample is represented in gray scale, forming a monochromatic image showing the spatial and temporal variations in emissions as the shuttle moved along its orbit at approximately 7.8 km/s. Since the gray scale of the images is not quantitative, the emission intensity along the orbit track at constant tangent heights is plotted in a graph below each image in Figures 3.5 through 3.7. Note that representative altitudes for selected rows in the array are indicated alongside the gray scale images at the top of Figures 3.5 through 3.7.
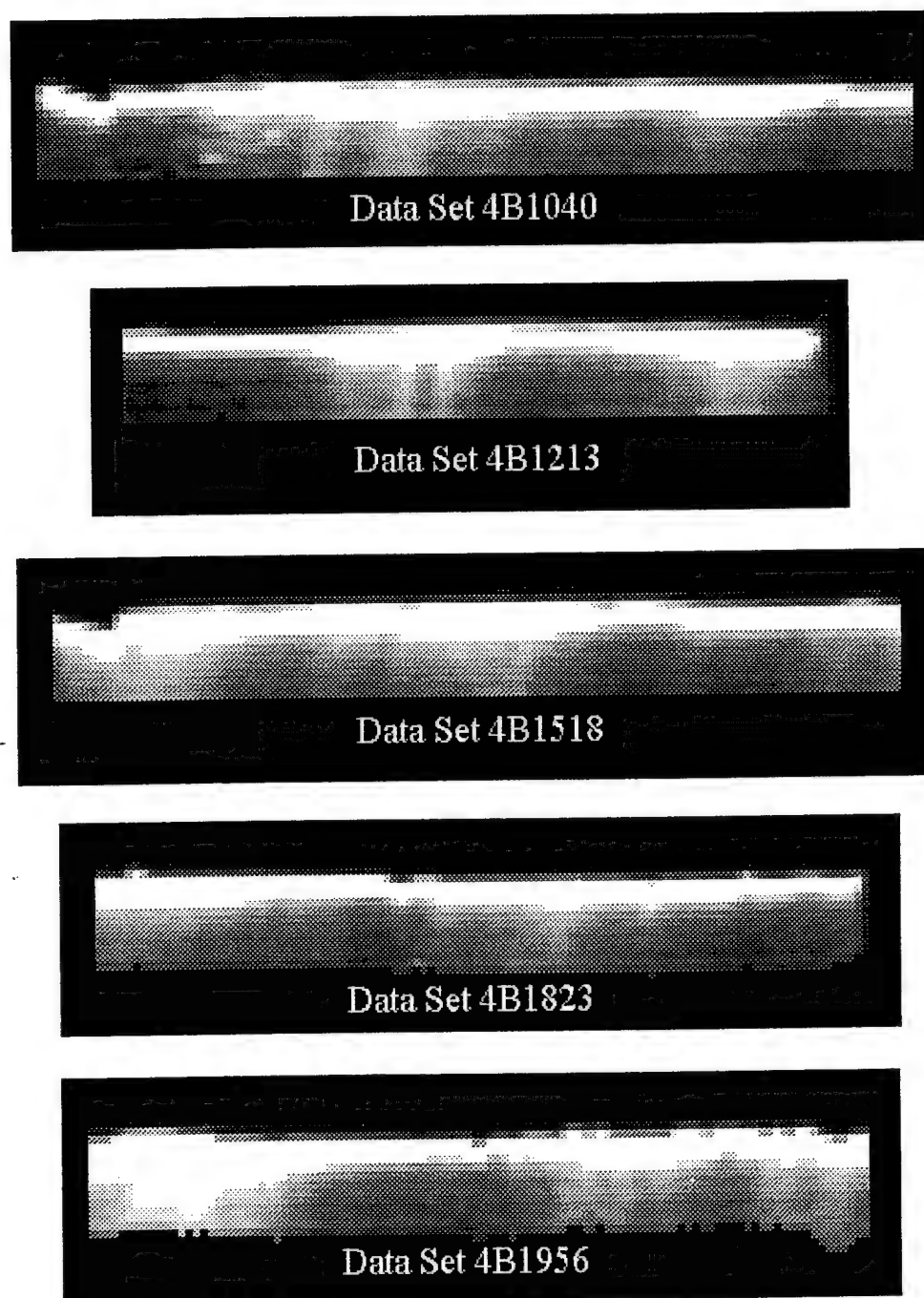
Figure 3.4. Monochromatic images in O_2 (0,0) from STS-69, MET day 4. The last four digits in each label give the MET times in hours and minutes.

Figures 3.5 through 3.7 show the line-of-sight column brightnesses of emissions at selected constant altitudes. The time axis of each brightness plot begins at the moment the orbiter crossed the terminator into shadow along the orbit track, relating all plots in local solar time. The O_2 (0,0) and OI (5577 Å) plots are similar, but the brightness variations of the two emissions do not coincide. The OH Meinel band emission is not correlated with either O_2 (0,0) or OI (5577 Å). Brightness changes vary with altitude in all three emissions.

Signal-to-noise ratios for O_2 (0,0), OH Meinel, OI (5577 Å), and O_2 (0,1) emissions in our data are on the order of 18, 10, 8, and 6, yielding brightness determination errors of 5%, 10%, 13%, and 17%, respectively. Summing N altitude profiles into one improves the signal-to-noise ratio by a factor of $\sqrt{N}$; a summation of 9 slices gives a factor of 3 increase, a summation of 25 gives a factor of 5, and so on (Broadfoot and Sandel, 1992). As long as variations among the slices being summed are minimized, information loss is also minimized. The "smearing" that does occur is equivalent to that caused by increased exposure or integration time, and represents a tradeoff between signal-to-noise ratio and temporal resolution.
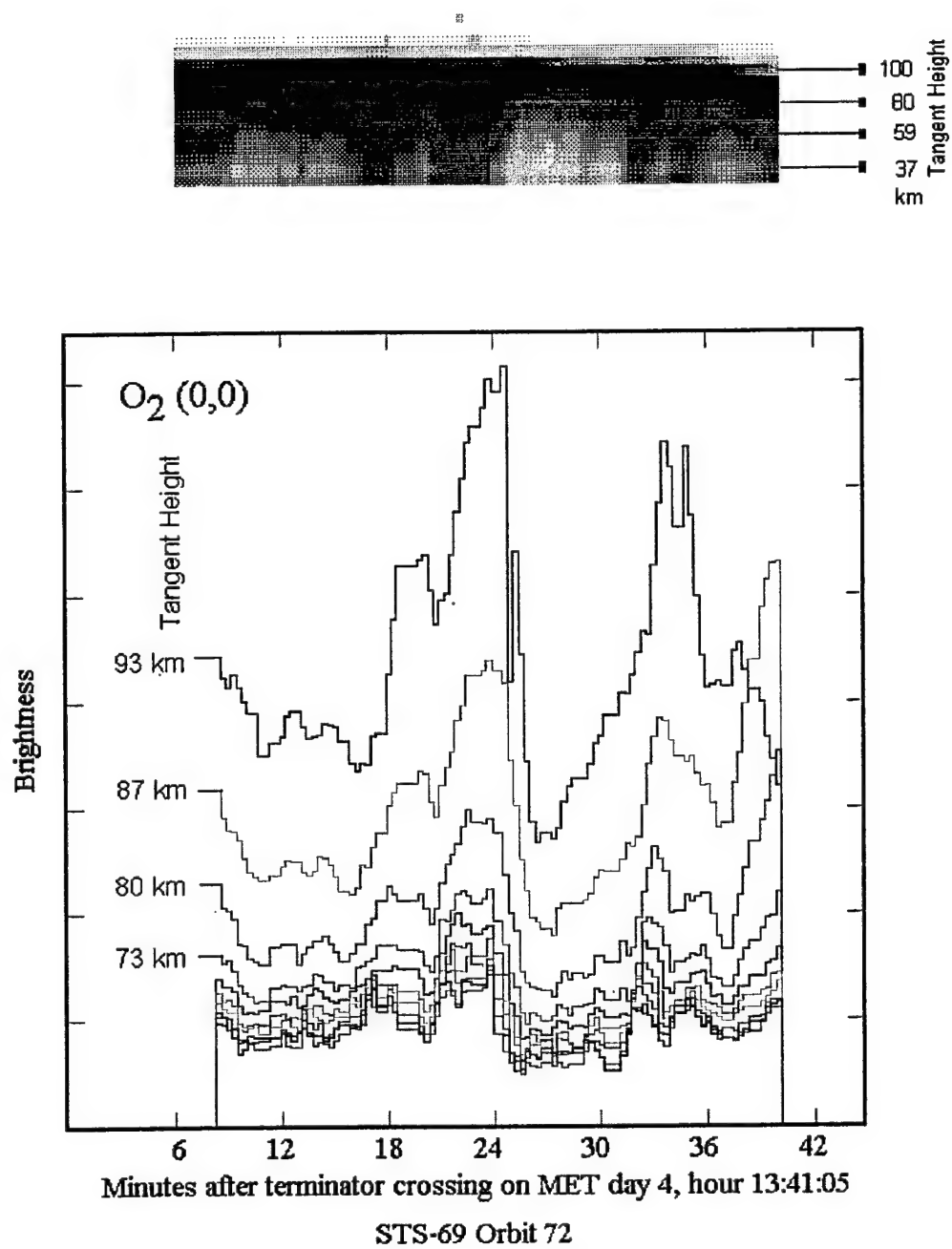
Figure 3.5. Monochromatic image and observed column brightness profile for the O_2 Atmospheric (0,0) band emission.
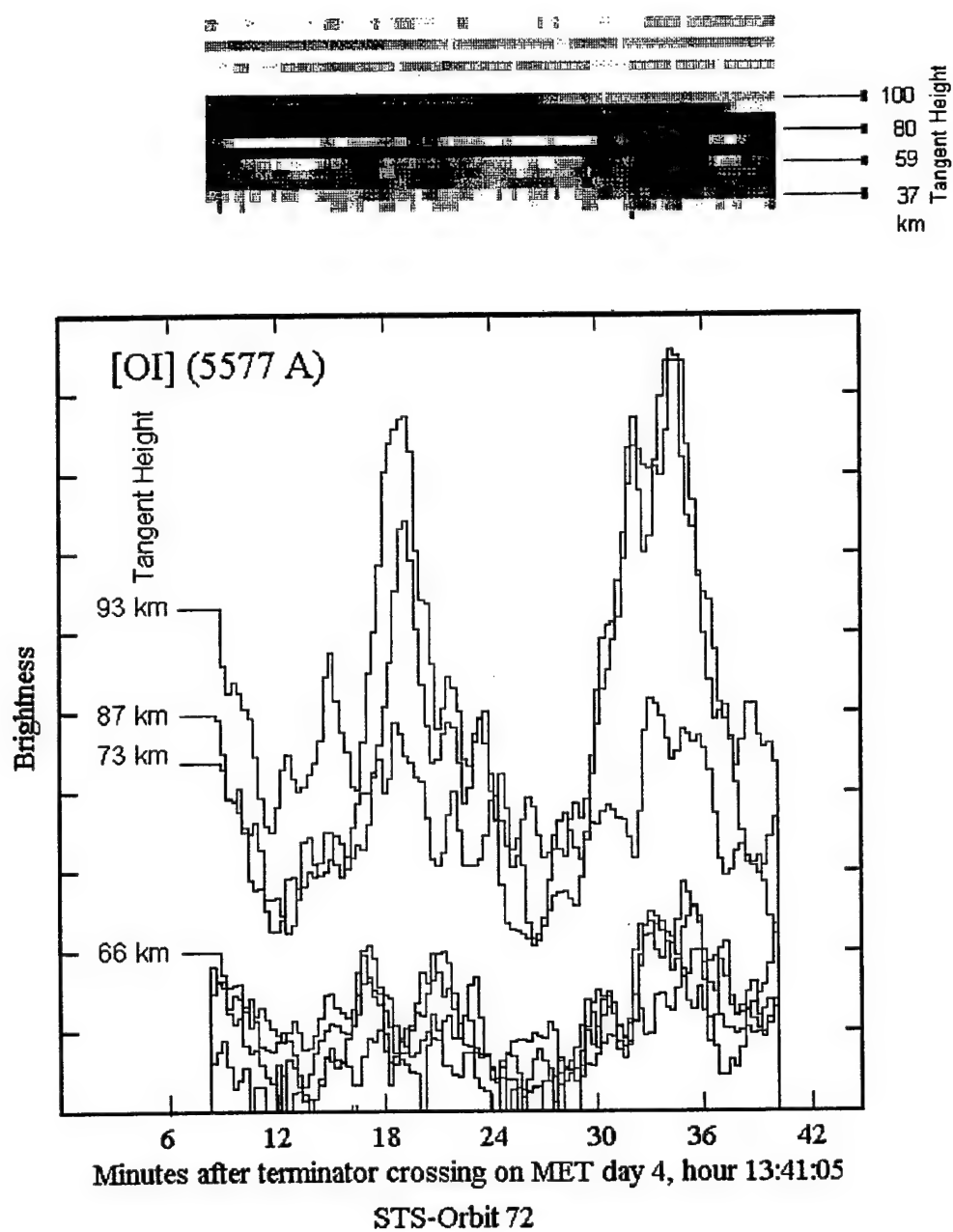
Figure 3.6. Monochromatic image and observed column brightness profile for the OI (5577 Å) emission.
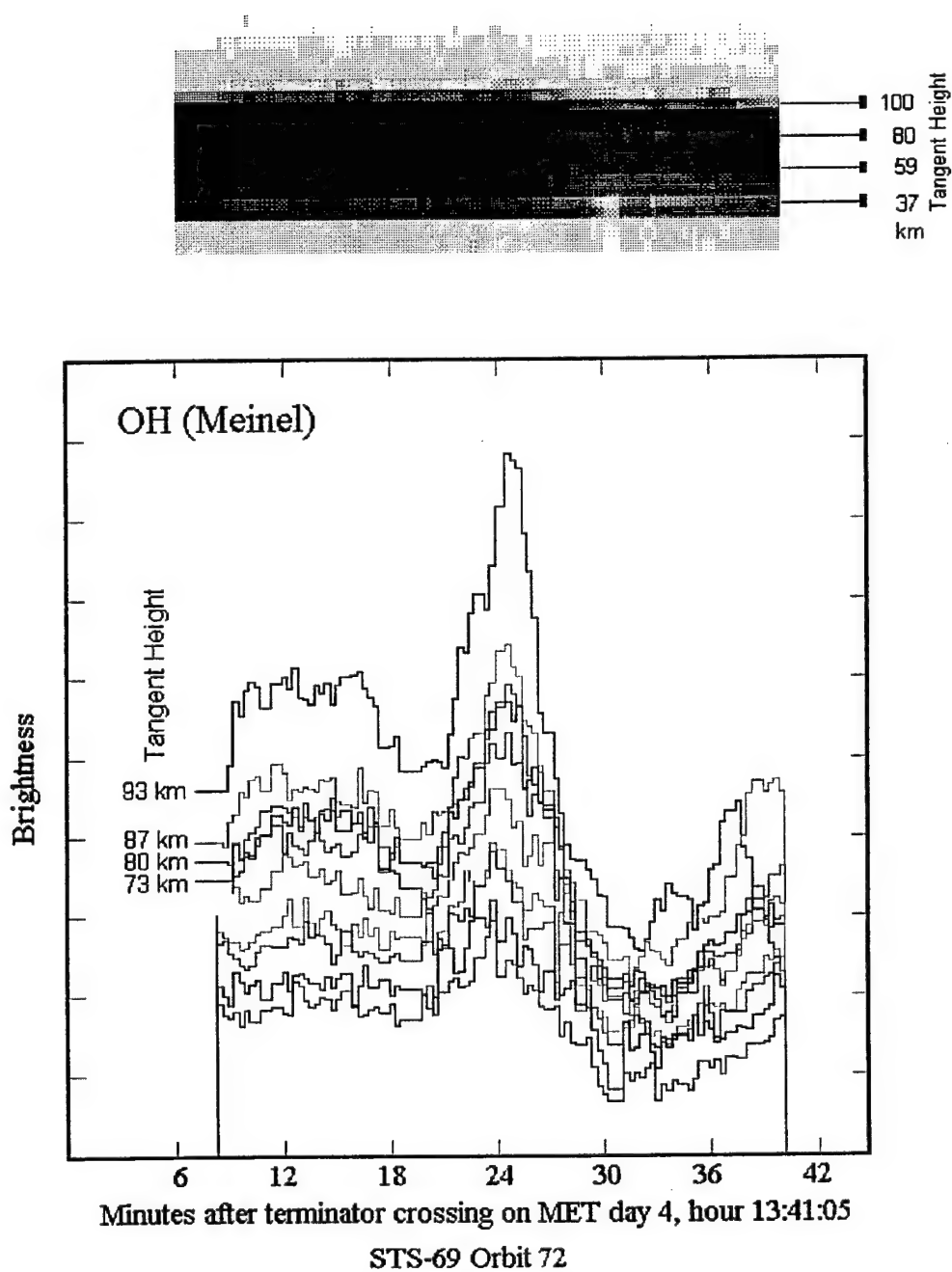
Figure 3.7. Monochromatic image and observed column brightness profile for the OH Meinel band emission.

3.2 Signatures of the O_2 (0,0) Band in the GLO Data Set

In this section, we will discuss O_2 (0,0) intensity variations seen in the night airglow for 29 orbits (71 through 99) during STS-69. This subset of the 39-orbit GLO data set was chosen for convenience and consistency, since observation geometry was less stable at the beginning and end of the 39-orbit data set.

The atmosphere is optically thick to emission of O_2 (0,0), so the column intensity recorded by GLO originates between the tangent point and the shuttle, with all emission from the far side of the line-of-sight being attenuated. Thus GLO observes an "O_2 (0,0) emission surface" restricted by the optical depth of O_2 (0,0). Because of this effect and because it is the brightest airglow emission, the O_2 (0,0) band is the best emission to use in examining wave signatures. On the other hand, the optical depth must be considered before inverting O_2 (0,0) intensities to obtain volume emission rates, which are necessary to interpret airglow chemistry. The interpretation of emissions in the O_2 Atmospheric (0,0) band requires radiative transfer

theory for a complete description. Solving the O_2 (0,0) radiative transfer problem will not be attempted here.

The variations in O_2 (0,0) intensity are of interest with respect to their relationship to the various types of waves that may exist in the MTI region. The plot of O_2 (0,0) column intensity variations along the track of orbit 72 in Figure 3.5 shows typical intensity enhancements. The half-width of the intensity peaks is about six minutes of orbiter flight time. At an orbital velocity of 7.8 km/sec, this half-width represents about 2800 km, which can be taken as the typical extent of an enhanced airglow region along the orbit track. With each night pass, the orbital track of STS-69 shifted 22.5° to the west, for a displacement of about 2500 km (Figure 1.4). If the intensity enhancements are part of a long lived phenomenon, they may be detected on consecutive orbits. With a characteristic extent between 2500 and 3000 km, they would just span the displacement between night passes. An isolated enhancement might be observed on two consecutive orbits, and an extensive wave front might be detected over several orbits.

STS-69 ORBITAL TRACK COVERAGE AS A FUNCTION OF LATITUDE AND LONGITUDE
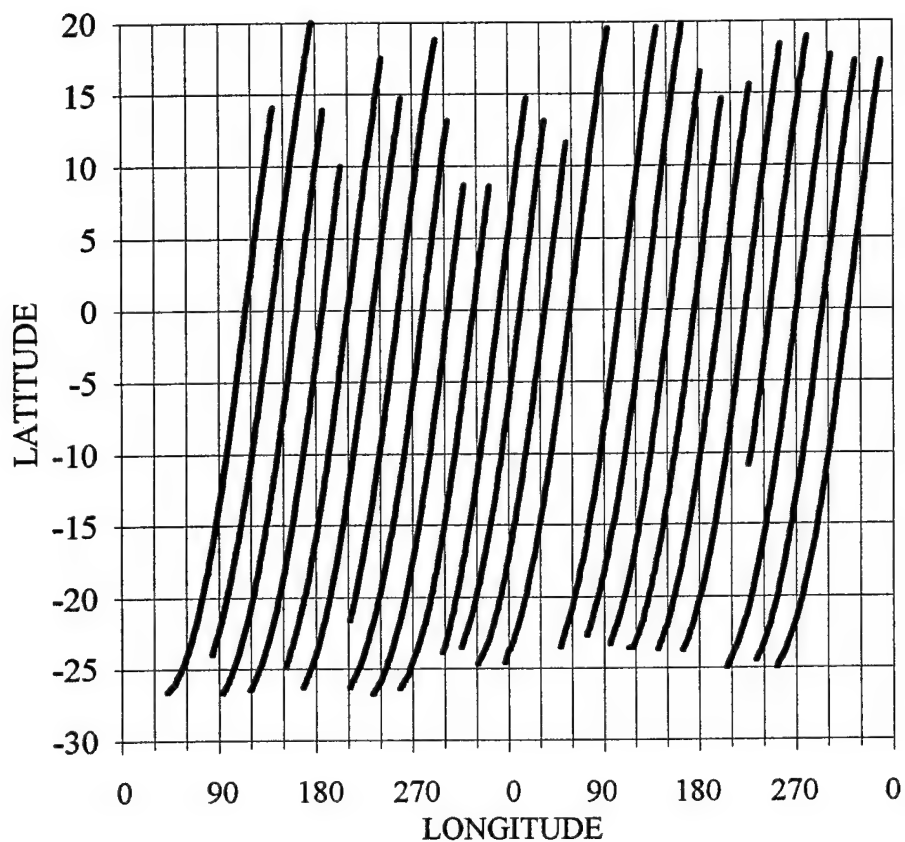
Figure 3.8. Orbit track coverage in latitude and longitude during the STS-69 mission. Orbit 71 is the first orbit at the right, while orbit 95 is the last on the left.
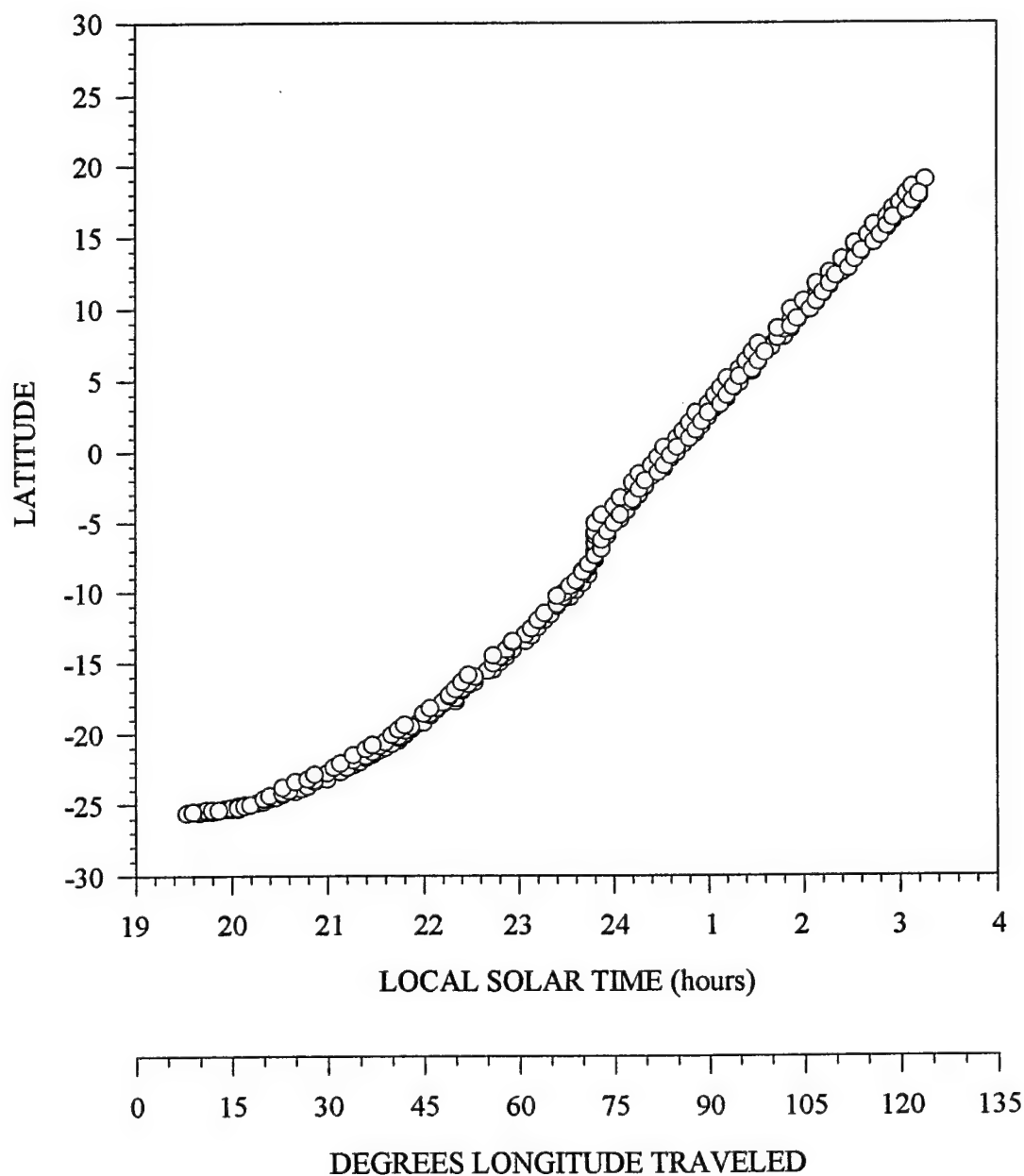
Figure 3.9. GLO observations during the STS-69 mission fell along an orbital track fixed in local time.

Figure 3.8 shows the geographic coverage of orbits during which GLO data was recorded and illustrates the latitude and longitude of the observational tracks. Figure 3.9 shows the local time trace of GLO observations during night passes through the Earth's shadow. Observations are seen to fall on a single orbital track fixed with respect to local solar time (LST) in Figure 3.9. Note that the orbital track is also fixed in latitudinal coverage and that the equatorial crossing occurs at 0.5 LST on every orbit.

In order to examine the data set for evidence of organized intensity enhancements that may be related to tides, the intensity along the orbital tracks has been plotted in Figures 3.10 and 3.11 as a function of local solar time. These two Figures show O_2 (0,0) brightness in rayleighs for 29 orbits. Fifteen orbits are plotted in each figure, with orbits 71 through 85 in Figure 3.10 and orbits 84 through 99 in Figure 3.11. The orbits overlap between the Figures. Intensity values are averaged over an altitude range of 20 km, centered at 90 km. The horizontal direction represents about 80 observations per orbit. The density of observations in this plot is thus much higher horizontally than vertically.

O$_2$ (0,0) BRIGHTNESS IN KILORAYLEIGHS
AVERAGED AT LAYER PEAK
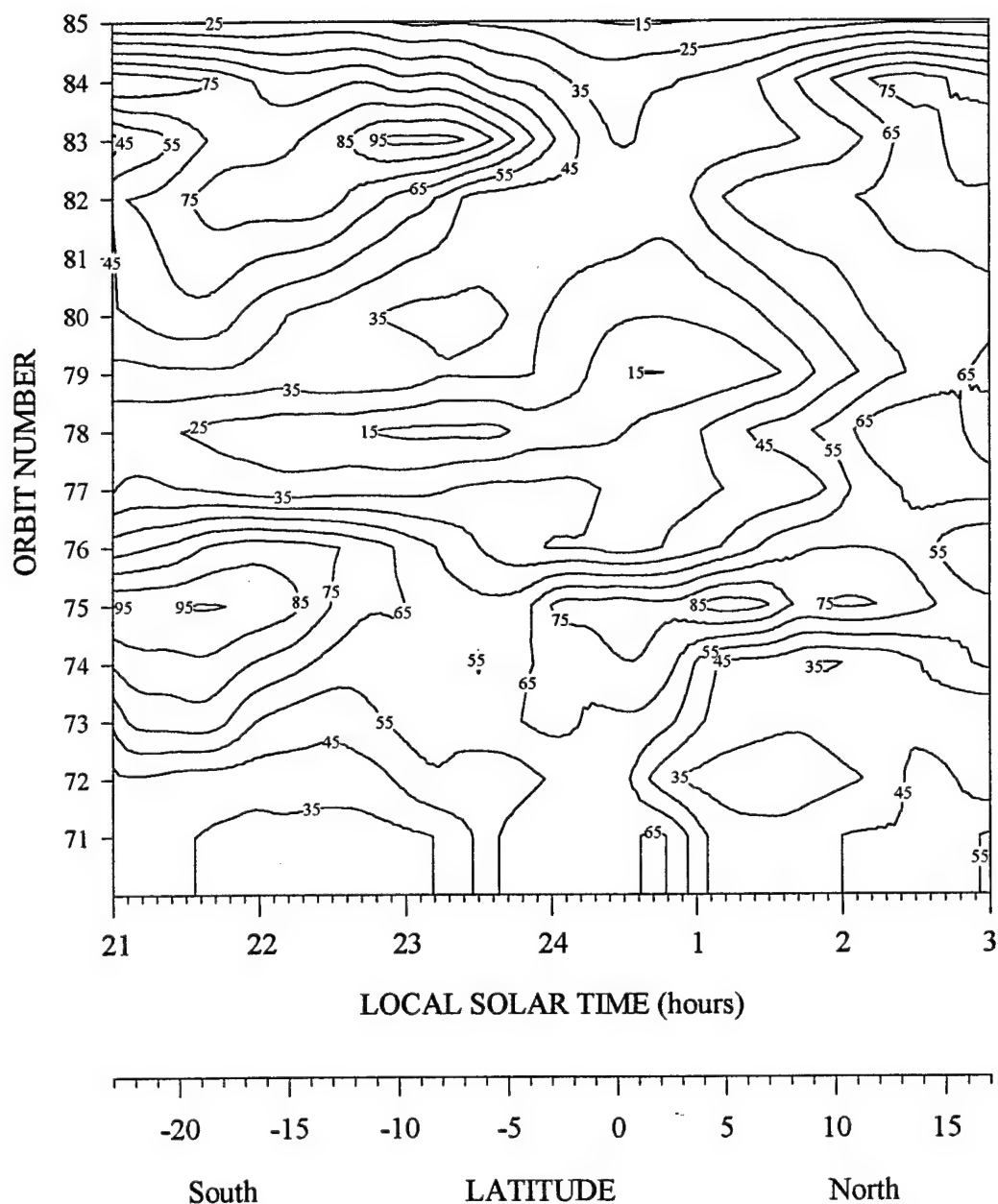
Figure 3.10. Brightness of the O$_2$ (0,0) emission for orbits 71 through 85 as a function of orbit and local solar time. There is no evidence of tidally-induced standing waves.

O$_2$ (0,0) BRIGHTNESS IN KILORAYLEIGHS
AVERAGED AT LAYER PEAK
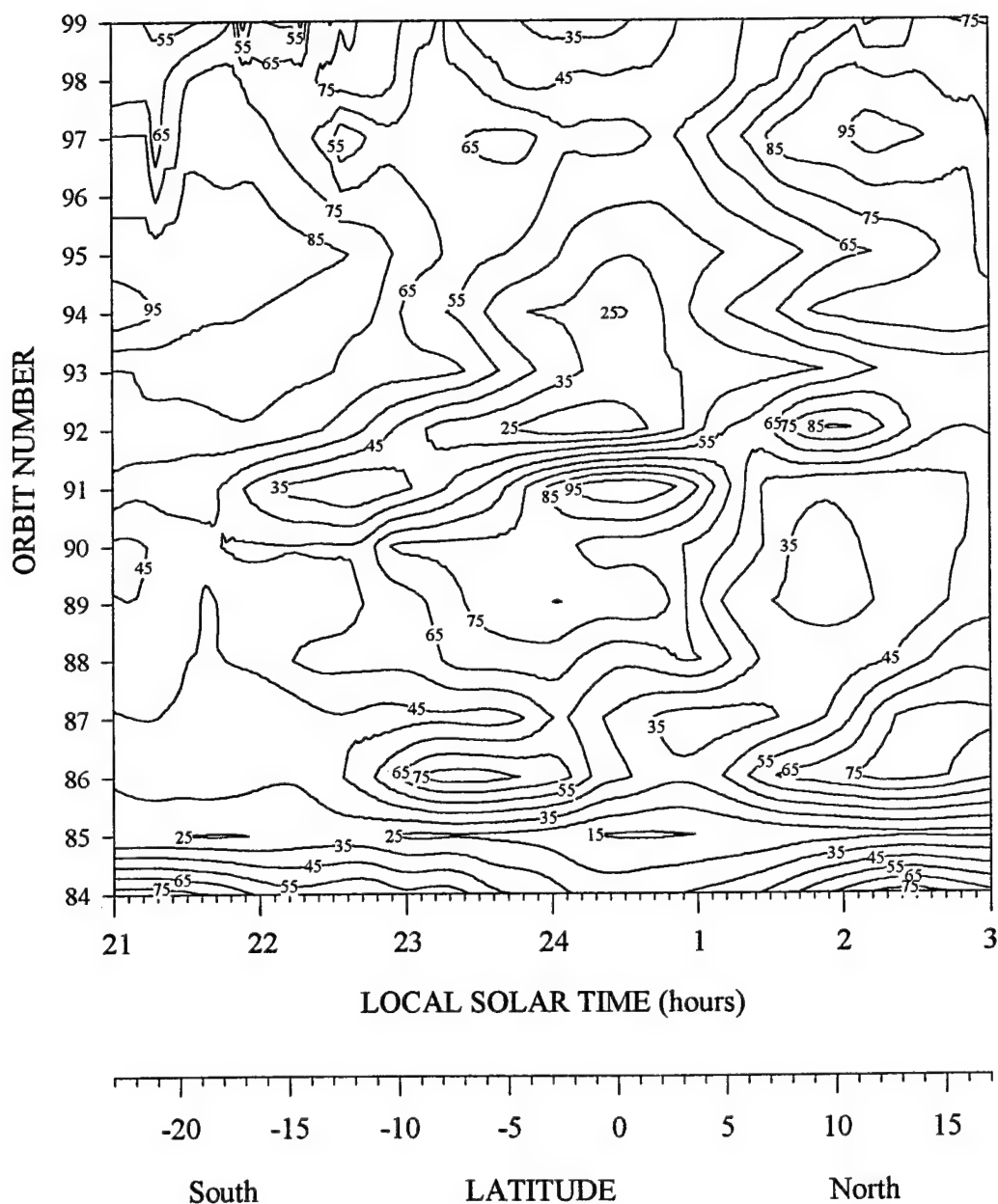
Figure 3.11. Brightness of the O$_2$ (0,0) emission for orbits 84 through 99 as a function of orbit and local solar time. There is no evidence of tidally-induced standing waves.

AVERAGED O$_2$(0,0) INTENSITY AS A FUNCTION OF LOCAL SOLAR TIME AND LATITUDE FOR 29 ORBITS
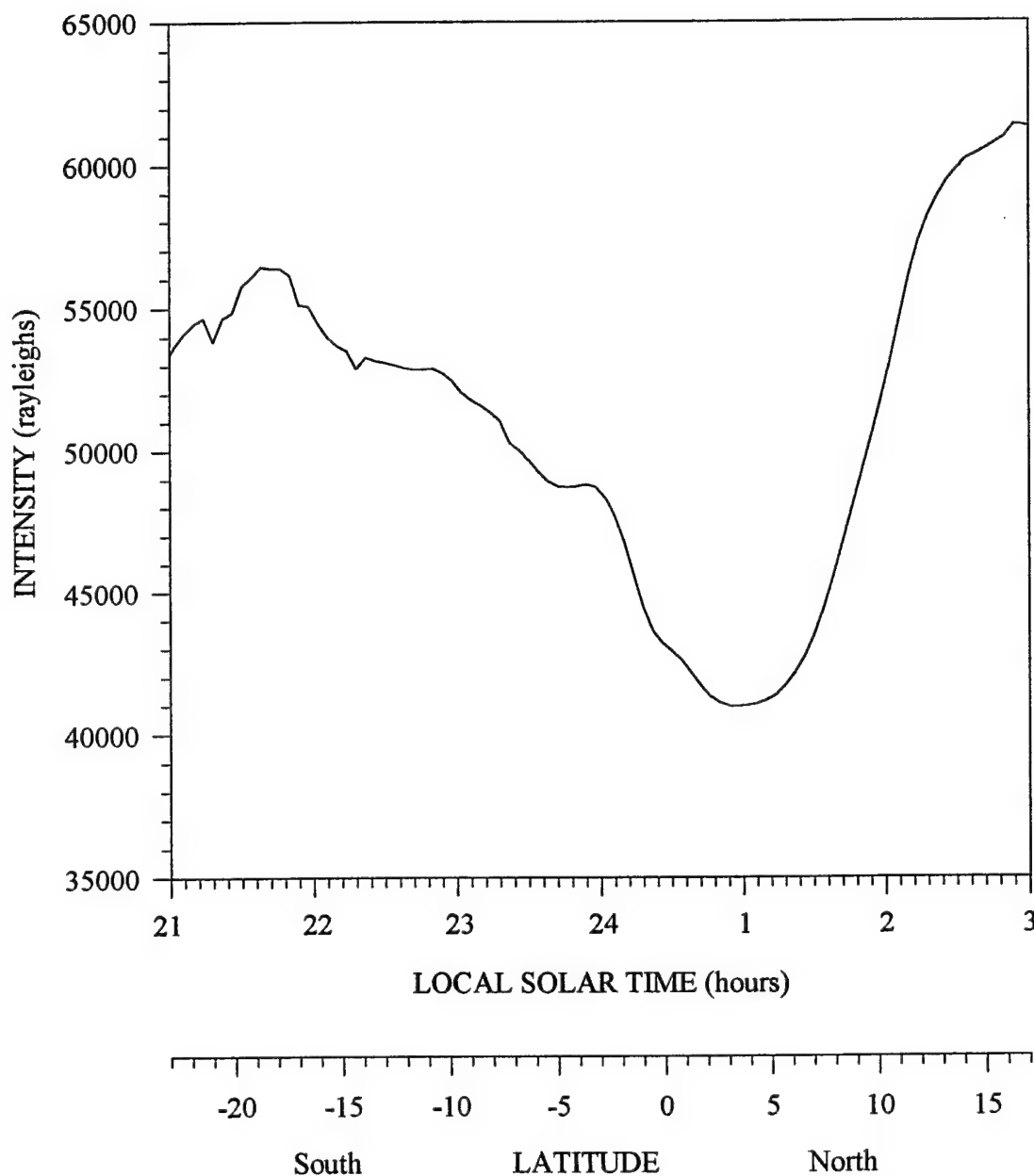
Figure 3.12. Intensity of the O$_2$ (0,0) emission averaged over orbits 71 through 99 as a function of local solar time. Note the pronounced intensity minimum near 1.0 LST, a few degrees north of the equator.

If tides existed in Figures 3.10 and 3.11, they would be detected as vertical bands of constant isopleths fixed in LST. However, moving vertically along these plots, brightness values change significantly from orbit to orbit, exhibiting no obvious correlation to local time. The implication is that tidal variations along our observation track, if they exist, are masked by other effects. Intensity variations caused by short duration vertical motions may dominate the more secular changes caused by tides.

A more sensitive test was performed by summing and averaging all of the data in local time to give the single curve in Figure 3.12. This is also a plot of the data as a function of latitude. Figure 3.12 shows that on average, the O_2 (0,0) intensity changes by a factor of 1.5 over a night pass. If tidal effects are present, they are masked by latitudinal variations. The minimum occurs near the equator, about one hour after local midnight. There is a suggestion of asymmetry in emission from south to north (dusk to dawn), with the northernmost (early morning) intensity being greater. The equatorial minimum is consistent with other observations, but there is still no signature of a tidal effect.
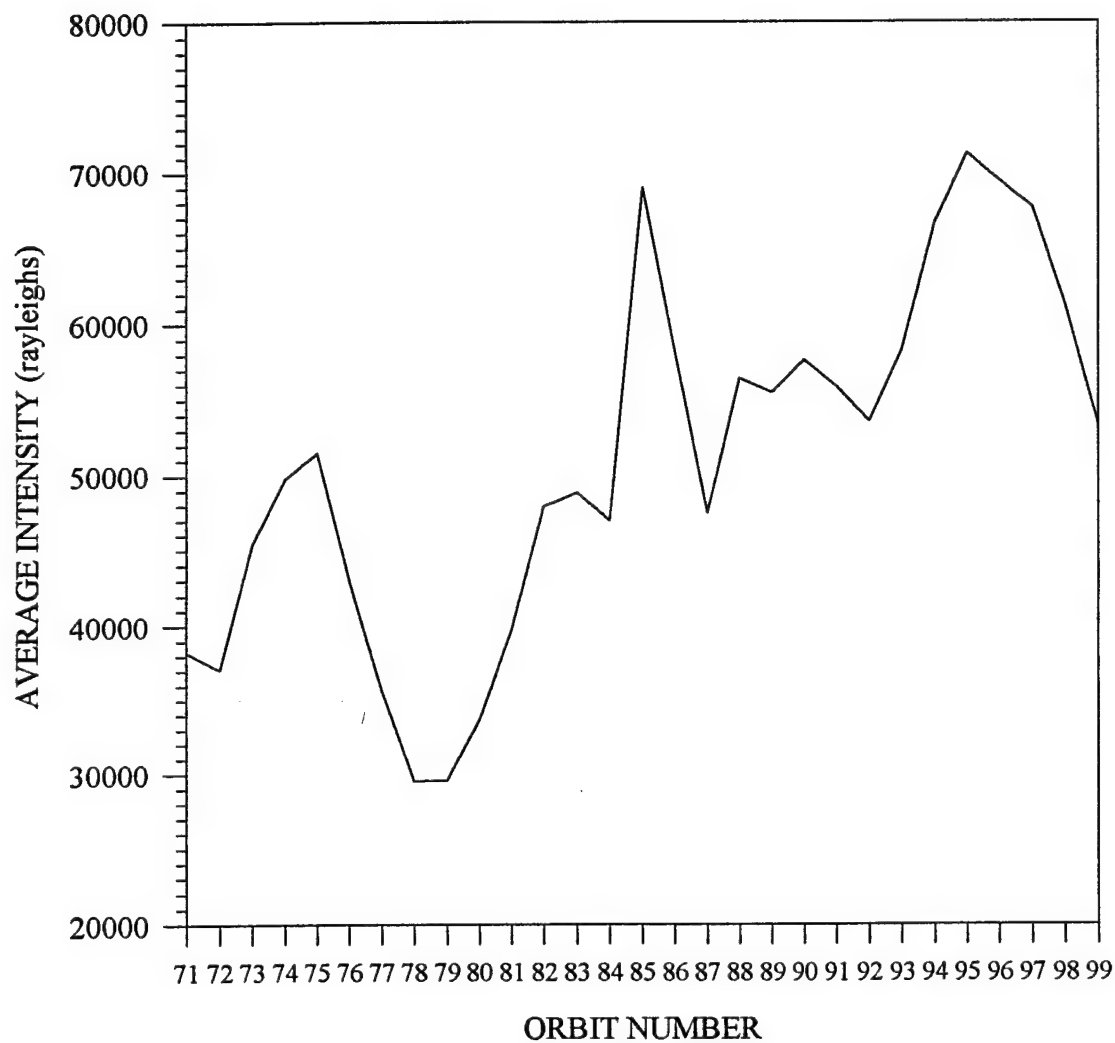
Figure 3.13. Average intensity of O_2 (0,0) for each orbit.

A measure of the total energy emitted in the O_2 (0,0) band during a night pass can be determined by averaging the intensity in each orbit. This is shown in Figure 3.13. There is a general upward trend, with average energy increasing by about a factor of 2 in the 2-day period. More remarkable is the variability in energy over short periods of time; Figure 3.13 shows a change in average intensity from 30 kR to 70 kR in only 6 orbits (9 hours elapsed solar time). With this high level of variability, it is not surprising that local brightness enhancements change significantly from orbit to orbit.

Since the geographic position of each 20 second spectrograph exposure is known, emission intensity can be examined as a function of latitude and longitude. The observation pattern is shown in Figure 3.8; about 80 exposures were recorded along each orbit track in this Figure. Figure 3.14 shows the geographical distribution of emission activity, but there is no obvious signature of organized wave activity. The average intensity along the meridians is shown in Figure 3.15. The intensity peaks in Figure 3.15 appear to have a characteristic width of about 25°, similar to the angular distance between orbital tracks (22.5°) shown in Figure 3.8. Since emission activity at the equator is low, this suggested emissions might exhibit a zonal variation

O₂(0,0) INTENSITY IN KILORAYLEIGHS AS A FUNCTION OF LATITUDE AND LONGITUDE
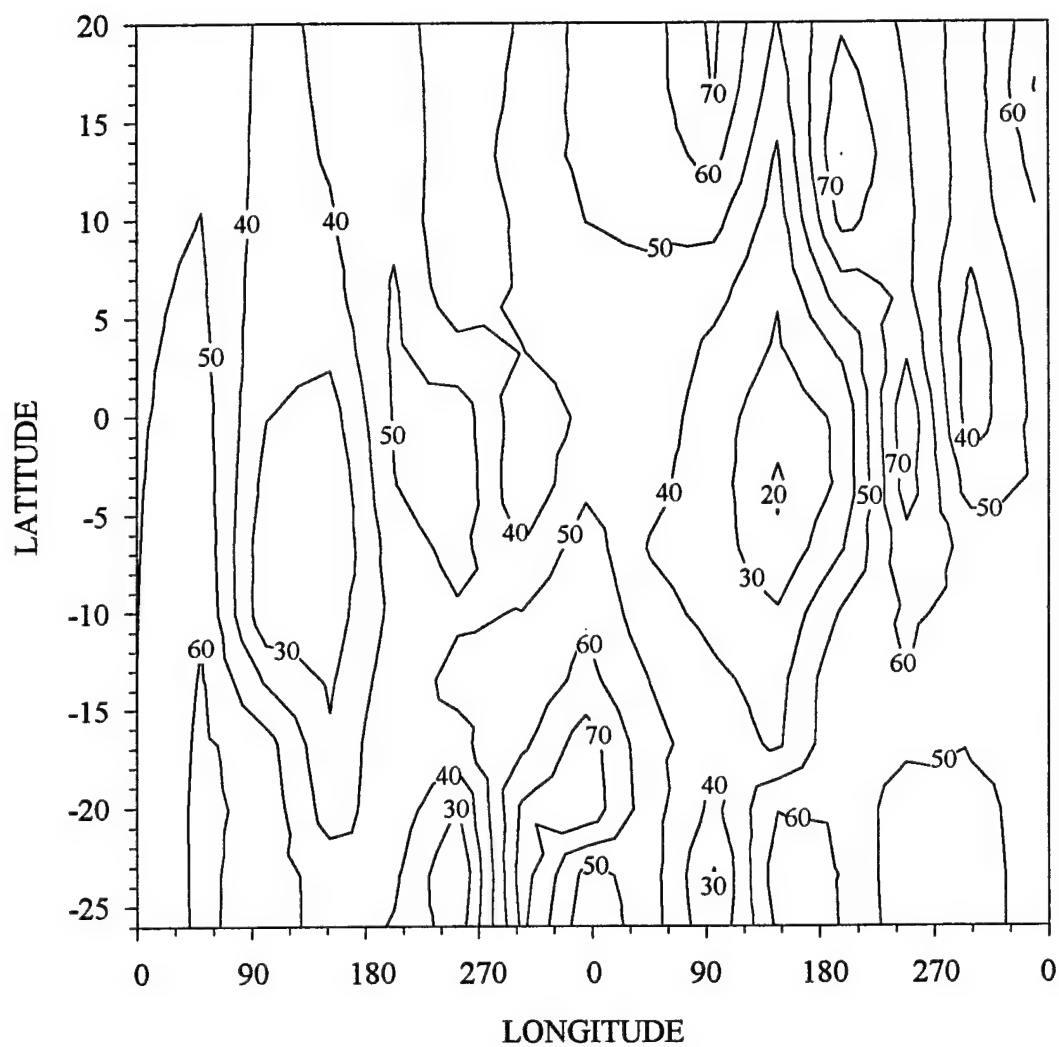
Figure 3.14. The geographical distribution of O_2 (0,0) intensity recorded by GLO.

moving from south to north. The intensity data were divided into three latitudinal zones: 28° S to 8° S (southern bin), 8° S to 8° N (equatorial bin), and 8° N to 28° N (northern bin). Then the meridional averages were again plotted in Figures 3.16a, 3.16b, and 3.16c to examine the emission activity in these zones. No periodicity is apparent in these Figures. The remarkable variations in local activity are still evident. Notice that in Figure 3.16a, the average intensity changes from a minimum of 18 kR to a maximum of 80 kR in 90° of longitude. Similar excursions are apparent in all three latitude bins. It may be significant that a deep minimum occurs at 130° longitude in all three bins, but otherwise, there seems to be no organized pattern of activity.

AVERAGED $O_2(0,0)$ INTENSITY BETWEEN
28° N and 28° S AS A FUNCTION
OF LONGITUDE FOR 29 ORBITS
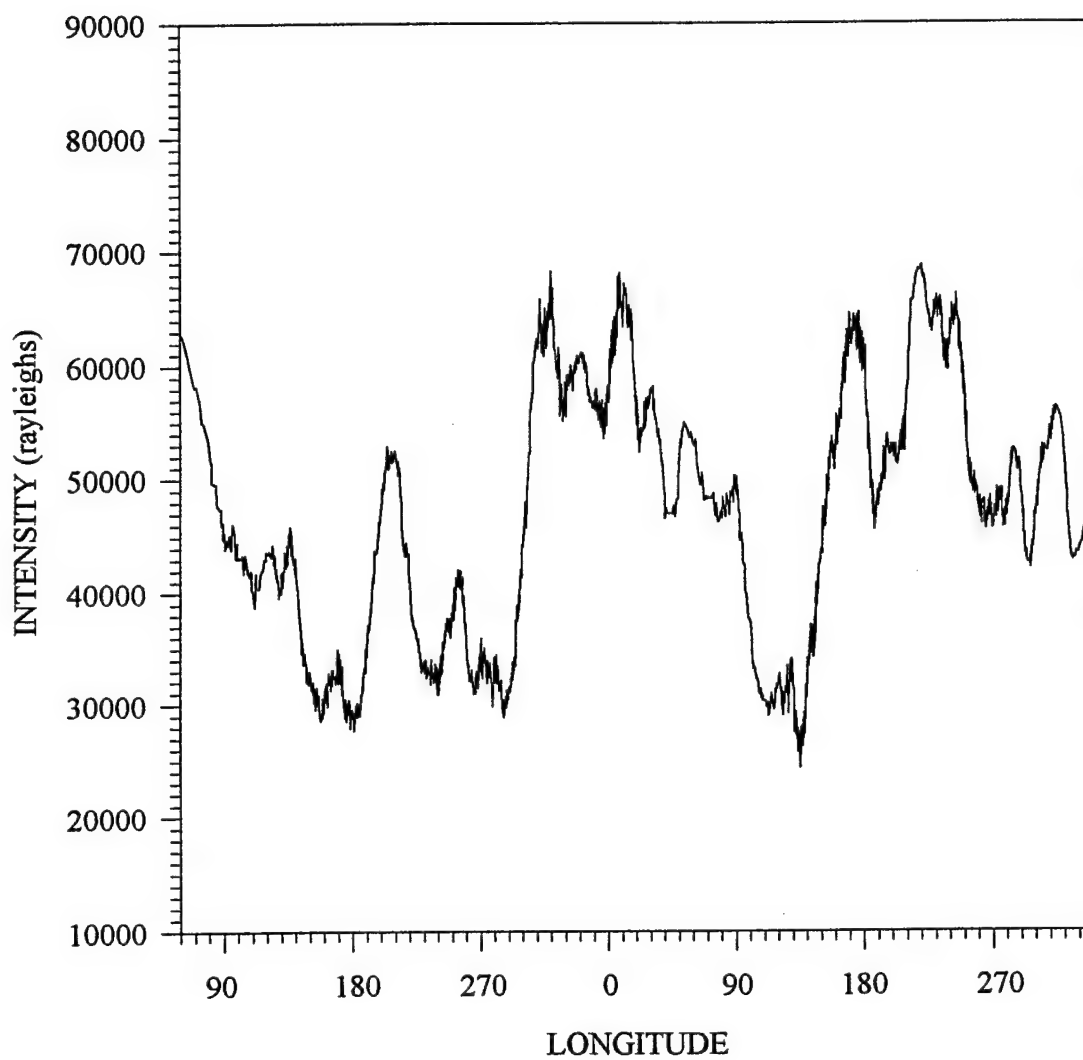
Figure 3.15. O_2 (0,0) intensity averaged in longitude over the latitude range of 28° N to 28° S.

AVERAGED $O_2(0,0)$ INTENSITY BETWEEN 28° S AND 8° S AS A FUNCTION OF LONGITUDE FOR 29 ORBITS
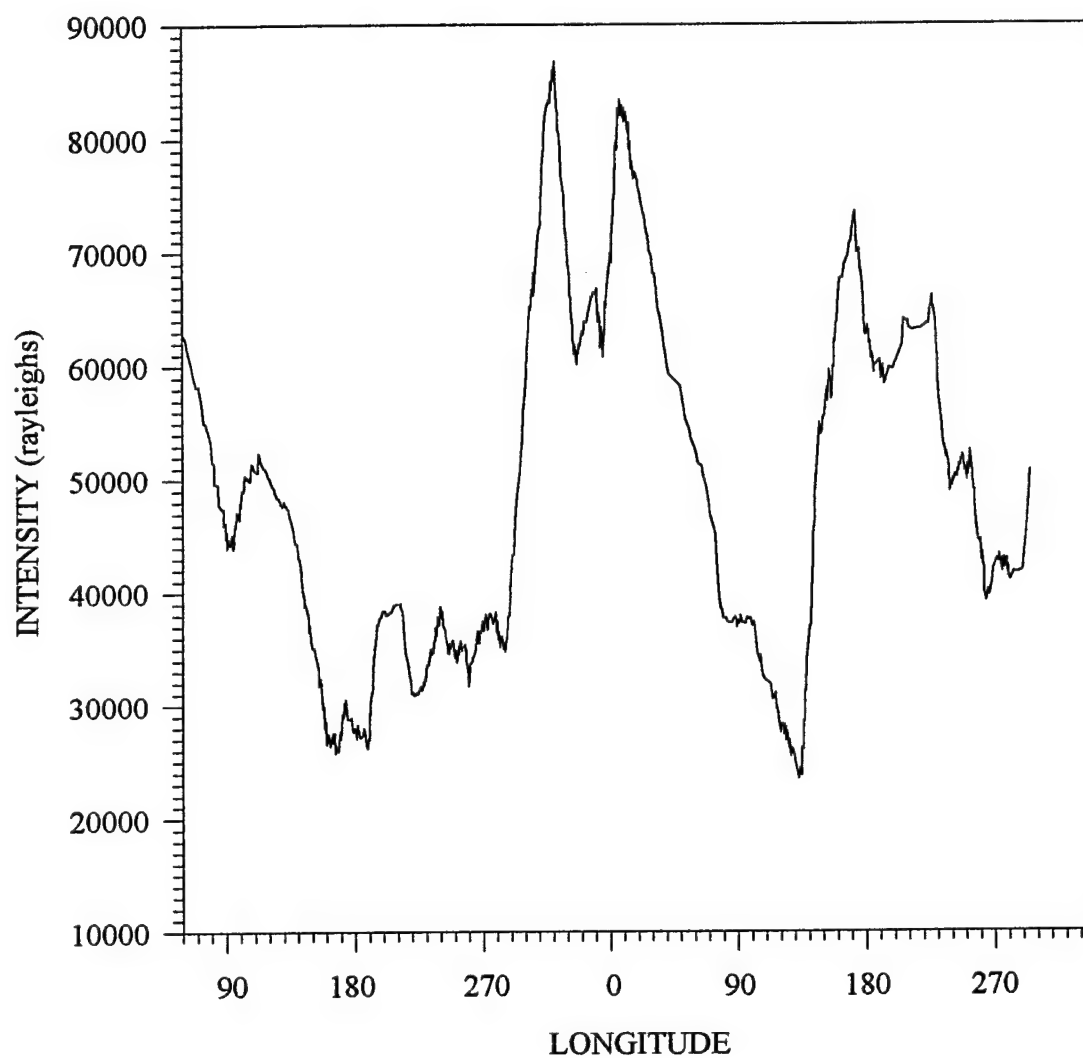
Figure 3.16a. The southern bin: O_2 (0,0) intensity averaged in longitude over the latitude range of 28° S to 8° S.

AVERAGED $O_2(0,0)$ INTENSITY BETWEEN
8° S and 8° N AS A FUNCTION
OF LONGITUDE FOR 29 ORBITS
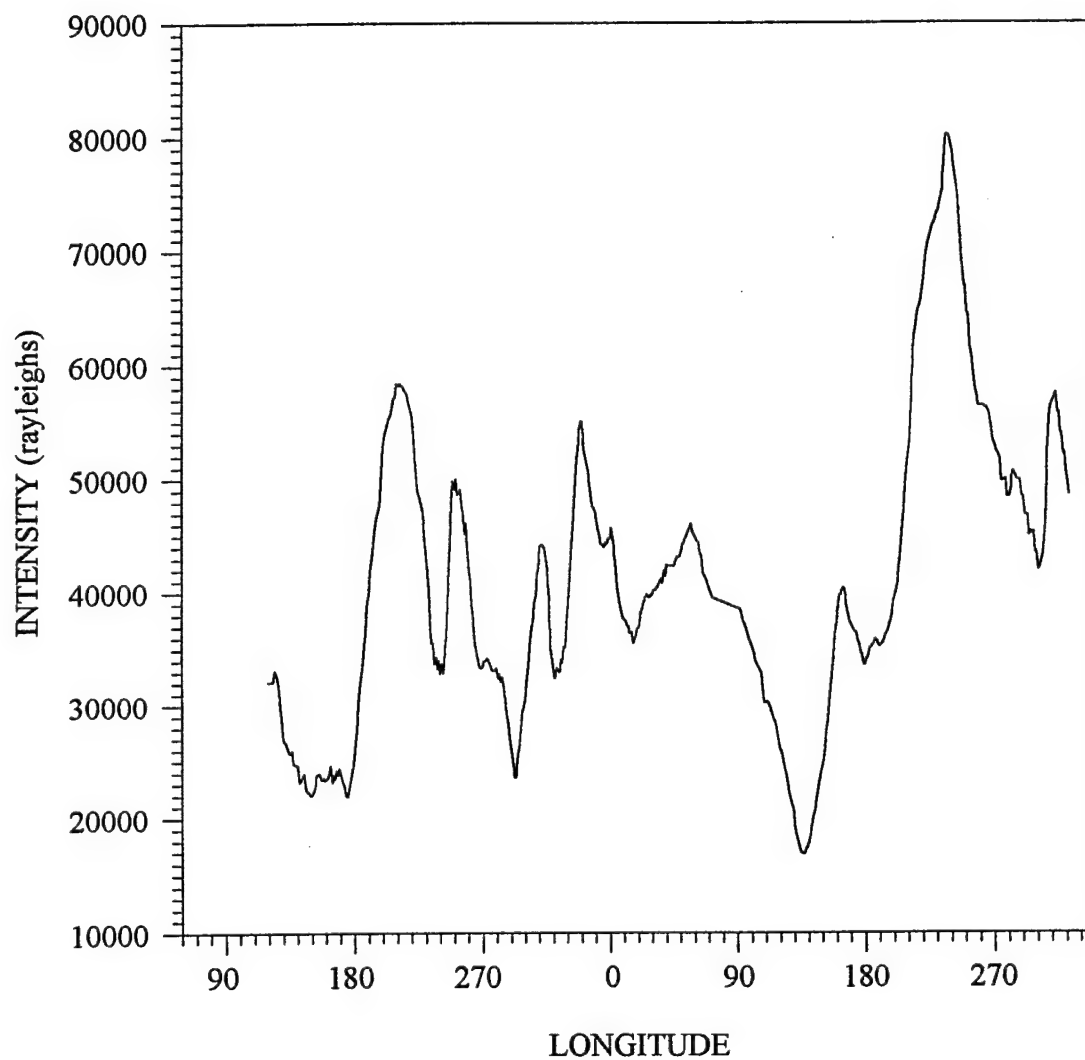
Figure 3.16b. The equatorial bin: O_2 (0,0) intensity averaged in longitude over the latitude range of 8° S to 8° N.

AVERAGED $O_2(0,0)$ INTENSITY BETWEEN
8° N AND 28° N AS A FUNCTION
OF LONGITUDE FOR 29 ORBITS
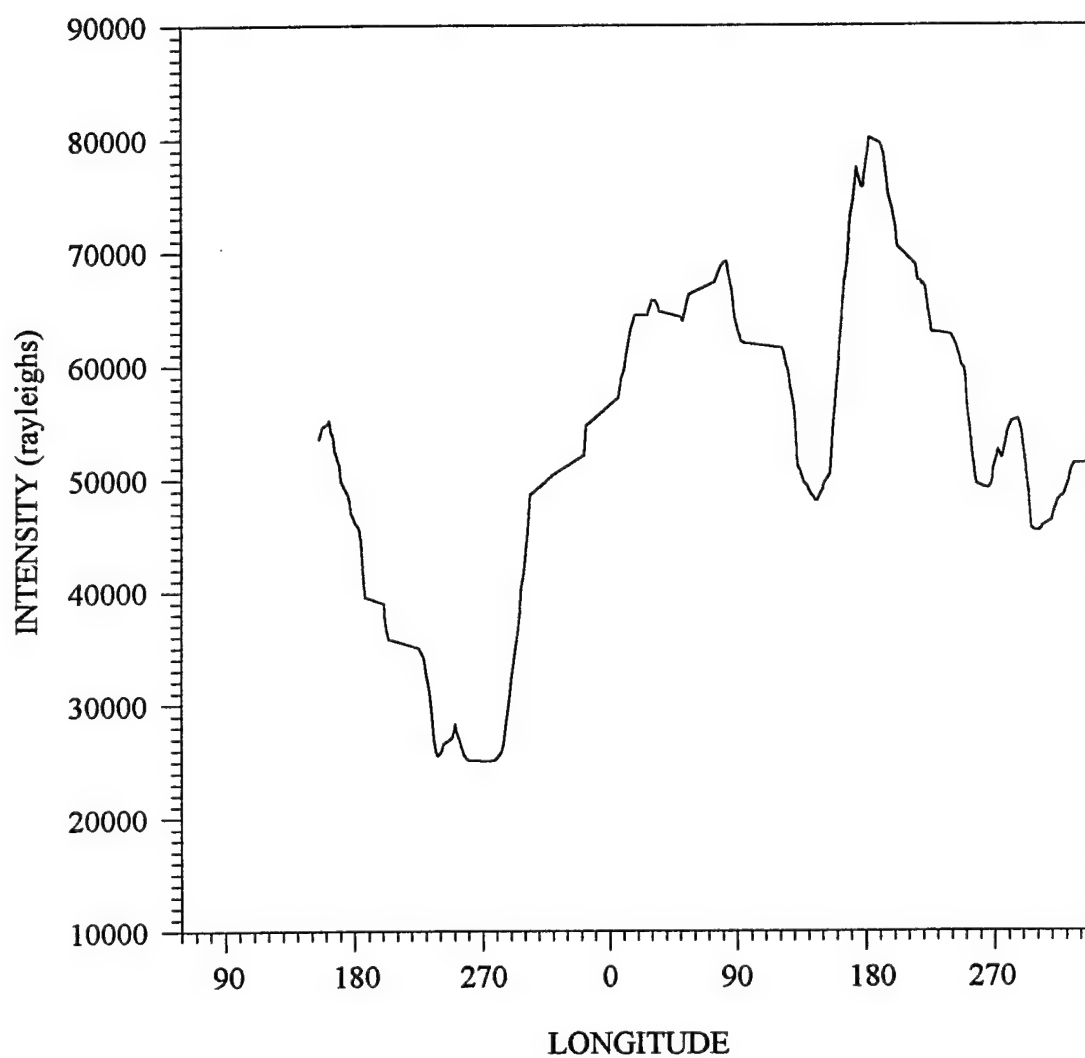
Figure 3.16c. The northern bin: O_2 (0,0) intensity averaged in longitude over the latitude range of 8° N to 28° N.

3.3 The O_2 (0,0) and O_2 (0,1) Atmospheric Bands Observed from Space

Up to this point, we have utilized the O_2 (0,0) band exclusively in this discussion of GLO observations of the night airglow. On the other hand, the O_2 (0,1) band has characterized the O_2 Atmospheric band system for ground-based aeronomers because the O_2 (0,0) band is self-absorbed and not observable from the surface. However, since the O_2 (0,0) band is 20.38 times brighter than the O_2 (0,1) band, it is the most intense emission seen from orbit. Although the intensity of the O_2 (0,0) emission makes it ideal for the work described in the previous section, the optical depth problem prevents this band from being useful for the study of airglow chemistry. Instead, the O_2 (0,1) band will be used for this purpose.

On the following pages, Figures 3.17 and 3.18 show plots of brightness in hundreds of rayleighs for O_2 (0,0) and (0,1) during orbit 72, in order to indicate the effects of optical depth on O_2 (0,0). The brightness of the O_2 (0,0) band is scaled down by a factor of 20.38, the ratio of the transition probabilities of O_2 (0,0) and O_2 (0,1) from the same upper state, in order to

compare the two emissions. Discrepancies between the O_2 (0,1) and scaled O_2 (0,0) brightness plots indicate the difference in the emission source functions.

The O_2 (0,1) emission isopleths in Figure 3.18 is shown to be shifted upward compared to the O_2 (0,0) isopleths in Figure 3.17, with a maximum at an altitude of about 85 km, 5 km higher than the O_2 (0,0) maximum. This is not surprising, since the O_2 (0,0) band originates from a surface close to the shuttle orbiter rather than from the limb, where the O_2 (0,1) band originates. The column brightnesses for both bands are very similar, but differences are apparent. Measurements of the O_2 (0,1) band intensity will be used in the discussion of atmospheric chemistry.

Figures 3.17 and 3.18 show orbit 72 exhibited multiple O_2 Atmospheric band maxima (at 20 LST, 24 LST, and 2.5 LST), with a secondary minimum at 21.5 LST and a deeper minimum at 1 LST. The minimum at 1 LST reflects a feature common to most night passes on average, as depicted in Figure 3.12, while the minimum at 21.5 LST is unique to this orbit.

SCALED-DOWN O_2 (0,0) BRIGHTNESS
IN HUNDREDS OF RAYLEIGHS
ORBIT 72
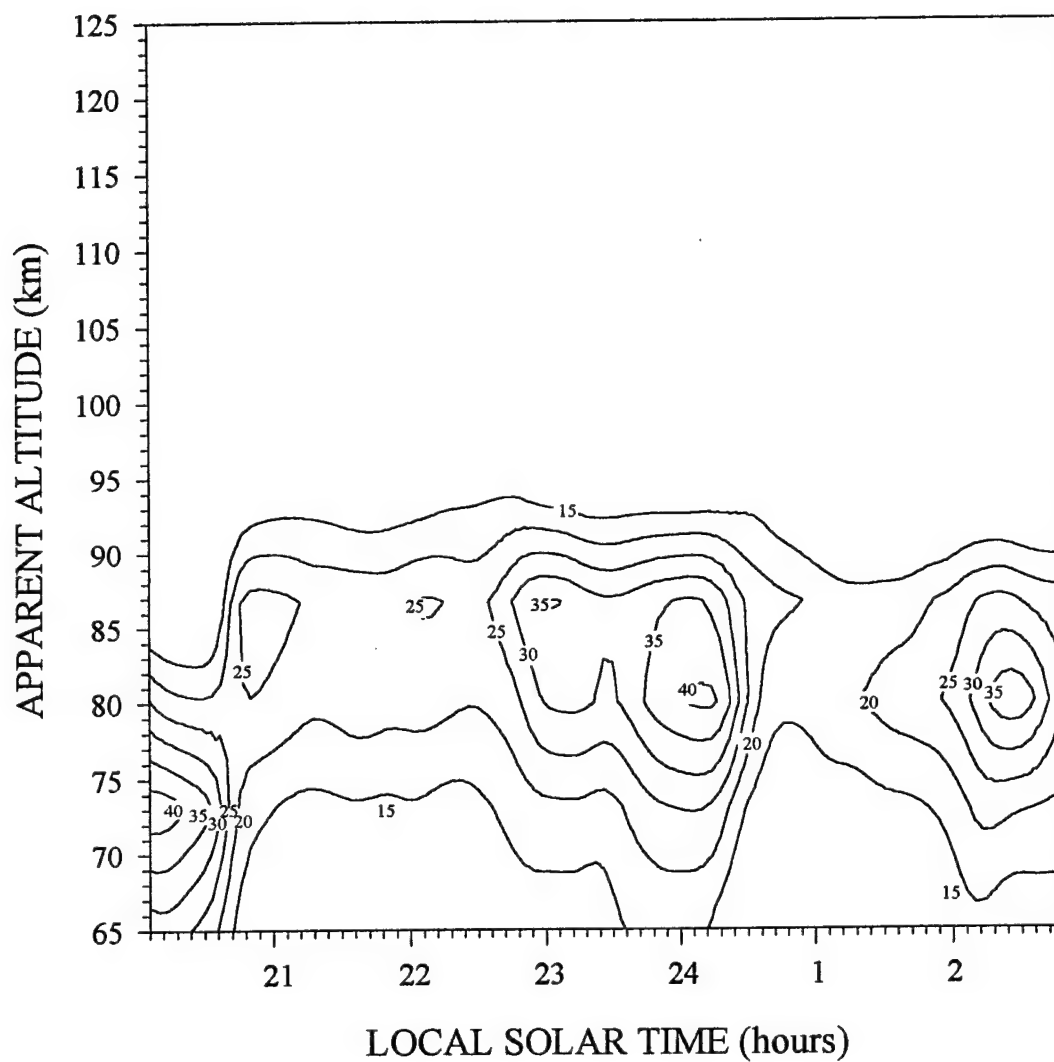
Figure 3.17. Scaled brightness in hundreds of rayleighs for the O_2 (0,0) band on orbit 72 as a function of altitude and local time.

O$_2$ (0,1) BRIGHTNESS IN
HUNDREDS OF RAYLEIGHS
ORBIT 72
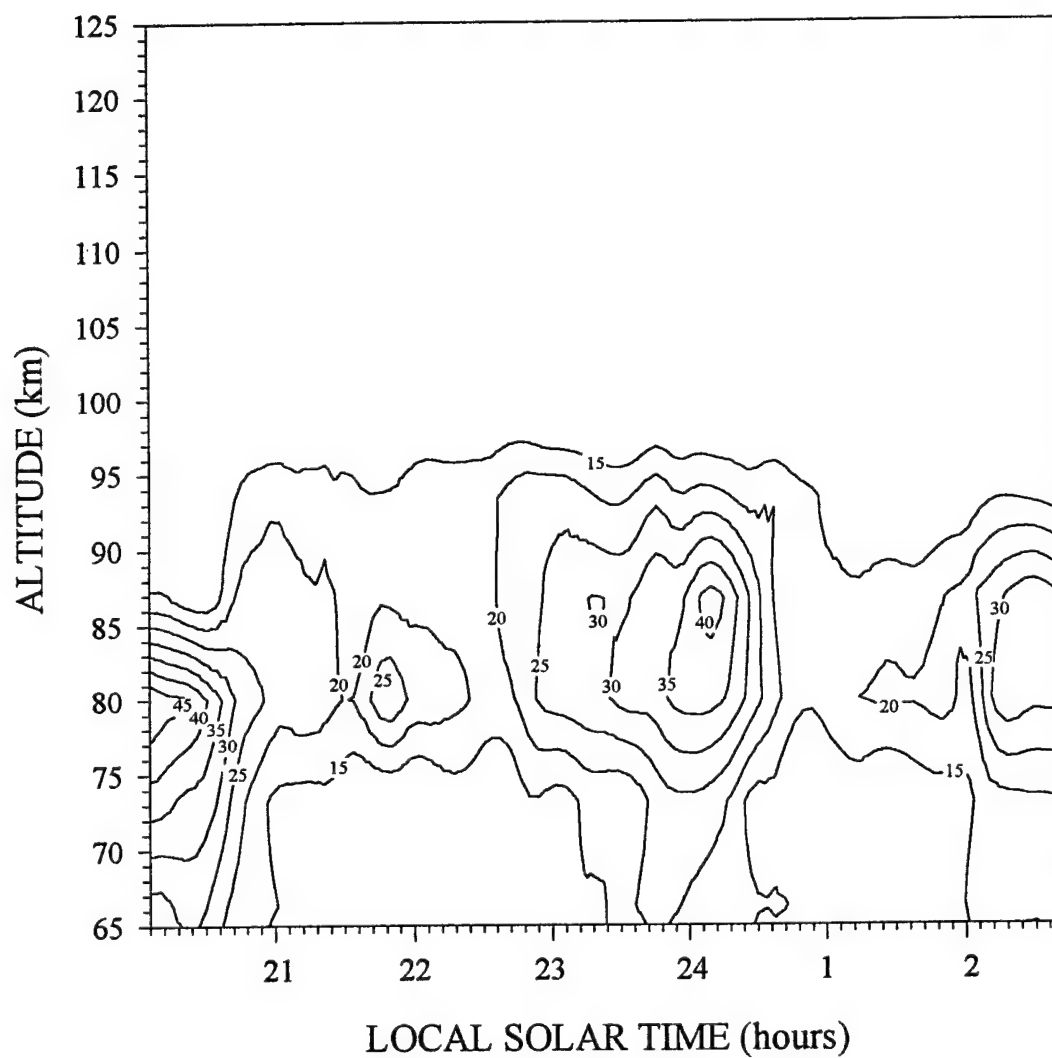
Figure 3.18. Brightness in hundreds of rayleighs for the O$_2$ (0,1) band on orbit 72 as a function of altitude and local time.

3.4 Spectral Signatures of Night Airglow Chemistry

The GLO data set is unrivaled in that it provides the first opportunity for an extensive examination of airglow emission characteristics recorded from a space platform. The unique feature of GLO observations is the capability to observe all the related emissions from the airglow layer simultaneously from a single column of gas, recorded at contiguous altitudes across the Earth's limb.

Figures 3.19a, 3.19b, and 3.19c on the following pages show the averaged intensity per orbit of the O_2 (0,0) band, 5577 Å, and the OH Meinel (6,2) band, respectively, as a function of orbit. Figure 1.19a has been repeated from Figure 3.13 for convenience. The O_2 (0,0) band and 5577 Å (Figures 3.19a and b) both show a trend of increasing intensity with successive orbits during the period, while the OH Meinel (6,2) band (Figure 3.19c) does not. Although the 5577 Å and O_2 (0,0) intensity plots are similar, 5577 Å shows a deep minimum at orbit 91, but O_2 (0,0) does not. The 5577 Å emission increased by about 260% between orbits 71 and 94, while O_2 (0,0) increased

by about 190%. The three emissions show no clear correlation, although it may be significant that there is a local peak in all emission on orbit 85.
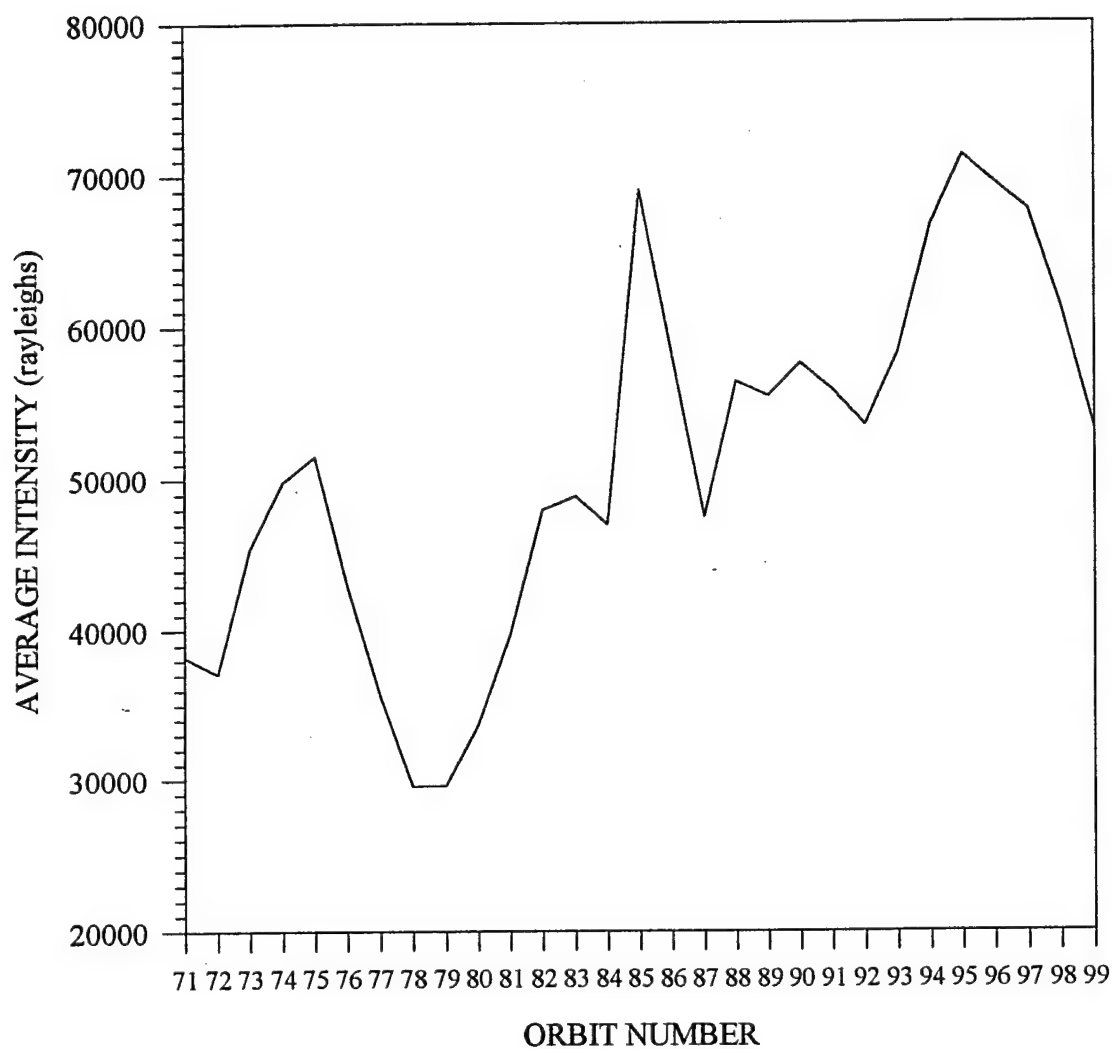
Figure 3.19a. Average intensity of O_2 (0,0) for each orbit.

AVERAGE INTENSITY OF OI (5577 Å)
AS A FUNCTION OF ORBIT
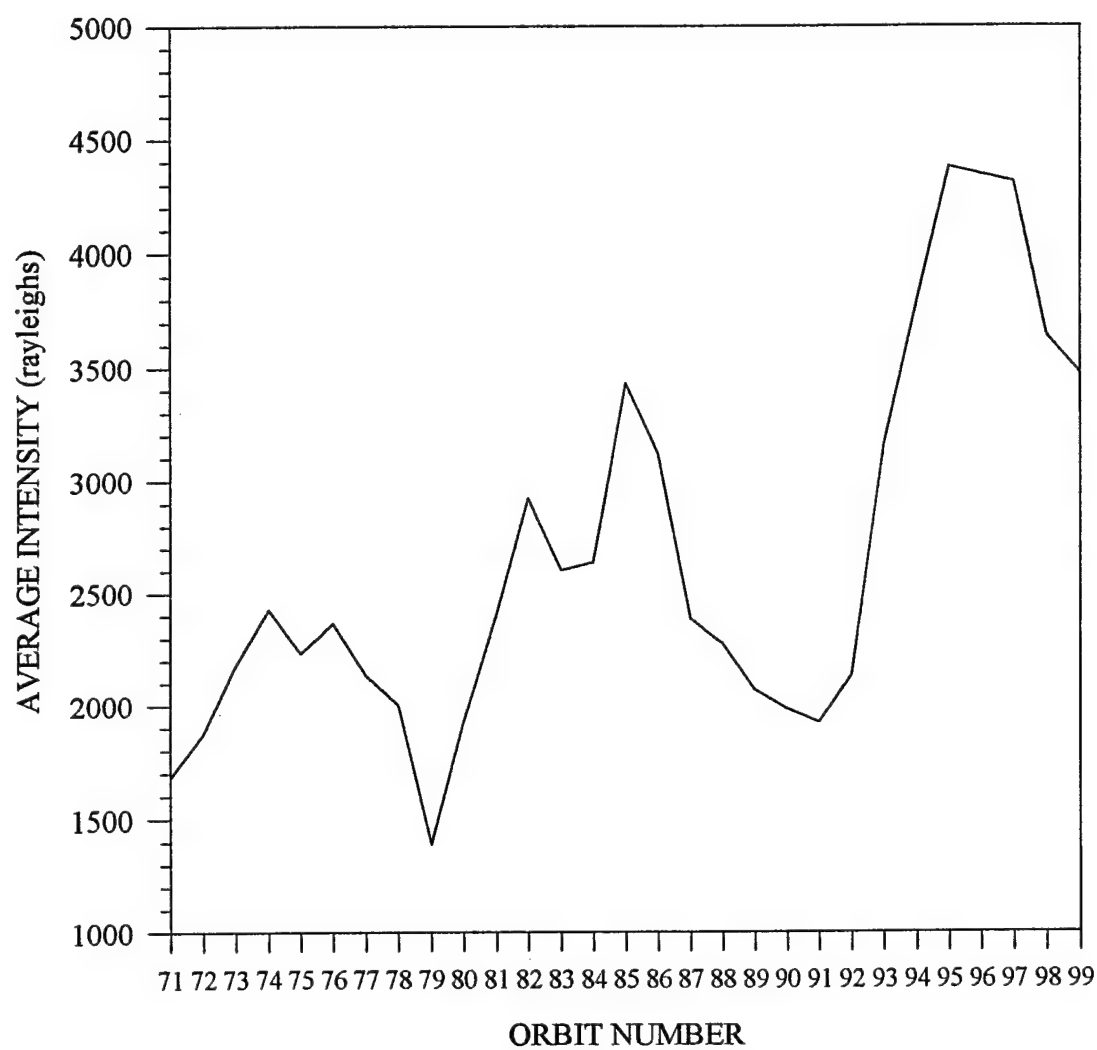
Figure 3.19b. Average intensity of OI (5577 Å) for each orbit.

AVERAGE INTENSITY OF OH (6,2)
AS A FUNCTION OF ORBIT
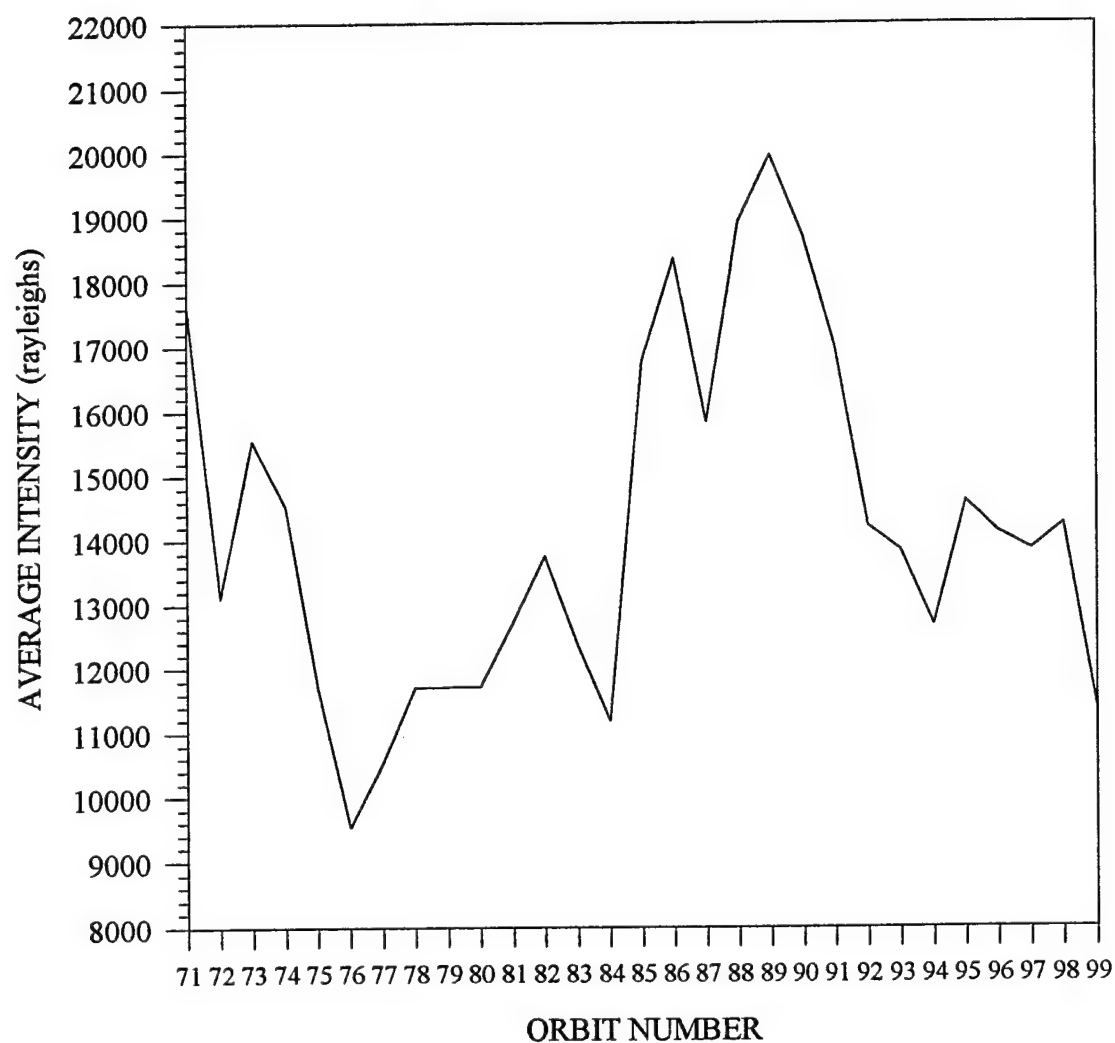
Figure 3.19c. Average intensity of OH Meinel (6,2) for each orbit.

Column intensities recorded by GLO can be inverted to determine volume emission rate profiles for the various species. Volume emission rate is directly proportional to density of emitting species, and thus is a indicator of airglow chemistry. The data from three successive orbits (85 through 87) were inverted for this study. The inversion required application of the Abel integral (Hassani, 1991), using an algorithm provided by Dasch (Appendix D). Orbits 85 through 87 are representative of the data set and were chosen for their clear signatures of dynamic behavior in the night airglow. The profiles for emissions of O_2 (0,1), OI (5577 Å), and OH Meinel (6,2) during orbits 85 through 87 are shown in Figures 3.20 through 3.22, each Figure being a set of three (a, b, and c, respectively).

The shuttle passed over the South Atlantic Anomaly between 20 and 22 LST during orbit 86 (Figures 3.21a, b, and c). The Anomaly is a region of weak geomagnetic field above the coast of Brazil. Energetic charged particle bombardment of GLO spectrograph B (see Table 2.1) in this part of the orbit created sufficient noise to render O_2 (0,1) data useless until just after 22 LST. Data for OH Meinel (6,2), also recorded by the same spectrograph, shows

evidence of noise just before 22 LST, but is not otherwise affected. Data for 5577 Å recorded by spectrograph C was not affected during this period.

Ground-based observations over the years have led to the belief that night airglow emissions are organized and coherent. Such orderly behavior is not seen from orbit. The plots for orbits 85 through 87, each separated by only 90 minutes in real time, are certainly evidence of greater dynamism in the night airglow than is generally recognized. Figures 3.20 through 3.22 show that the volume emission rates for O_2 (0,1), 5577 Å, and OH (6,2) are dynamic and poorly organized. They exhibit a chaotic pattern of emission variations that changes significantly on time scales of hours or less in real time. Observations from orbit provide a completely different view of the night airglow than ground-based observations.

Table 3.1 below summarizes the emission variations seen in Figures 3.20 through 3.22. The Table reports maximum and minimum volume emission rates at the same altitude for a given emission, as well as the time of occurrence and the maximum-to-minimum ratio.

	O$_2$ (0,1)		OI (5577 Å)		OH (6,2)	
Orbit 85						
Maximum	1300	22.2 LST	750	2.6 LST	5500	23.7 LST
Minimum	< 200	0.7 LST	100	0.6 LST	2000	1.7 LST
Max/Min Ratio	>6.5		7.5		2.75	
Orbit 86						
Maximum	1000	2.0 LST	1150	1.5 LST	6500	22.2 LST
Minimum	< 200	0.5 LST	100	0.3 LST	2000	1.2 LST
Max/Min Ratio	>5.0		11.5		3.25	
Orbit 87						
Maximum	900	2.2 LST	750	2.2 LST	6500	23.6 LST
Minimum	< 200	0.5 LST	100	0.2 LST	2000	1.3 LST
Max/Min Ratio	>4.5		7.5		3.25	

Table 3.1. Observed emission enhancements during STS-69 orbits 85 through 87.

Note that although the altitudes for the O$_2$ (0,1) and OH Meinel peak emission only varied by about 1 km over the three orbits, the peak emission in 5577 Å rose from about 96 km to 100 km. Figure 3.23 and 3.24 give averaged vertical profiles describing Regions I and II as indicated on orbit 86. Regions I and II were chosen to emphasize that emissions are not correlated.

O$_2$(0,1) VOLUME EMISSION RATE
(photons cm^{-3} sec^{-1})
ORBIT 85
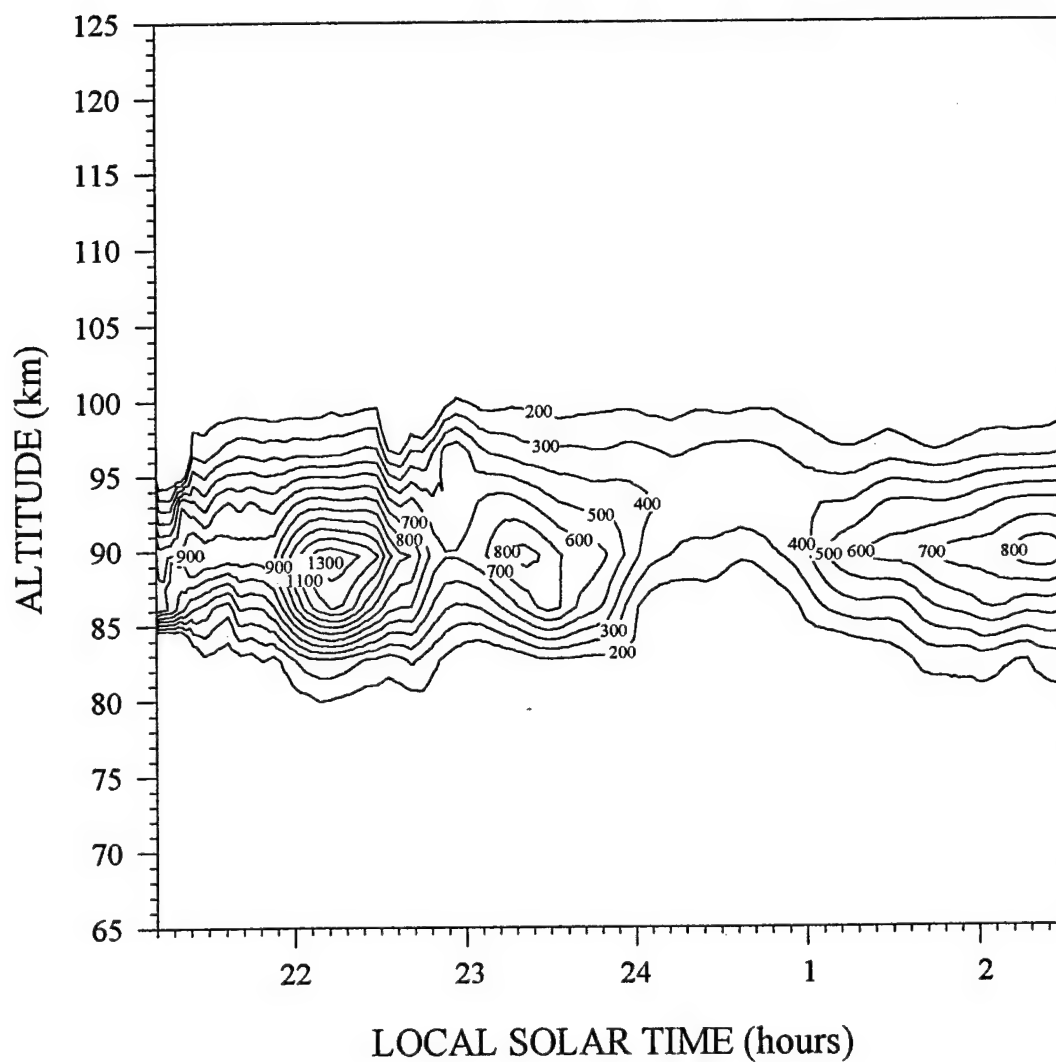
Figure 3.20a. Volume emission rate for the O$_2$ (0,1) band on orbit 85 as a function of altitude and local time.

OI (5577 Å) VOLUME EMISSION RATE
(photons cm^{-3} sec^{-1})
ORBIT 85
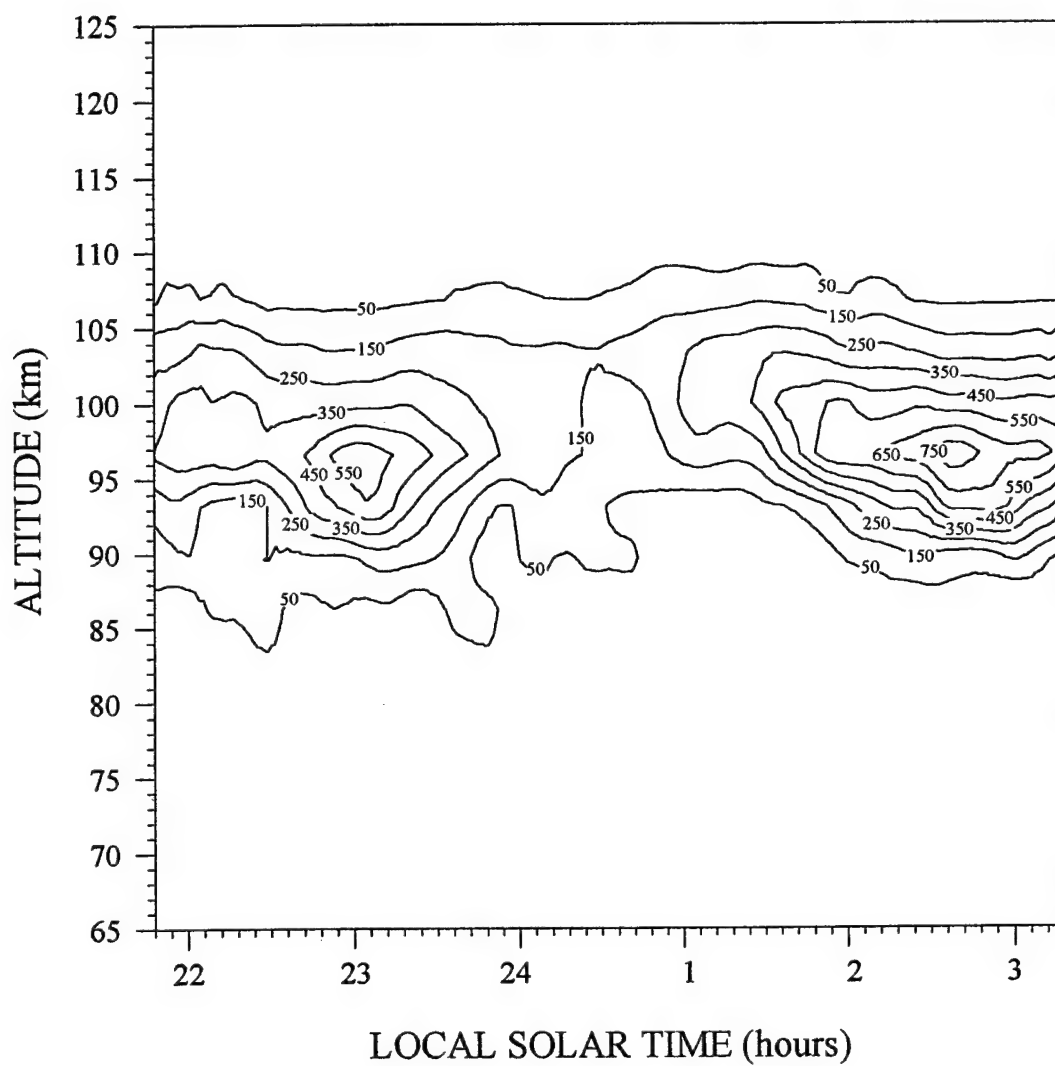
Figure 3.20b. Volume emission rate for OI (5577 Å) on orbit 85 as a function of altitude and local time.

OH (6, 2) VOLUME EMISSION RATE
(10^2 photons cm^{-3} sec^{-1})
ORBIT 85
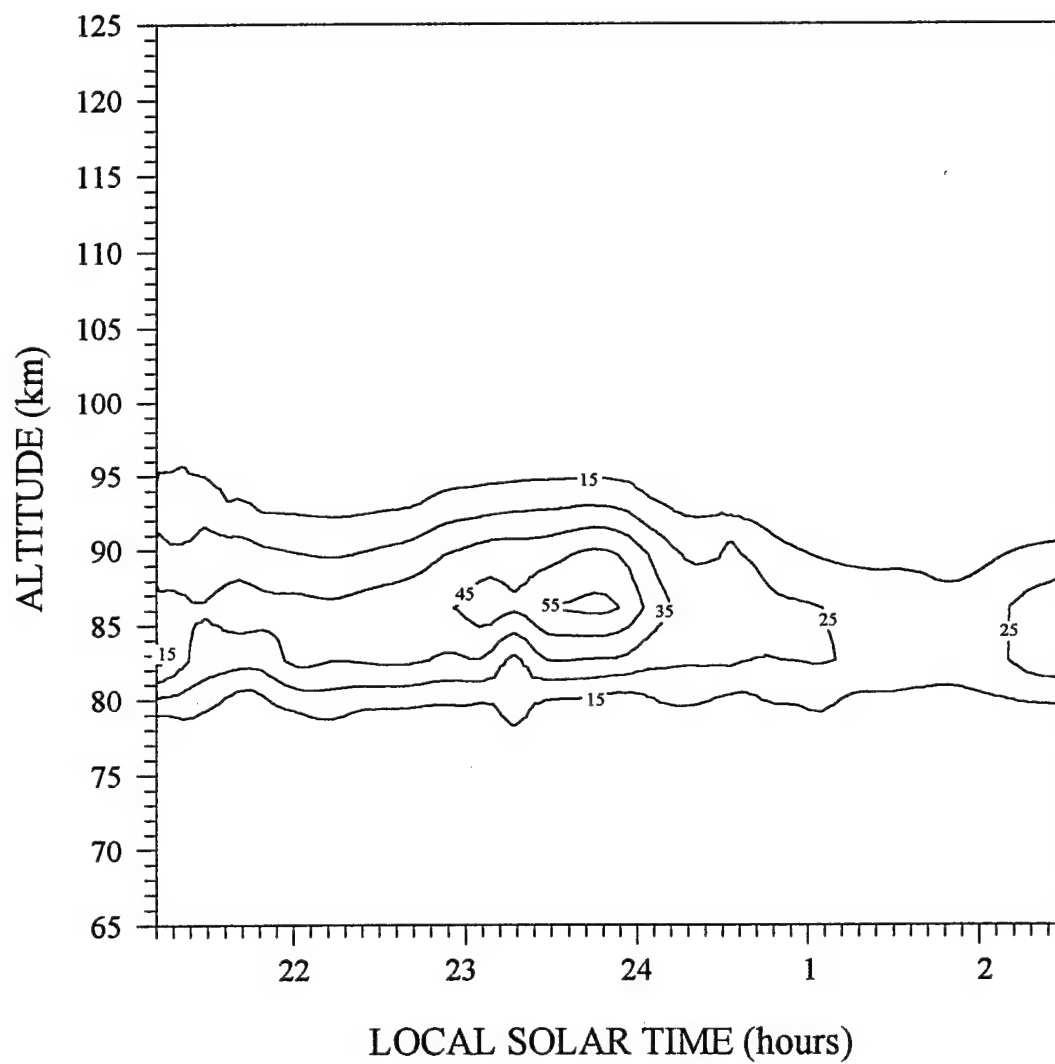
Figure 3.20c. Volume emission rate for the OH Meinel (6,2) band on orbit 85 as a function of altitude and local time.

O$_2$ (0,1) VOLUME EMISSION RATE
(photons cm^{-3} sec^{-1})
ORBIT 86
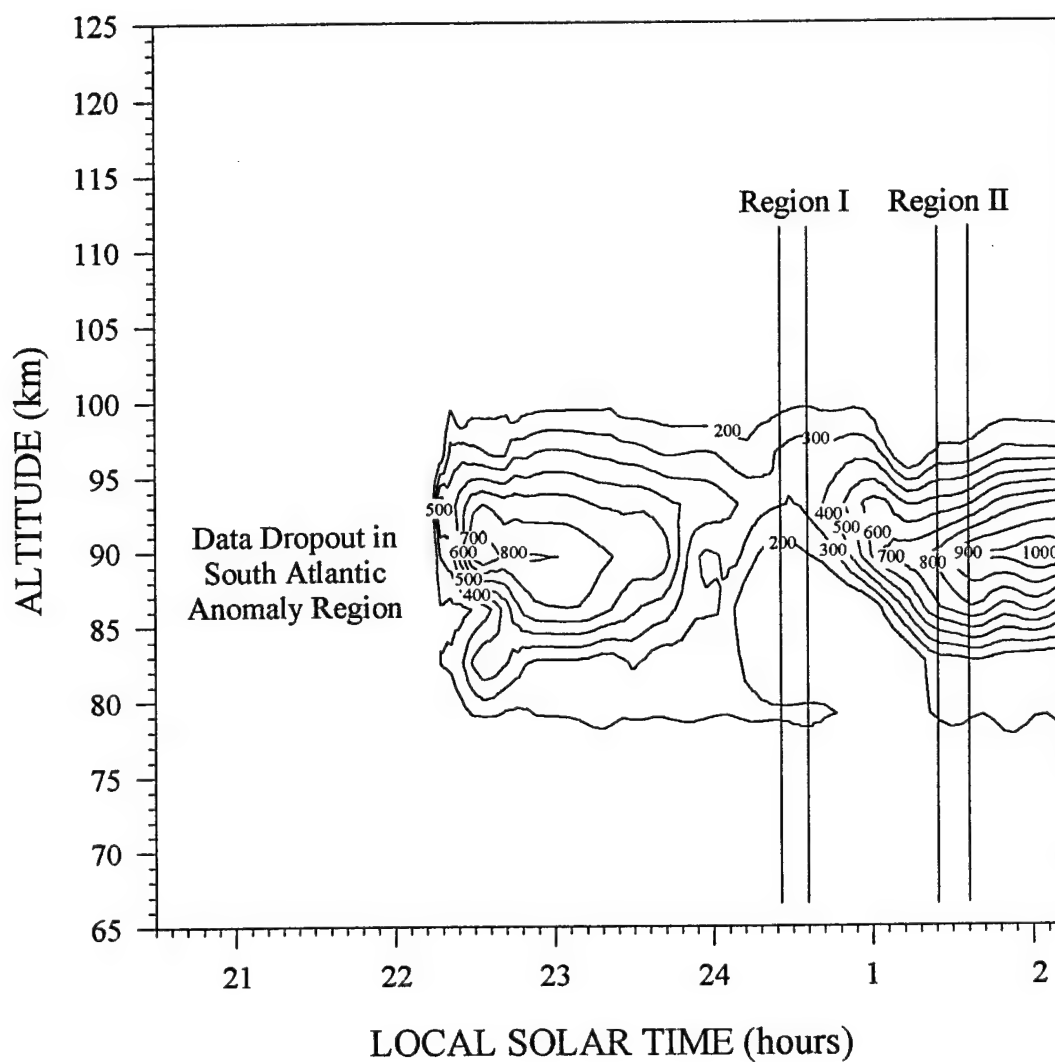
Figure 3.21a. Volume emission rate for the O$_2$ (0,1) band on orbit 86 as a function of altitude and local time.

OI (5577 Å) VOLUME EMISSION RATE
(photons cm^{-3} sec^{-1})
ORBIT 86
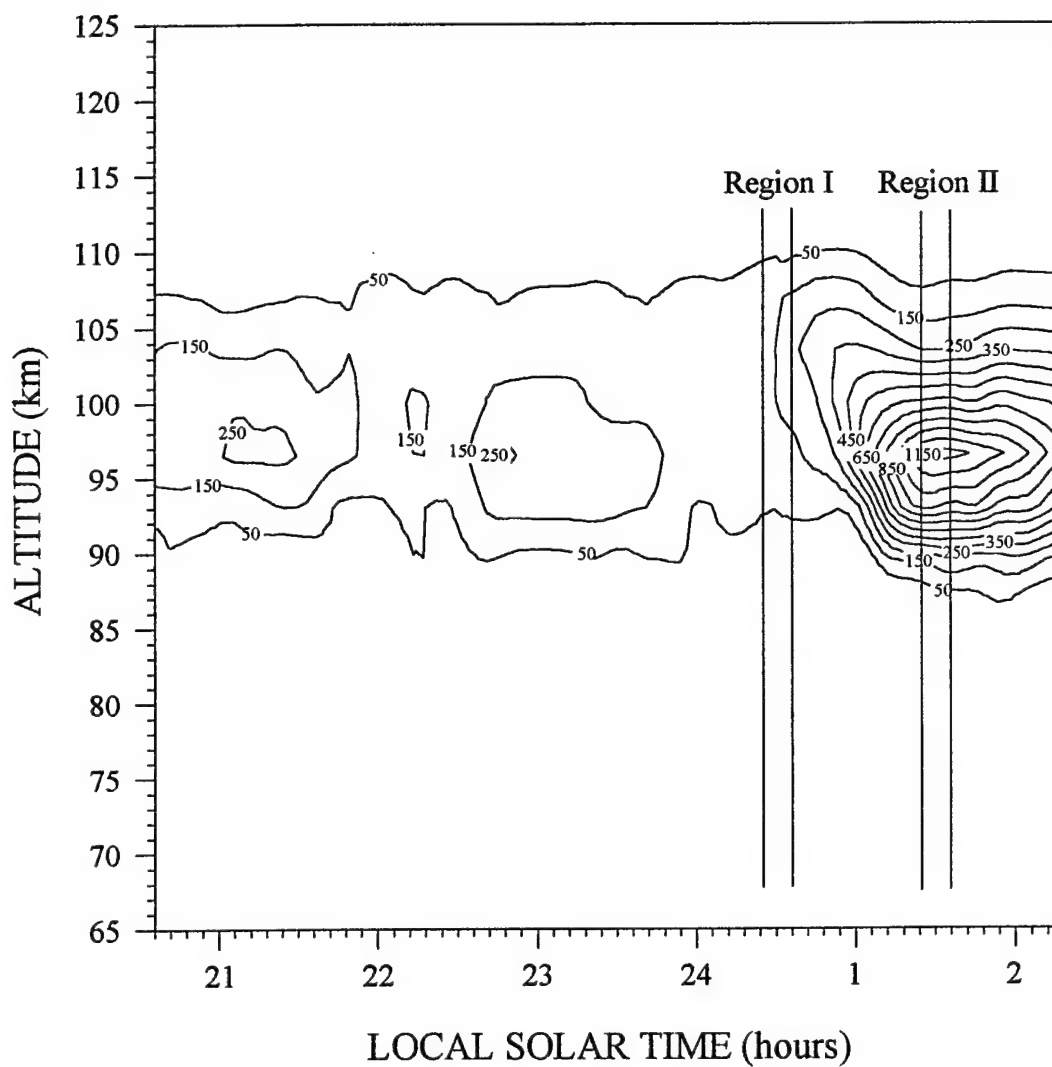
Figure 3.21b. Volume emission rate for OI (5577 Å) on orbit 86 as a function of altitude and local time.

OH (6, 2) VOLUME EMISSION RATE
(10^2 photons cm^{-3} sec^{-1})
ORBIT 86
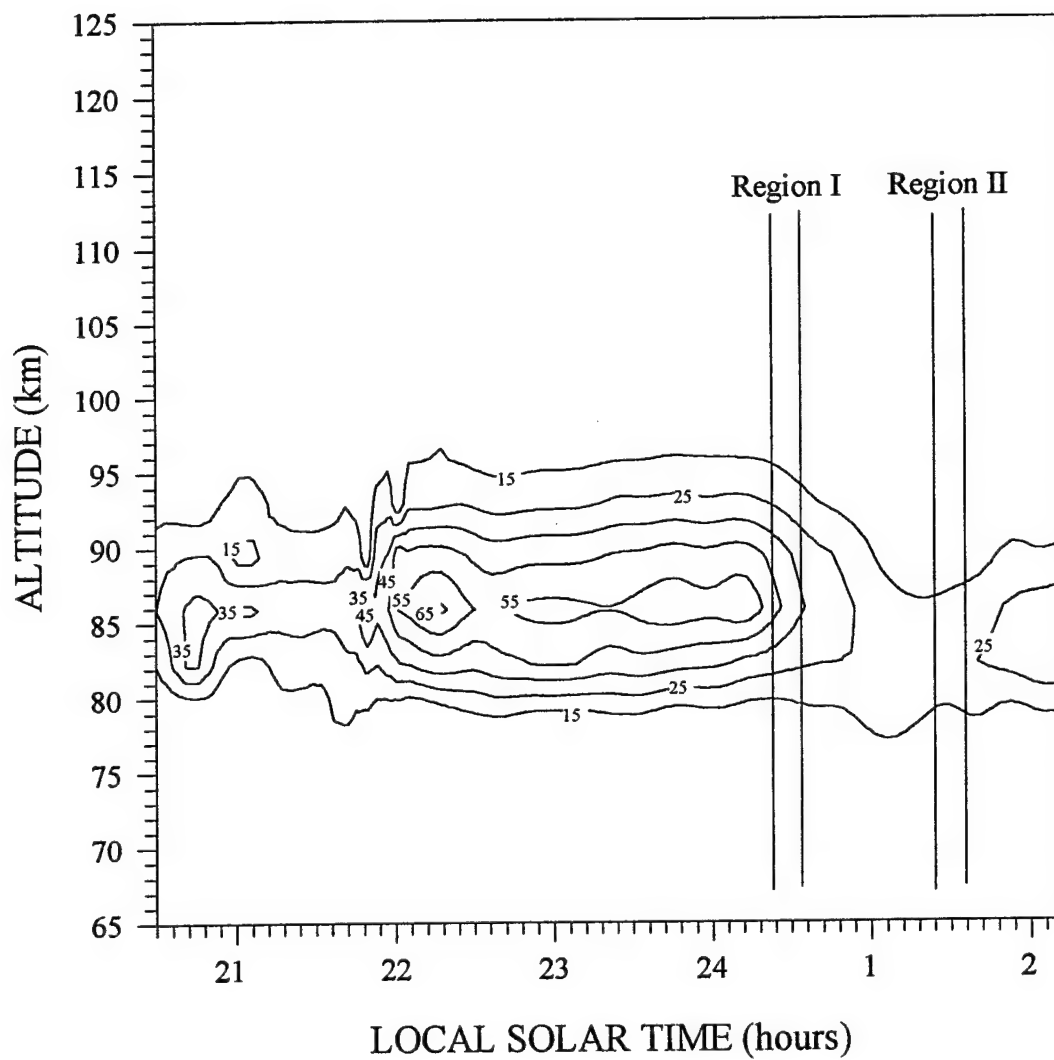
Figure 3.21c. Volume emission rate for the OH Meinel (6,2) band on orbit 86 as a function of altitude and local time.

O$_2$ (0,1) VOLUME EMISSION RATE
(photons cm^{-3} sec^{-1})
ORBIT 87
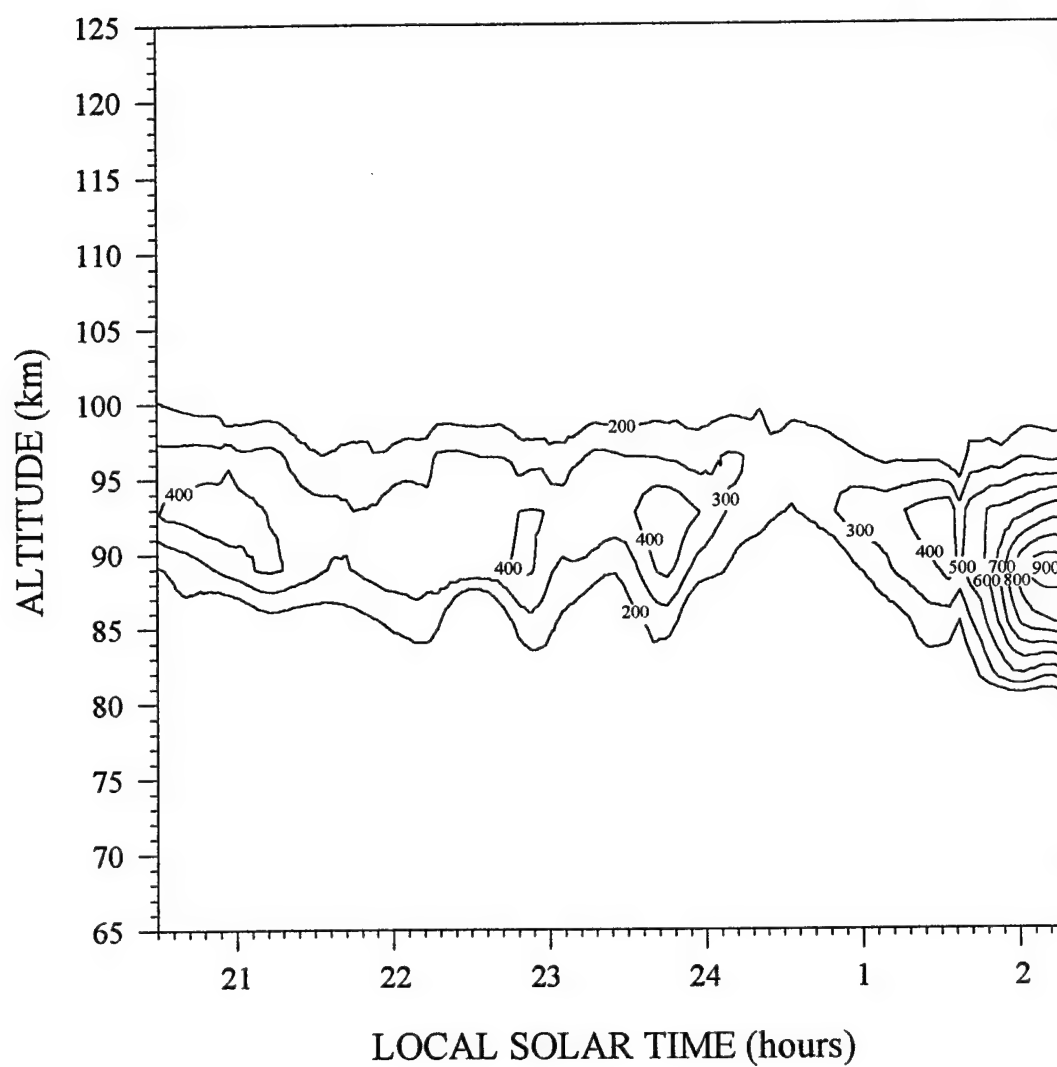
Figure 3.22a. Volume emission rate for the O$_2$ (0,1) band on orbit 87 as a function of altitude and local time.

OI (5577 Å) VOLUME EMISSION RATE
(photons cm^{-3} sec^{-1})
ORBIT 87
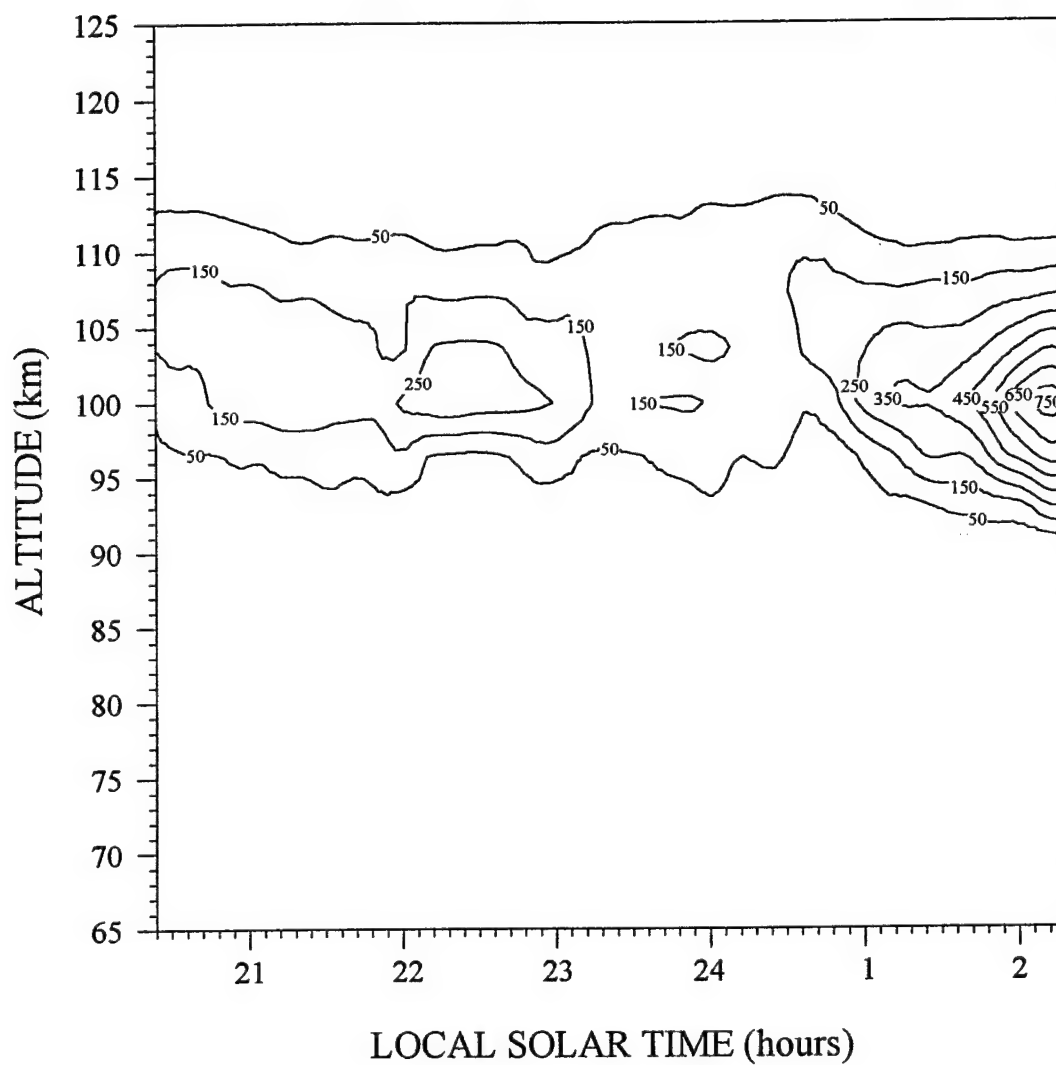
Figure 3.22b. Volume emission rate for OI (5577 Å) on orbit 87 as a function of altitude and local time.

OH (6, 2) VOLUME EMISSION RATE
(10^2 photons cm^{-3} sec^{-1})
ORBIT 87
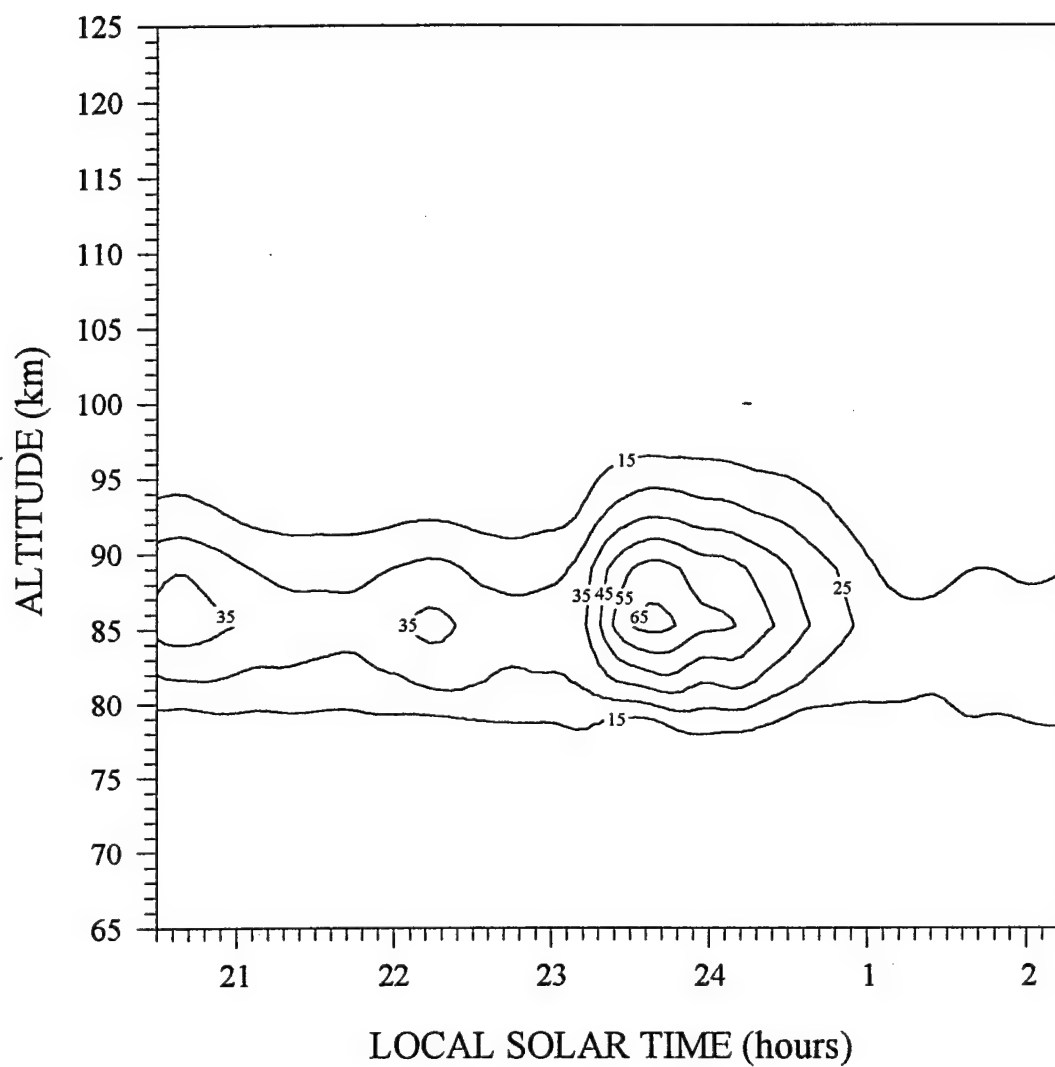
Figure 3.22c. Volume emission rate for the OH Meinel (6,2) band on orbit 87 as a function of altitude and local time.

Figures 3.23 and 3.24 illustrate that the night airglow emissions of O_2 (0,1), OI (5577 Å), and OH (6,2) are not coupled. Figure 3.23 shows the vertical profiles of volume emission rates averaged between 0.4 and 0.6 LST on orbit 86 (Region I), about one hour after the emission maximum for OH Meinel (6,2), but when O_2 (0,1) and 5577 Å emissions were near their minimums. Figure 3.24 shows the vertical profiles one hour later on orbit 86 (Region II), averaged between 1.4 and 1.6 LST. Here, 5577 Å emission was at maximum, O_2 (0,1) emission was nearly at maximum, and OH Meinel (6,2) emission was near minimum. These plots are not smooth because of discrete sampling along the spectrograph slit, but they indicate the lack of temporal and spatial correlation among the three emissions. Over an hour, 5577 Å and O_2 (0,1) emissions varied by about a factor of 5, while OH (6,2) varied by about a factor of 2. The emission maxima of OI (5577 Å) is about 7 to 10 km higher than that of O_2 (0,1), while peak emission of O_2 (0,1) is, in turn, about 7 km higher than peak emission for OH (6,2).

VOLUME EMISSION RATES
AVERAGED OVER 0.2 HOUR
ORBIT 86
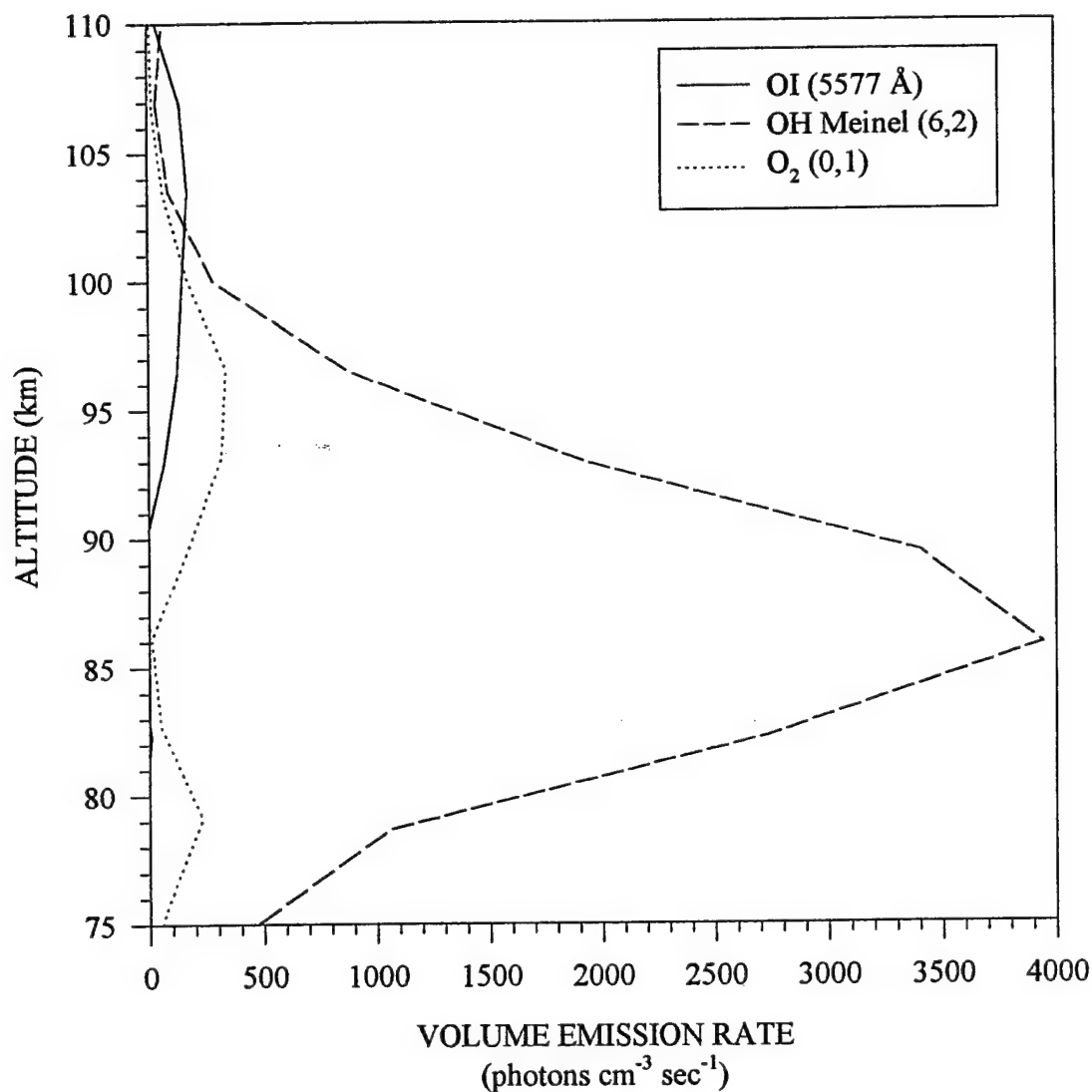
Figure 3.23. Volume emission rates for airglow emissions averaged over 0.2 hour between 0.4 and 0.6 LST on orbit 86 (Region I). OH Meinel (6,2) emission was moderate while 5577 Å and O_2 (0,1) emissions were at or near minimum at this time.

VOLUME EMISSION RATES
AVERAGED OVER 0.2 HOUR
ORBIT 86
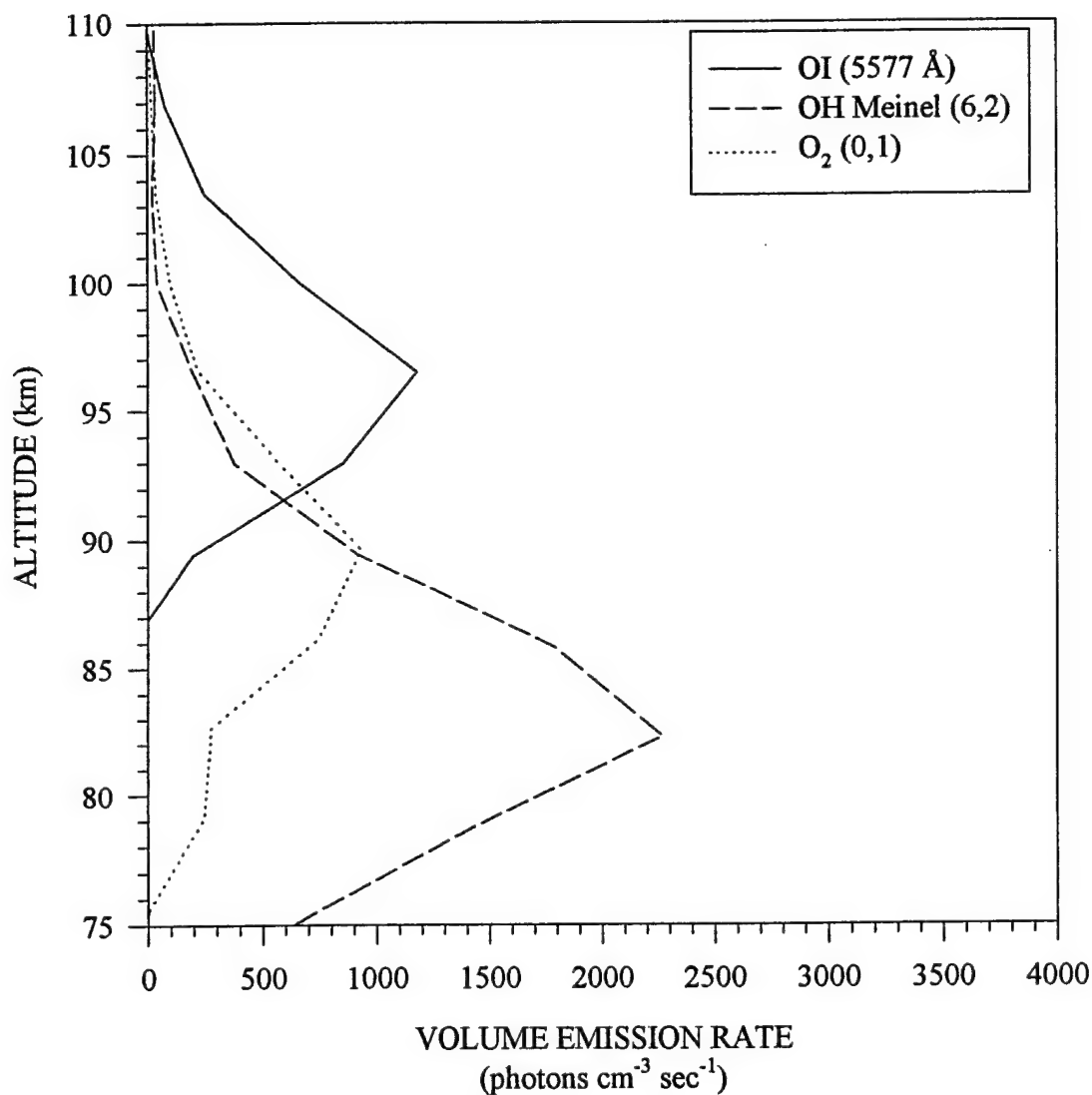
Figure 3.24. Volume emission rates for airglow emissions averaged over 0.2 hour between 1.4 and 1.6 LST on orbit 86 (Region II). OH Meinel (6,2) emission was near minimum while 5577 Å and O_2 (0,1) emissions were at or near maximum at this time.

3.5 Comparisons of GLO Data with the Johnston-Broadfoot Model

The Johnston-Broadfoot model, outlined in Appendix F, assumes statically stable conditions. GLO data presented here shows this assumption is far from reality. However, the model can provide a baseline against which observations can be compared.

Sensitivity studies using the Johnston-Broadfoot model indicate that emissions at 5577 Å on the one hand, and emissions in the OH Meinel and O_2 Atmospheric bands on the other hand, react very differently to changes in ambient number density [M] (= [N_2] + [O_2]) and oxygen density [O] in the airglow layer. By *increasing* ambient number density [M] in the model (as might be caused by upwelling from below), emissions at 5577 Å *decrease* as a result of enhanced quenching of [O*], while emissions in the OH Meinel and O_2 Atmospheric bands *increase* as a result of enhanced production. When O concentration alone is *increased* (as might be caused by subsidence from above), emissions at 5577 Å and in the O_2 Atmospheric bands *increase*, while OH Meinel band emissions remain almost unchanged, exhibiting only a

slight increase. Vertical transport is assumed to be important in the creation of the localized emission activity detected in the GLO data set. Upwelling and subsidence effects are examined here with respect to the predictions of the Johnston-Broadfoot model.

The [O] and [M] inputs to the Johnston-Broadfoot model can be varied as desired. Simple upward shift of [M] values in the input data array with respect to altitude simulates an upwelling. Increasing [O] by a constant factor simulates the accumulation of subsiding O from above. Varying the input profiles of eddy viscosity above 90 km simulates atmospheric turbulence and gravity wave "breaking" (turbulent dissipation), which is presumed to be ubiquitous at altitudes near 100 km (the so-called "turbopause").

Table 3.2 summarizes the results of varying key parameters in the Johnston-Broadfoot model. The Table indicates that only upwelling in a relatively *shallow* layer enhances O_2^* emissions, while upwelling in general increases OH* emissions while decreasing O* emissions. Increased [O] enhances all emissions. Molecular viscosity changes, even by a factor of 10

(whether increases or decreases), do not seem to significantly affect any emissions. Increasing eddy viscosity enhances both O_2* and OH* emissions while leaving O* emissions unchanged. Decreasing eddy viscosity by a factor of 10 produces negligible effects for all emissions.

Parameter	Change in Parameter	Change in $[O_2*]$	Change in $[OH*]$	Change in $[O*]$
[M]	5 km uplift	× 1.35	× 1.63	× 0.65
[M]	10 km uplift	Negligible	× 2.15	× 0.24
[M]	20 km uplift	× 0.17	Negligible	× 0.01
[O]	× 2	× 3.17	× 1.67	× 7.84
[O]	× 3	× 5.98	× 2.11	× 24.7
[O]	× 4	× 9.20	× 2.45	× 54.8
[M] & [O]	[M] × 2 & [O] × 2	× 2.58	× 1.86	× 2.80
[M] & [O]	[M] × 2 & [O] × 3	× 7.94	× 3.63	× 18.3
Eddy Viscosity	× 10	× 1.17	× 1.20	Negligible
Eddy Viscosity	× 20	× 1.26	× 1.34	Negligible
Eddy Viscosity	× 0.1	Negligible	Negligible	Negligible
Molecular Viscosity	× 10 or × 0.1	Negligible	Negligible	Negligible
Molecular Viscosity	5 km uplift	Negligible	Negligible	Negligible

Table 3.2. Results of varying input parameters in the Johnston-Broadfoot model.

An increase in [O] by a factor of 2 in the Johnston-Broadfoot model changes [O*] and [OH*] by factors of 7.84 and 1.67, respectively. This

closely parallels the emission changes by factors of 7.5 and 2.75 actually observed for 5577 Å and OH (6,2) on orbit 86, as shown in Table 3.1. However, the model indicates that increasing [O] by a factor of 2 is not sufficient to raise $[O_2*]$ by the factor of 6.5 seen on orbit 86, suggesting that upwelling [M] as well as subsiding [O] caused the O_2 (0,1) emission peak. The model predicts that upwelling decreases $[O*]$. The enhancements on orbit 87 by factors of 5.0, 11.5, and 3.25 for O_2 (0,1), 5577 Å, and OH (6,2) emissions are similar to model output factors of 5.98, 24.7, and 2.11 for an [O] increase by a factor of 3. However, a blend of upwelling and subsidence is again suggested because of the discrepancy between predicted and actual 5577 Å enhancement. Model output for an [O] increase by a factor of 2 again closely matches the actual observations on orbit 87, and more closely matches the smaller increase in O_2 (0,1) emission on this orbit. Since upwelling from below and subsidence from above need not be mutually exclusive events, we can conclude that the two effects could compete to determine the actual emission enhancements observed by GLO. This is consistent with the scale of local dynamics inferred during the search for organization on a more global scale in Section 3.2.

A separate test for temperature sensitivity in the Johnston-Broadfoot model was performed. Using an extreme temperature increase of 40 K at peak in a vertically symmetric layer, changes were negligible and nearly all species emissions were slightly *decreased*, with only the OH Meinel bands seemingly unaffected by the temperature change. Model output does not appear to support the contention that temperature variations *in situ* can directly force the brightness changes observed. Model output, however, cannot simulate the secondary effect of temperature variations: namely, the destruction of static stability and the creation of vertical motions, which undoubtedly will change [M] and [O].

The production of O_2^* (excited state molecular oxygen) is determined by the three body association reaction $O + O + M \rightarrow O_2^* + M$ (Step I of the Barth process described in Chapter 1). We see that O_2 emissions, being proportional to the number density $[O_2^*]$, should vary as $[M][O]^2$, and are strongly dependent on the number density of ground state atomic oxygen (Shepherd et al., 1995). With O_2 emissions (and thus $[O_2^*]$) varying by factors of three or more, we see that [O] must vary by a factor of about two to

explain our observations during STS-69, assuming [M] does not change. Similarly, since the production reaction for excited state atomic oxygen is Step II of the Barth process, $O_2^* + O \rightarrow O_2 + O^*$, we see that variations in O^* (neglecting quenching effects) must follow the product $[O_2^*][O]$, or alternatively $[M][O]^3$. This product gives an enhancement factor of 6, if $[O_2^*]$ increases by a factor of 3 and [O] increases by 2. This is in good agreement with the variations of O^* emissions actually observed in the GLO data set.

Quenching caused by the increases in ambient density [M] and atomic oxygen [O] must be taken into account. O_2^* is primarily quenched by collisions with N_2, which has a concentration roughly equal to 0.78 [M], while O^* is quenched both by O and O_2. The quenching rate coefficient for O_2^* and N_2 is 2×10^{-15} cm^3 s^{-1}; for O^* and O_2, 3×10^{-13} cm^3 s^{-1}; and for O^* and O, 7.5×10^{-12} cm^3 s^{-1} (Vallance Jones, 1974). Although O is 25 times more efficient than O_2 at quenching O^*, O_2 is so much more numerous than O that O^* losses caused by O^*-O_2 collisions are 40 times greater than the losses caused by O^*-O collisions. Upwelling motions will increase $[O_2]$ and $[N_2]$, enhancing both production and quenching of O_2^* and OH^* by [M], but

increased production dominates the increased quenching in this case. However, O* quenching by [M] will dominate O* production whenever [M] is increased, as, for example, in upwelling from lower altitudes. Thus, chemistry considerations indicate that GLO data are consistent with vertical transport of reactants into the airglow layer.

A measure of the severity of quenching is the altitude at which an emission is reduced to half its unquenched rate. This parameter is known as the quenching height, h_Q. Above h_Q, quenching quickly becomes negligible, while below h_Q, quenching is extreme. The greater h_Q for a given emission, the greater that emission's sensitivity to quenching.

For example, the atomic oxygen line at 6300 Å has a quenching height between 250 and 350 km, and it is not observed at airglow layer altitudes. For the 5577 Å emission, h_Q ranges from 95 to 115 km. For the O_2 (0,0) emission, h_Q is about 95 km (Vallance Jones, 1974). The tendency here is for O* to be more sensitive to quenching than O_2*. The h_Q for the OH Meinel band is not well established. Figures 3.20 through 3.24 indicate OH emission is reduced

when 5577 Å emission increases, possibly as a result of subsidence of O.

This would imply OH quenching by O with the reaction $O + OH \rightarrow O_2 + H$.

Thus, h_Q for OH Meinel emissions could be quite variable, depending on the

dynamics of the downward flow of O into the MTI region at night.

3.6 Comparisons of GLO Data with Previous Observations

GLO data from STS-69 agrees in general with observations reported in both historical and contemporary research. The uniqueness of the GLO data set provides insight into the nature of night airglow chemistry and dynamics. In particular, GLO observed evidence for the dynamic influence of vertical winds on night airglow emissions.

Airglow parameters based on previous research, the Johnston-Broadfoot model, and the inversion of GLO data (Appendix D) are shown in Table 3.3. Parameters based on rocket observations are marked by the symbol "^," while orbital observations and model output references are unmarked. The volume emission rate for the O_2 (0,0) band marked with the symbol "*" was estimated by multiplying the rate for the O_2 (0,1) band by 20. The results of Shepherd et al. and Ward et al. referenced in Table 3.3 come from data recorded by the WINDII instrument on board UARS. Observations from orbit, such as those by GLO and WINDII, can capture airglow variations on a planetary scale, unlike spatially isolated and short duration rocket data.

EMISSION FEATURE	PEAK VOL EMISSION RATE photons/cm³/sec	PEAK ALT km	FWHM km	SOURCE
O$_2$ (0,0)	No estimate	89-95	10	Ward et al., 1995
	2400-11000	88-96	5-12	^López-González et al., 1992a
	4800	94	13	^Murtagh, 1995
	8000-26000*	89-93	11-13	This dissertation, 1997
	1600	94	10	Johnston-Broadfoot Model, 1992
O$_2$ (0,1)	No estimate	88-96	5-12	^López-González et al., 1992a
	400-1300	89-93	11-13	This dissertation, 1997
	78	94	10	Johnston-Broadfoot Model, 1992
5577 Å	100 - 400	92-97	5-7	^López-González et al., 1992a
	165	97	8	^Murtagh, 1995
	140	95	8	Shepherd et al., 1995a
	370	92	12	Ward et al., 1995
	65 - 110	95-98	7-13	^Kita et al., 1992
	250-1150	96-100	10-12	This dissertation, 1997
	78	96	7	Johnston-Broadfoot Model, 1992
OH (6,2)	2500 - 6500	85-87	10-12	This dissertation, 1997
	750	89	10	Johnston-Broadfoot Model, 1992

Table 3.3. Comparison of measured and modeled airglow parameters.

UARS researchers (Burrage et al., 1994) have indicated that they detected tidal signatures in their data averaged over periods of weeks and months. However, they reported a persistent region of maximum emission between 10° N and 10° S that ran from sunset to 23 LST, and a region of

minimum emission beginning just after midnight. This is just west of the observation track shown in Figure 3.8. Our data set is consistent with this observation of Burrage et al., since the evening tidal enhancement they describe could not have been detected by GLO. However, Burrage et al. also detected a short term enhancement at the equator that persisted for a few days. GLO did not observe any such long-lived region of organized emission activity, at the equator or elsewhere.

Retrieved altitudes of peak emission are consistent with output from the Johnston-Broadfoot model and previous measurements. The Johnston-Broadfoot model depends on an Air Force high altitude winter atmospheric model that may not be well suited for low to midlatitudes where the STS-69 data set was recorded. From the results of Table 3.3, the Johnston-Broadfoot model appears to be systematically underestimating reactant concentrations. The differences between model predictions and GLO observations indicate that modeled reactant concentrations are low by about a factor of 5. From GLO data, O_2 Atmospheric emissions were seen to peak at around 90 km, OH Meinel at around 85 km, and OI (5577 Å) at around 95 km, although

these altitudes were variable. Fluctuations in these altitudes were noted in Figures 3.20 through 3.24 in section 3.4.

Swenson et al. (1989) observed nightly altitude shifts of about 8 km in the 5577 Å and O_2 night airglow layers using the Atmospheric Emissions Photometric Imager (AEPI) on STS-9. AEPI observations were consistent with earlier findings by Wasser and Donahue (1979) based on OGO 6 data. Similar variations have been confirmed by WINDII and now by GLO, with variations of 7 to 10 km observed on orbits 85 through 87.

Shepherd et al. (1993) have observed emission in 5577 Å to vary by factors of 4 or more, with similar patterns exhibited by OH emissions. Ward et al. (1995) observed the 5577 Å emission to vary by a factor of 10 and the O_2 (0,0) emission by a factor of 5. These findings are in good agreement with GLO data that indicate enhancement factors between 3 and 12, in general, for all emissions. They are also in accord with the Johnston-Broadfoot model.

Ward et al. (1995) have inferred from their WINDII observations that emissions in OI (5577 Å) and the O_2 Atmospheric (0,0) band are highly correlated. GLO observations suggest that the two emissions, when averaged over time scales of days, do indeed show similar trends in enhancement. However, on time scales of hours or minutes, these emissions are not coincident in space and time, and they are neither simply correlated nor anticorrelated. Chemistry considerations and output from the Johnston-Broadfoot model imply that the dynamic interaction of upwelling from below and subsiding atomic oxygen from aloft probably drives these brightness changes in a complex fashion. Upwellings may be connected to upwardly propagating gravity waves. The associated increase in eddy viscosity with such propagating gravity waves would tend to increase OH and O_2 (0,0) emissions while leaving those of 5577 Å unchanged. The downward flow of atomic oxygen in the MTI region is only now being parameterized in general circulation models at the National Center for Atmospheric Research (NCAR) and is not yet well understood.

Roble and Shepherd (1997) describe one NCAR general circulation model in which strong upwardly propagating tides disrupt the 5577 Å airglow layer near 95 km and reduce its emission rate. This same upwelling would increase O_2 (0,0) brightness and bring its peak emission rate to a lower altitude. Such effects are consistent with GLO observations. Roble and Shepherd also describe a weaker tide which does not penetrate high enough to quench the 5577 Å airglow layer, and this may be more consistent with the correlation assumption of Ward et al. (1995) based on their WINDII observations. If strong tides are presumed to be intermittent and of brief duration, averaging over long time scales as practiced by UARS researchers may reduce their signatures in airglow emission data.

Shepherd et al. (1993) reported evidence for planetary wave influence on 5577 Å emissions from analysis of data recorded by WINDII on UARS in January 1992. They detected possible diurnal and semidiurnal wave patterns in these emissions in the narrow latitude band of 40° to 42° N. Their conclusions based on this restricted coverage for a single emitting species do not agree with the phenomena observed by GLO on a global scale during the

mission of STS-69. Shepherd et al. also used the WINDII experiment to infer the effect of atmospheric tides on 5577 Å emission in the equatorial region. They observed that 5577 Å brightness in the night airglow layer near 100 km decreased by a factor of 2.7 in a 6 hour period from local dusk to midnight. GLO typically observed variations for 5577 Å much greater than this, and on orbit 86 recorded an increase by a factor of nearly 12 in a one-hour period. Shepherd et al. inferred from the UARS data that the 5577 Å decrease by a factor of 2.7 could caused by a decrease in [M] by a factor of 1.7, combined with a decrease in [O] by a factor of 1.3. They reported a subsequent gradual brightening at 5577 Å toward morning twilight, ascribing this to subsidence of atomic oxygen-rich air from above after local midnight, as predicted by the NCAR Thermosphere/Ionosphere General Circulation Model (TIGCM) of Roble (Roble and Shepherd, 1997). The brightening of the 5577 Å emission in response to the subsidence of [O] is consistent with the GLO observations summarized in Table 3.1, as discussed previously.

4. CONCLUSIONS

GLO recorded midlatitude night airglow data near equinox during Space Shuttle mission STS-69. GLO observations from the shuttle provided a record of the night airglow layer seen edge on at the Earth's limb. These top side observations show a fundamentally different picture of the night airglow compared to observations from the ground. They complement and extend the phenomenology generated by other global observations from orbit. GLO observations also represent the first simultaneous optical measurements of airglow emissions over the spectral range from 1150 to 9000 Å, showing global emission variations in the night sky. When primary emissions are all measured simultaneously, intensity variations are shown to be uncorrelated among emitting species, implying greater dynamism and more complex chemical interactions in the airglow than previously assumed.

Although other researchers describe observations of organized waves and tides in the night airglow, those observations are averaged over long time periods. The night sky intensity variations recorded by GLO do not exhibit

any obvious relationship to atmospheric tides. They may instead be associated with the chaotic superposition of upward and downward vertical motions.

Intensity variations in the night airglow layer are likely to be driven by upwelling and subsidence. These vertical motions may cause the decoupling of emissions in the O_2 Atmospheric band, the OH Meinel band, and the atomic oxygen green line at 5577 Å in the night airglow. Emission enhancements with maxima-to-minima ratios of 4 to 12, depending on emitting species, have been observed. Inferred horizontal extent of observed emission enhancement regions is on the order of 3000 km. Emissions in the O_2 Atmospheric band system and the OI (5577 Å) green line show a greater dynamic range of variation than the OH Meinel band system.

Brightening in the O_2 and OH bands and dimming of the OI (5577 Å) emission may coincide with the lowering of the altitude of peak emission. This signature is consistent with upwelling from below. The upwelling increases the concentration of reactants for the production of O_2^* and OH^*,

while quenching O*, and brings peak production of all three emitters to lower altitudes. Brightening of 5577 Å (and occasionally in O_2 and OH emissions) occurs with the subsidence of air from above, enriched with O (compared to other species). Lifting of peak emission altitudes may be associated with this subsidence.

The chemistry along a limited line-of-sight can be explained by classical airglow chemistry as modeled by Johnston and Broadfoot, but only over a limited altitude range. Dynamic effects in the 80 to 100 km MTI region are sufficiently chaotic to present mixed results when inferring chemical processes as a function of altitude.

The GLO instrument is an invaluable resource for investigation of the mesosphere-thermosphere-ionosphere (MTI) region. The ability to record atmospheric phenomena simultaneously over a wide spectral range on a global scale is critical to the advancement of our knowledge of the night airglow. GLO can therefore make a significant contribution to ongoing CEDAR campaigns designed to study the middle atmosphere.

APPENDIX A: DESCRIPTION OF THE GLO INSTRUMENT

The Arizona Airglow Instrument, or GLO, is designed to study auroral and airglow emissions. From the Shuttle, GLO can measure spatial, temporal, and spectral emission signatures at wavelengths from 1150 to 11000 Å, typically for altitudes ranging from about 80 to 350 km. The following description refers to a nominal configuration; this may be (and has been) altered depending upon the needs of a particular mission. GLO consists of nine spectrographs and twelve imagers with coaligned optical axes, incorporating both unintensified ("bare") charge-coupled devices (CCDs) and intensified charge-coupled devices (ICCDs). As a result of optimal design to minimize weight and volume, the spectrographs share four image intensifiers while the imagers share three intensifiers (Broadfoot and Sandel, 1992).

The CCDs used in the GLO instrument are 384 by 576 pixel two-dimensional arrays. Each CCD is divided into two equal sections measuring 192 by 576 pixels. Each pixel is a 0.022 mm square and the overall sensitive area of the CCD is 12.7 by 8.4 mm. Spectral dispersion along the length of

the CCD uses all 576 pixels, but the height of a single spectrum only requires 8 pixels of the CCD. Thus two sets of 24 spectra each can be focused side by side onto a single detector, retaining spectral resolution while using only 192 pixels per set of 24 (8 pixels per spectrum × 24 spectra = 192 pixels). This reduces the size of the spectrographs and uses the CCDs more efficiently. The detectors operate effectively only below 0° C. This is not a problem for the typical mission on orbit, but a cooling system can be applied if mission requirements or ground laboratory tests require it. Active cooling can be accomplished by thermoelectric or circulating refrigerant techniques, while passive cooling with radiators is also possible.

The seven intensifiers used in GLO each consist of a photocathode to detect incoming photons and a phosphor screen to generate the image. Between these components, a series of microchannel plate electron multipliers amplify the signal to produce a brighter image on the phosphor screen. The voltage across these microchannel plates determines the gain of the intensifier. A single photon entering the intensifier and hitting the photocathode can cause 10^4 photons in the 5000 to 7000 Å wavelength region

to be emitted from the phosphor screen. Exposure is controlled by setting the voltage between the photocathode and the nearest microchannel plate. When the potential of the photocathode is +40V with respect to the front microchannel plate, no electrons are emitted by the cathode. With the cathode at -200V, photoelectrons are accelerated and collide with the front microchannel plate, initiating the electron multiplication cascade. Each photon interaction, or photoevent, is spatially indexed by the microchannel plates and the fiberoptics coupler to the associated CCD. Since the spectral response of an intensifier depends on the material of the photocathode, three types of photocathodes are used to fix the sensitivity of the intensifiers to specific spectral regions of interest (Broadfoot and Sandel, 1992).

Image intensifiers make each pixel of an ICCD function as a photon counting device that preserves the Poisson (discrete) statistics of arriving photons. The dynamic range of an ICCD is not limited by the number of free electrons per pixel in the detector (the "full-well capacity"), but rather by the dark count rate and available digital memory. The dark count rate for the ICCDs used in GLO is quite small, at about 10^{-5} events per pixel per second.

At maximum gain, the image intensifier generates about 500 electrons per pixel per photoevent. A typical full-well capacity of about 2.5×10^5 free electrons implies a dynamic range limit of about 500 photoevents per pixel. However, ICCD counts can be read out frequently and quickly accumulated in memory. Integrating the signal in this way involves a modest statistical penalty factor of $2^{\frac{1}{2}}$ in going from pulse counting to pulse integration, but the dynamic range can be dramatically extended to as high as 10^7 photoevents per pixel, with a detection threshold of about 10^{-3} photoevents per pixel per second. Compare this with a dynamic range of about 10^4 photoevents per pixel and a detection threshold of about 50 photoevents per pixel per second for a bare CCD! The photocathode of an ICCD can also be chosen to eliminate sensitivity to unwanted wavelengths, an additional advantage over the bare CCD, which can yield spurious signals after being contaminated by photons outside the wavelength region of interest (Broadfoot and Sandel, 1992).

Complete spectral coverage from the UV to the near-IR eliminates the ambiguities of partial spectral coverage, and recording the entire spectrum

simultaneously allows the measurement of temporal variations. Resolution at the shortest wavelengths is 4 Å, while resolution is 10 Å at the longest wavelengths. Eight of the nine spectrographs use ICCD's, with the ninth using a bare CCD. The twelve imagers, fitted with interference filters, have varying fields of view and spectral sensitivities in order to measure the spatial extent of brightness variations over several orders of magnitude.

The brightness of the target image on the detector depends only on the f-ratio of the optics. The instrument's CCD focal plane detectors are very small, permitting much shorter optical path lengths than other technologies while maintaining the desired f-ratios and sensitivities. GLO uses concave holographic gratings that correct spherical and chromatic aberrations, as well as replace the collimating lens, plane grating, and refocusing lens needed in a conventional spectrograph. These factors combine to reduce the size and weight of the instrument. The sensor head includes all optics, the CCDs and ICCDs, and some of the electronics for GLO; it measures about 40 by 40 by 30 cm and weighs less than 35 kg.

The nine nearly identical spectrographs can each observe a long thin swath of the target region. Eight spectrographs are grouped in four pairs (pair #1 includes two UV, pair #2 includes one visible and one near-UV, pair #3 includes two visible, and pair #4 includes one visible and one near-IR spectrograph). Each pair shares a slit, foreoptics, and an optical bench mounting surface. The foreoptics for the near-IR, near-UV, and visible light optical benches consist of a cover with light baffles, two cylindrical focusing lenses, a spectral cutoff filter to eliminate higher order spectra, and two path-folding prisms. The UV foreoptics are similar, but utilize cylindrical mirrors instead of lenses to maintain focus. Each slit has dimensions 0.045 by 4.5 mm. This arrangement gives side by side image sets at the CCD, with each slit image set measuring 2 pixels wide and 192 pixels long. (Recall that each line of a spectrum is an image of the slit). The 192 pixels are divided into 24 segments of 8 pixels, and a separate spectrum is recorded in each segment. The ninth spectrograph, operating in the IR, has its own slit, foreoptics, and optical bench. The IR spectrograph foreoptics include a negative focal length lens, and this optical bench has a slit with dimensions 0.045 by 8 mm. For all nine spectrographs, the distances between the gratings and the slits are the

same, and the fields-of-view (FOV) determined by the foreoptics are about 8.5° along the slit and 0.15° perpendicular to the slit. Each grating was designed for a specific spectrograph to give dispersion and spectral coverage to match the size of the detector (Viereck et al., 1990).

On the horizon, at typical ranges of about 1500 km from a Shuttle orbiting at about 340 km, the field-of-view of a spectrograph encompasses about a 260 by 4 km swath of the atmosphere. With the slit tangent to the limb, a 4 km depth of atmosphere is thus observed by the instrument. If the slit is tilted at an angle to the limb, a deeper scan of the atmosphere is possible. For example, at an angle of 10° to the horizontal, a 45 km depth of the atmosphere is sampled, while at 90°, a maximum altitude range of about 260 km can be imaged on the slit. Since the slit image is divided into 24 segments, spectra from 24 contiguous atmospheric layers, each of about 11 km depth, may be obtained simultaneously in the latter case.

Each imager system consists of lenses to focus the source onto an image intensifier, an interference filter to limit spectral response, an imager

intensifier to increase sensitivity, and a CCD to collect the images and transform them into electronic signals. (Note, however, that image intensifiers are not used for the infrared imagers). The spectrographs and imagers both use flexible fiberoptic cable bundles, or "image conduits", to carry images from the intensifiers to the CCDs. Each fiberoptic cable consists of many strands of 0.004 mm diameter, giving a total cross section of 2.8 by 3.2 mm, defining the size of an image. There are about 20 strands per pixel, and in the imager systems, they form cables that are 60 cm long. At the face of a CCD, six fiberoptic cables form a single bundle with dimensions 8.4 by 6.4 mm, which covers half of the CCD. The image conduit bundle allows six images to be collected by one CCD. In the spectrographs, however, the fiberoptic cables are formed into short rigid blocks, connecting each intensifier to a single CCD and transferring the phosphor image directly to the CCD.

The twelve imagers include four narrow field-of-view ultraviolet (NUV) imagers (FOV 1.8° azimuth × 1.6° elevation), four wide field-of-view ultraviolet (WUV) imagers (FOV 25° az × 21° el), two medium field-of-view visible (VIS) imagers (FOV 6.0° az × 5.3° el), one wide field-of-view

infrared (WIR) imager (FOV 21° az × 19° el), and one narrow field-of-view infrared (NIR) imager (FOV 2.3° az × 2.0° el).

The eight UV imagers have narrower bandpass filters than the four non-UV imagers in order to provide spectral isolation and two-dimensional spatial information for selected UV emission features. The NUV imagers must use focusing mirrors with relatively long focal lengths, requiring larger diameters than desired to maintain an adequate f-ratio. The large diameter conflicts with the design requirement to keep the four optical axes close enough to use a single intensifier. This problem is overcome by cutting a single mirror into equal quarters which are then slightly separated to provide four distinct optical axes. A commercially available Cassegrain mirror system with a UV coating was used for this purpose. Primary and secondary mirrors were radially cut into four pieces and remounted with 9 mm gaps between their straight edges. The resulting optical axes are thus mutually separated by 9 mm, yielding four images on a single intensifier, as desired. The original Cassegrain system with an f-ratio of 1.1 and a single large aperture thus becomes a system with an f-ratio of 2.2 and four smaller apertures. The four

WUV imagers use hemispherical lenses and flat spacers made of magnesium fluoride (MgF_2) with 3.5 mm diameter apertures and f-ratios of nearly 2. They also share a single intensifier. The NUV and WUV imagers use interference filters with spectral bandpasses centered at 1600, 2000, 2350, and 2600 Å, each with a 250 Å spectral half-width (Viereck et al., 1990).

The VIS, WIR, and NIR imagers obtain pointing and target brightness information. The two VIS imagers share an image intensifier. With their approximate 5° fields-of-view, they collect broad-spectrum data from extended sources and star fields for post-flight pointing analysis. Each has a 9 mm diameter lens with a 35 mm focal length, yielding a 3.8 f-ratio. They are identical except for their interference filters: one filter has a bandpass centered on 5500 Å while the other is centered on 7000 Å, and both filters have spectral half widths of 2000 Å. The WIR and NIR imagers are not intensified and are therefore much less sensitive than the other imagers; they can observe extremely bright sources without suffering damage to their detectors. Images are formed directly on the ends of the fiberoptic cables for these much simpler IR imagers. The WIR imager, with an approximately 20°

field-of-view, monitors target brightness, while the NIR imager, with an approximately 2° field-of-view, provides fine-pointing information.

APPENDIX B: CALIBRATION OF THE GLO INSTRUMENT

Calibration of GLO occurs before, during, and after the mission. Pre- and post-flight calibration consists of measuring the coalignment, fields-of-view, and sensitivity as a function of wavelength of both the imagers and the spectrographs. Wavelength calibration and spectral line shape (instrument function) determinations are also accomplished. Faulty ("hot") pixels and average background signal for specific CCDs are identified and their effects subtracted during post-flight data calibration. Observing stars of known brightnesses in specific spectral regions provides in-flight and post-flight calibration and the best check of instrumental pointing precision and spectral response.

Laboratory intensity calibrations are referenced to a calibrated photodiode traceable to the National Institute of Standards and Technology (NIST) in Boulder, Colorado. The spectral luminosity B_λ of a light source is determined using this photodiode, a series of bandpass filters, and optical elements. Convolution of the photodiode response with the filter transmission

function gives the spectral luminosity at the center wavelength of the filter bandpass: one filter yields a single value for luminosity at a single wavelength. (The spectral luminosity is assumed constant over the bandpass range, typically less than a few hundred angstroms). By choosing many narrow overlapping bandpass filters, a spectral luminosity curve for the light source, measured in rayleighs per angstrom, can be constructed over any wavelength range of interest. Recall that one rayleigh (1R) equals 10^6 photons $sec^{-1} cm^{-2}$.

The response of an optical detector is given by the photometric equation:

$$P \text{ (in photoevents sec}^{-1}) = B_\lambda \, A_d \, \Omega \, T \, \varepsilon,$$

where B_λ = source luminosity in photons $sec^{-1} cm^{-2}$ steradian^{-1} at wavelength λ, A_d = detector area in cm^2, Ω = solid angle of the source subtended at the detector in steradians, T = optical transmission efficiency (a dimensionless ratio of the number of photons transmitted through the detector divided by the number of photons incident on the detector), and ε = detector quantum efficiency in photoevents photon^{-1}. A photoevent registered by the detector

results in an electronic signal which can be quantified by an analog-to-digital converter (ADC). The ADC produces one digital Data Number (DN) for a specific input signal from the detector. The response P can be converted to digital response R by the formula R (in DN/sec) = P (in photoevents/sec) $\times$ S, where the conversion factor S depends on the type of detector. For an unintensified CCD, S_{ccd} is approximately 0.02, where approximately fifty photoelectrons yield a signal of one DN, while for an intensified CCD, S_{iccd} is approximately 2.0, where two DN are typically registered at maximum gain for each photoevent.

The solid angle Ω of an imaging system can be written in terms of the f-ratio of the optics, where f-ratio = focal length divided by aperture: $\Omega = \pi/4 \times (\text{f-ratio})^{-2}$. Using this definition of Ω, the fact that detector pixels each measure 22 mm $\times$ 22 mm, and that the normalized spectral luminosity equals imager bandpass in angstroms times 1 R/Å, we obtain, for a source of brightness N (R/Å), a normalized digital response per pixel given by the formula:

$$R \text{ (DN/pixel)} = R_{\text{normalized}} \text{ (DN/sec)} \times N \times \text{exposure (sec)}.$$

Calibration for wavelengths longer than 4000 Å is reproducible to within ±20%, implying an overall precision of about 80% for the GLO spectrographs. This level of precision is representative of modern optical instrumentation standards. No degradation of response has been detected as a result of detector exposure to the space environment.

APPENDIX C: LIMB TRACKING VALIDATION

The GLO limb tracker follows the brightest region of a strip through the imager FOV by moving the scan platform in AZ and EL, thereby removing the shuttle limit cycle motion. Post-flight, the airglow layer height is calculated by combining the AZ/EL coordinates (corrected to shuttle coordinates) of the GLO scan platform and the shuttle attitude (given by the pitch, roll, and yaw axes).

Position data is available describing both the shuttle attitude and GLO scan platform tracking motion. A data analysis software package known as SYBIL, developed by Kalynnda Berens at LPL West, allows the automatic adjustment and interpolation of this position data to automatically extract spectrograph and imager photometric data at constant altitudes. In this section, that process is validated.

GLO limb tracking capability was used throughout this data set. GLO pointing control adjusted the elevation and azimuth of the GLO boresight in

order to track the airglow layer. Shuttle pitch information and actual GLO pointing direction were combined, then the result used to calculate the LOS elevation angle (LOS θ, measured up from nadir). LOS θ leads to the tangent point altitude and range by simple right triangle relations. The calculated tangent point altitude is thus a result of known shuttle pitch variations and unknown vertical motion of the airglow layer.

Our problem is to separate the two effects, removing the influence of shuttle pitch changes to discover the true change in altitude of the airglow layer.

If there is no timing error between the GLO clock and the orbiter clock, then the tangent point height calculation is assumed to be accurate. We can calculate the GLO AZ/EL coordinates for a constant tangent point altitude by using the shuttle attitude record provided by NASA. The difference between these AZ/EL coordinates and actual AZ/EL coordinates recorded while tracking would give the variation in the altitude of the airglow layer. Consequently, GLO data could be adjusted to true altitude.

In Chapter 2, the systematic error due to the discrepancy between the GLO clock and the orbiter clock was described. The correction to the tangent point altitude is calculated by SIBYL. This calculation uses plane geometry and does not take into account the effect of small angles near the pole of GLO scan platform azimuth axis. Unfortunately, the night sky observation geometry for STS-69 required data to be collected near the GLO azimuth pole. This problem has been referred back to the LPL West GLO science team. For the purposes of this work, the airglow layer altitude has been corrected to the sodium layer at 90 km, assumed to be a stable reference.

Figures 2.7 and 2.8 showed that the maximum excursion in shuttle pitch was typically 1.3° during a night pass. This caused the LOS to sweep through a 45 km range of altitude at the Earth's limb at a range of 2000 km. This would have severely compromised observation time on the limb if tracking had not been used. Although GLO scan platform pointing accuracy is known, this pointing must be calibrated in terms of the shuttle coordinate system to achieve optimum tracking.

In order to correct the airglow observational altitude to the absolute tangent point altitude, the scan platform was calibrated with respect to the shuttle coordinate system as described previously. The recorded scan platform motion in AZ and EL must now also be reconciled against the limit cycle motion of the shuttle.

The shuttle pitch motion causes the primary change in GLO pointing. Since the slit is at an angle to the limb, both AZ and EL are affected. Tracking compensated for pitch changes by rotating AZ and EL in the opposite sense of those changes. Shuttle pitch was recorded in real time by NASA ground control at one second intervals. Thus the shuttle pitch changes ΔP (Figure C.1) are known with high temporal resolution. The imposed "sawtooth function" ripples in Figure C.1 are unresolved as yet, but are apparently the result of data truncation in the NASA recording process.

STS-69 PITCH DEADBAND FOR ORBIT 72
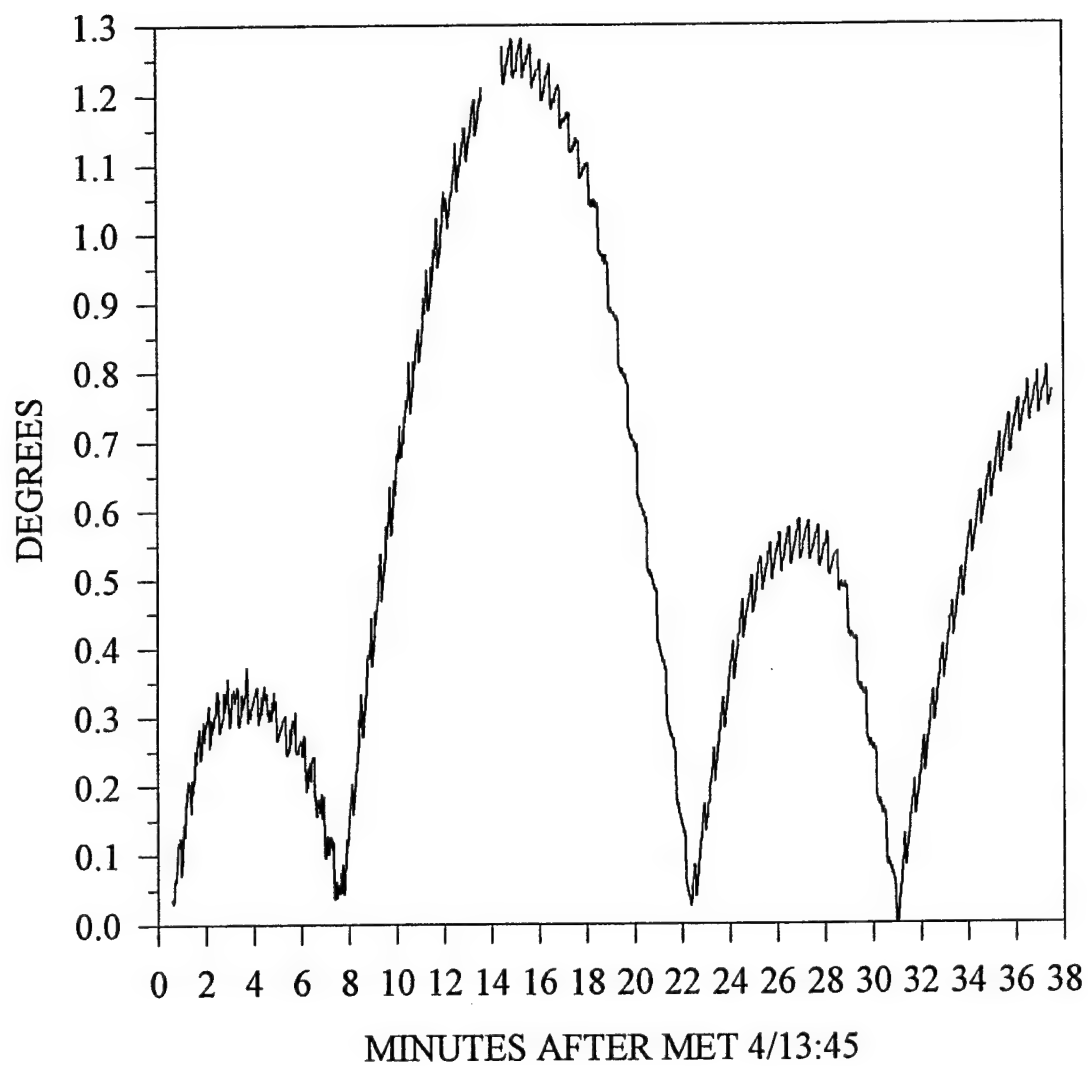
Figure C.1. STS-69 pitch deadband for orbit 72.

Attained AZ and EL positions (Figure C.2) were also updated at two second intervals in response to the error determined by the tracker telescope on GLO. Attained and commanded AZ/EL positions differed by ±0.005° because of the limits of scan platform pointing accuracy.

Spherical geometry gives the angular offset caused by AZ/EL tracking (accounting for pitch *and* airglow altitude changes) with the formula

$$\Delta P' = \cos^{-1}[\sin(EL_1)\sin(EL_2)+\cos(EL_1)\cos(EL_2)\cos(AZ_1-AZ_2)],$$

where EL_1 and EL_2 are consecutive elevation values, AZ_1 and AZ_2 are the corresponding azimuth values, and $\Delta P'$ is the compensating angular variation caused by tracking (Figure C.3). The sum of actual tracking variations $\Delta P'$ reflected in Figure C.3 and pitch variations ΔP shown in Figure C.1 should yield a small residual representing the vertical motion of the airglow layer.

STS-69 AZIMUTH AND ELEVATION FOR ORBIT 72
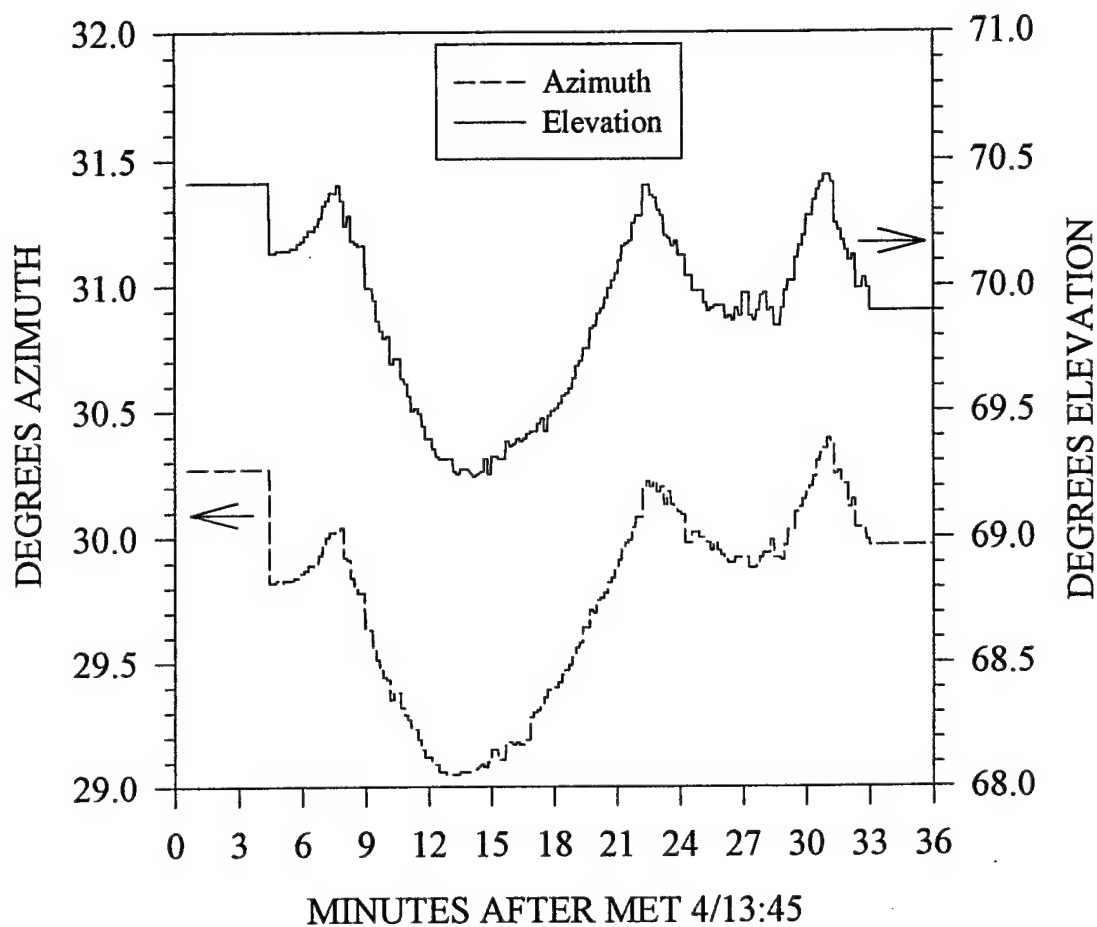
Figure C.2. STS-69 azimuth and elevation while tracking during orbit 72.
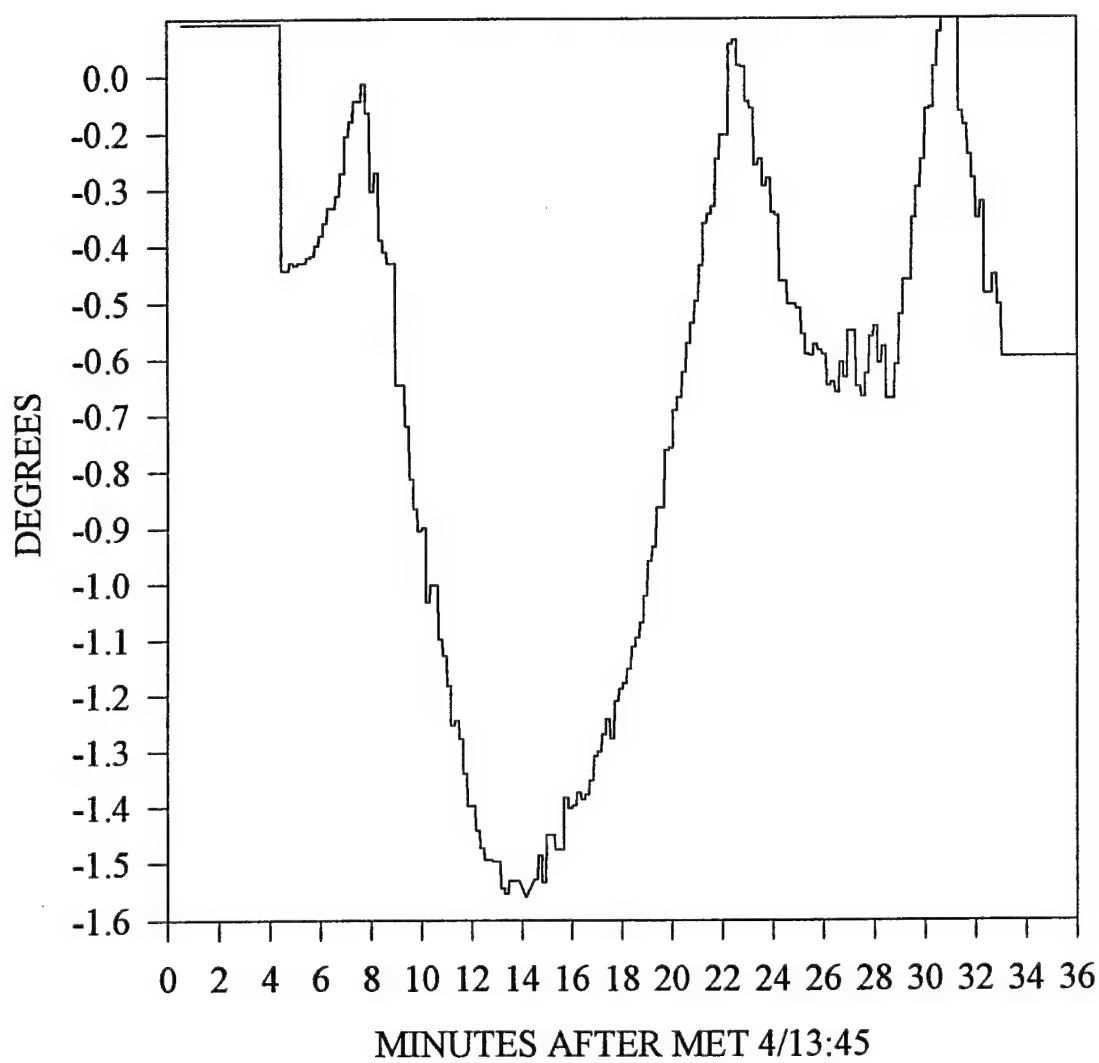
Figure C.3. GLO tracking primarily compensates for pitch changes.

Figure C.4 shows the tangent point altitude calculated from LOS θ as a function of time. Tracking begins at 4.4 minutes into the orbit and ends at 34.2 minutes. Figure C.4 should be a reflection of Figure C.3, and yet the two plots are very different. LOS θ is a secondary product derived by the LPL West science team from NASA mission data. The discrepancy between Figures C.3 and C.4 is caused by the need for spherical geometry calculations near the pole of the GLO scan platform, as described previously.

# TANGENT POINT ALTITUDE FOR ORBIT 72
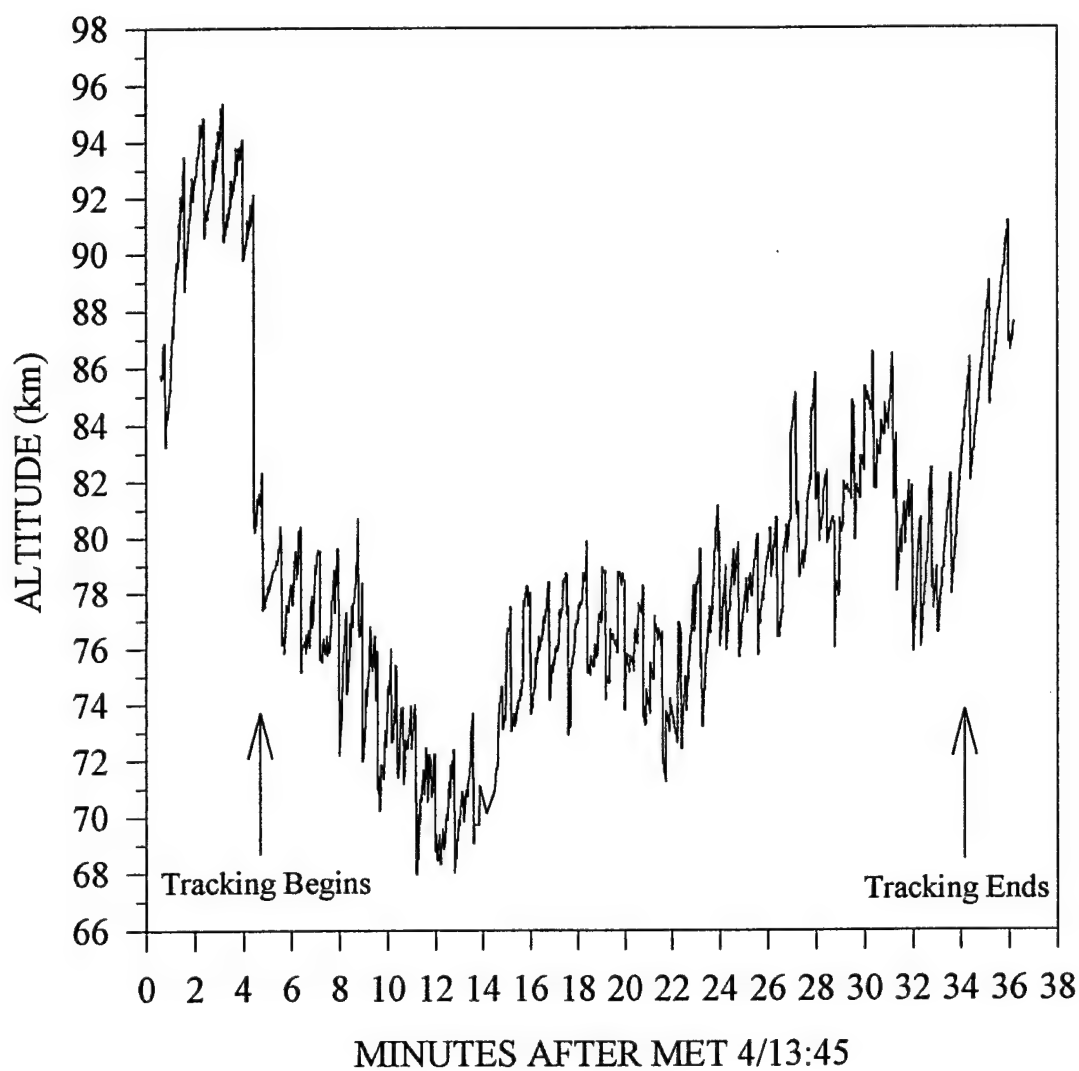
Figure C.4. Tangent point altitude as a function of time. This plot reflects a superposition of shuttle attitude drift and GLO scan platform motion.

Note that Figure C.4 exhibits the sawtooth variation described previously. The sawtooth has a period of 25 seconds and an amplitude of 0.05°. It represents an undetectable change in line-of-sight direction and is not an artifact of tracking. After subtraction of $\Delta P'$, the new plot of airglow altitude variation would still possess the sawtooth. The sawtooth is easily removed by smoothing with a running point average. Averaging over 50 seconds of data produced the best results (Figures C.5 and C.6). The smoothed plots on the next two pages were expected to represent the relative variation in altitude of the airglow layer as GLO followed limb brightness. However, they depict remnants of the shuttle limit cycle and not true airglow height variations because of the limitations of the SIBYL analysis package.

Figure C.5. Tangent point altitude minus pitch drift effects for orbit 71.

ALTITUDE INFERRED FROM THE DIFFERENCE
BETWEEN CALCULATED TANGENT HEIGHT
AND PITCH COMPENSATION DURING ORBIT 72
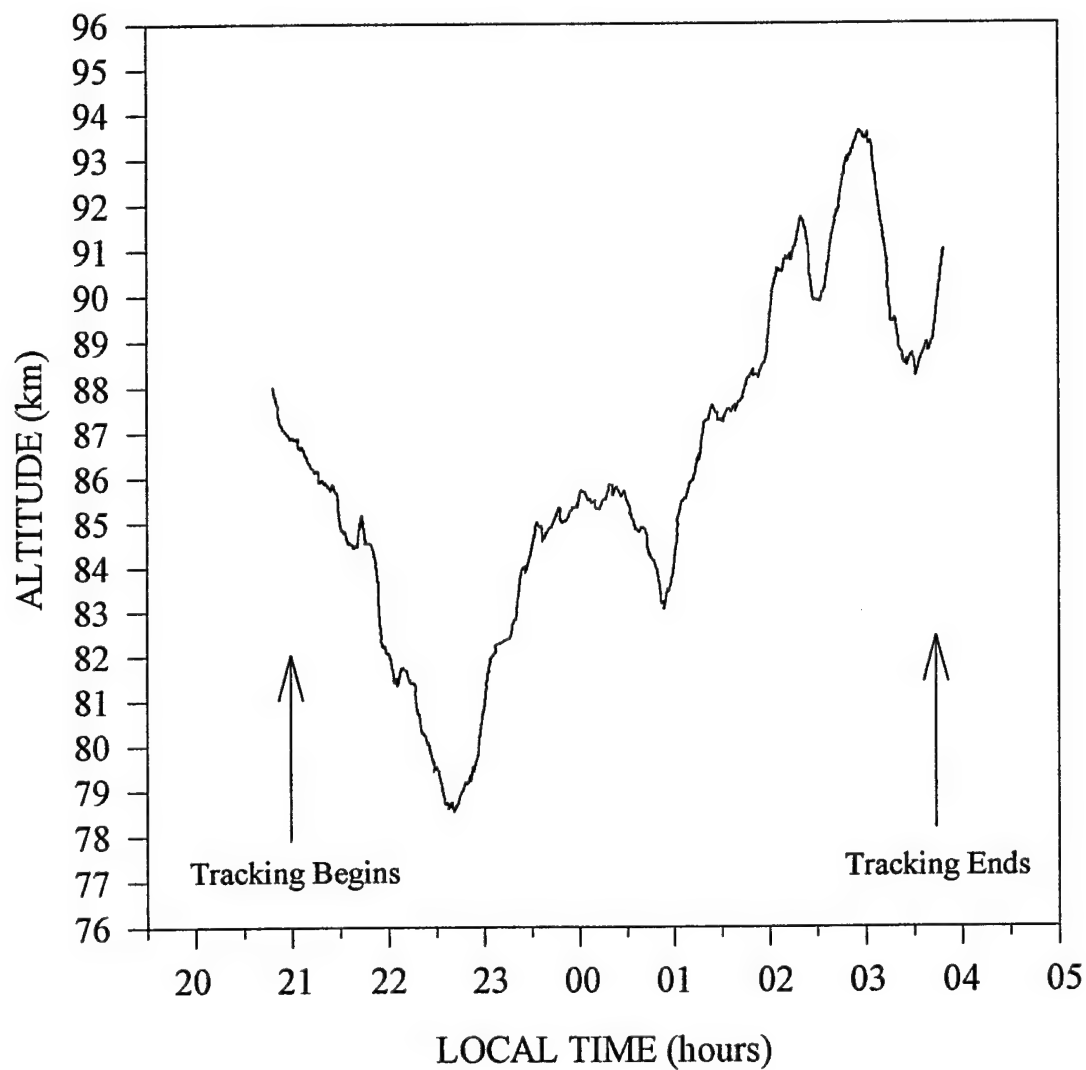
Figure C.6. Tangent point altitude minus pitch drift effects for orbit 72.

APPENDIX D: RETRIEVAL OF VOLUME EMISSION RATES FROM LOS BRIGHTNESS PROFILES

Dasch (1992) described the technique used here to infer vertical profiles of emitting species. His method is an algorithm based on the known properties of the Abel integral (Hassani, 1991). The algorithm assumes cylindrical symmetry in the plane of observation and involves an integration over observed data $P(r_j)$ to obtain values of the originating field distribution $F(r_i)$. Here, the $P(r_j)$ are the line-of-sight surface brightness intensities, integrated along the path from the tangent point to the GLO instrument, arising from the actual vertical profile of volume emission rates $F(r_i)$. The technique is appropriate here because lateral spherical curvature is negligible in our fields of view, making cylindrical geometry highly accurate.

The integral for a given $F(r_i)$ can be expressed analytically as the sum

$$F(r_i) = -\frac{1}{\Delta r} \sum_j [I_{ij}(1) - I_{ij}(0)] P(r_j - 1) - 2 I_{ij} P(r_j) + [I_{ij}(1) + I_{ij}(0)] P(r_j + 1),$$

where $I_{ij}(0)$ and $I_{ij}(1)$ are symmetry weighting factors and Δr is the distance increment between points where $F(r_i)$ is evaluated (Dasch, 1992).

The symmetry weighting factors $I_{ij}(0)$ and $I_{ij}(1)$ are defined as follows:

$I_{ij}(0) =$

$$0 \qquad \text{for } j = i = 0 \text{ or } j < i;$$

$$\frac{1}{2\pi}\ln\left\{\frac{[(2j+1)^2 - 4i^2]^{1/2} + 2j + 1}{2j}\right\} \qquad \text{for } j = i \neq 0;$$

$$\frac{1}{2\pi}\ln\left\{\frac{[(2j+1)^2 - 4i^2]^{1/2} + 2j + 1}{[(2j-1)^2 - 4i^2]^{1/2} + 2j - 1}\right\} \qquad \text{for } j > i;$$

and

$I_{ij}(1) =$

$$0 \qquad \text{for } j < I;$$

$$\frac{1}{2\pi}[(2j+1)^2 - 4i^2]^{1/2} - 2j I_{ij}(0) \qquad \text{for } j = i;$$

$$\frac{1}{2\pi}\{[(2j+1)^2 - 4i^2]^{1/2} - [(2j-1)^2 - 4i^2]^{1/2}\} - 2j\, I_{ij}(0) \qquad \text{for } j > i.$$

Dasch confirmed the cylindrical symmetry of the observation geometry is completely captured by the weighting factors. Retrieval of the original

geometry is independent of the spatial increment Δr between the observations $P(r_j)$, as long as oversampling (i.e., redundant observation) is avoided.

The geometric weighting factors I_{ij} (0) and I_{ij} (1) need only be computed once and can be applied to *any* set of observations with cylindrical symmetry. The calculated values then fill a square transformation matrix I_{ij}, whose dimension is appropriate to the number of observations performed. The observations $P(r_j)$ form a column vector; premultiplying this column matrix by the square transformation matrix I_{ij} yields the originating column vector $F(r_i)$ describing the vertical profile we seek.

The square matrix of these values acts as the operator for the Dasch algorithm, technically known as a "three-point Abel inversion." Roble and Hays (1972) described a related Abel integral technique used to process occultation data for recovering vertical density profiles of atmospheric constituents. Others have discussed similar techniques since at least the 1960s (e.g., Barr, 1962). Dasch compared several similar techniques and concluded the three-point Abel inversion suffers the least from noise and is the most

effective in deconvolving sharp data discontinuities. It is also easy to calculate using spreadsheet software, such as Lotus 123 or Quattro Pro. For these reasons, the three-point Abel inversion was adopted for this research.

Two tests were performed of this method's effectiveness. Manually, the integrated brightnesses along line-of-sight chords in concentric spherical shells were computed as altitude was decreased along a radial. These LOS values arose from a constant volume emission rate of 2000 photons cm^{-3} sec^{-1} in a 10 km thick uniform layer centered at 100 km altitude. Applying the Dasch algorithm using a Δr of 1 km to this LOS input profile provided a fairly accurate retrieval. The volume emission rate profile was a "box function," sharp-edged, discontinuous, and entirely nonphysical (Figure D.1). The LOS brightness profile resulting from this volume emission rate profile should have been very difficult for Dasch's algorithm to process, yet the method provided output very close to the original profile (Figure D.2). The output returned a skewed box-type profile, while overestimating the original value by about 20% at the bottom of the layer and 10% at the top of the layer. Based on this result, the method was deemed very effective. To test the

INTEGRATED LOS PROFILE USED AS INPUT
BY THE DASCH INVERSION, MANUALLY COMPUTED
FOR THE ORIGINAL "BOX FUNCTION" PROFILE
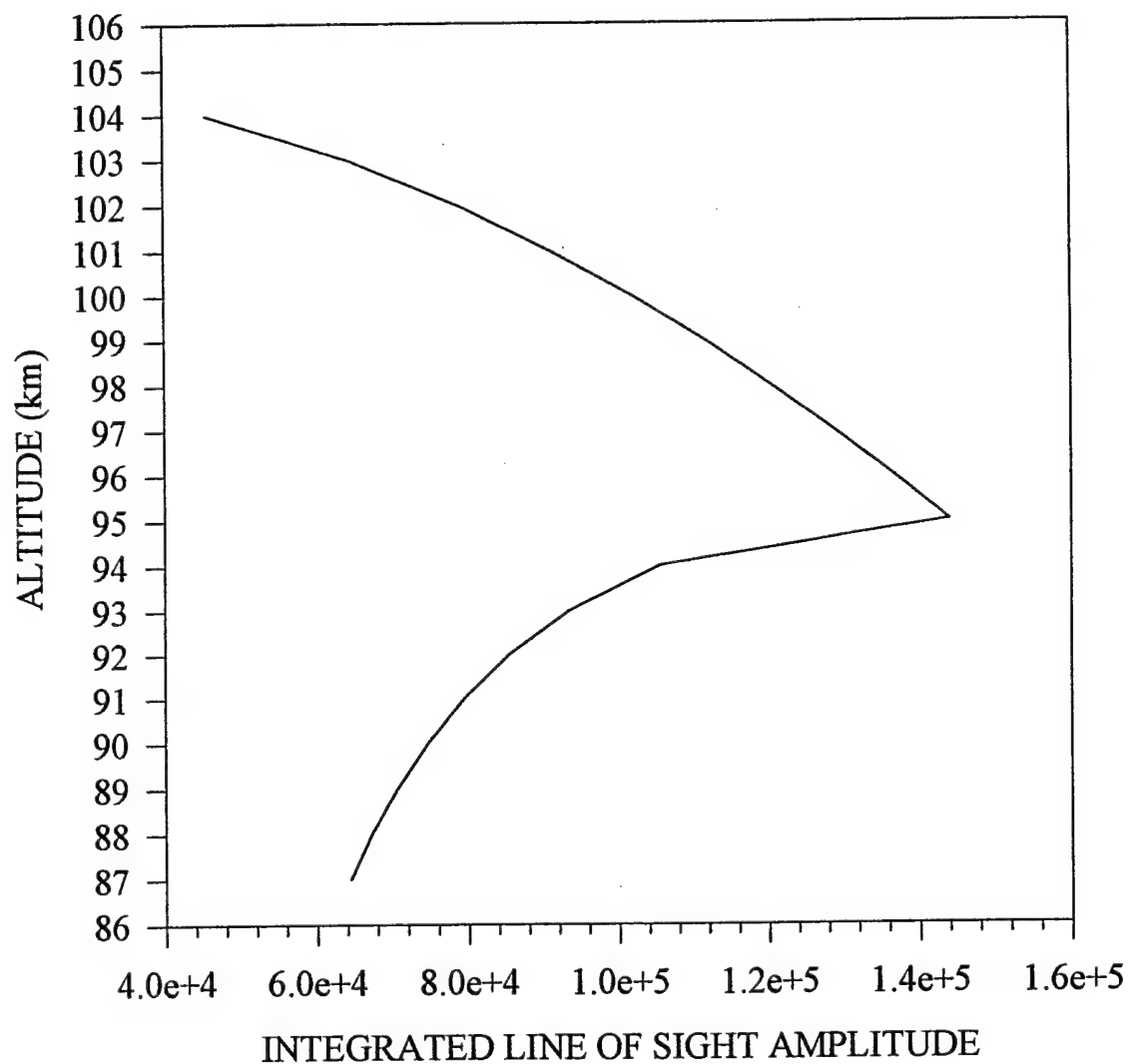
Figure D.1. The integrated line-of-sight profile for the box function computed manually and used as input to test the Dasch algorithm.

COMPARISON OF ORIGINAL "BOX FUNCTION" PROFILE
TO PROFILE RETURNED BY THE DASCH INVERSION
OPERATING ON THE INTEGRATED LOS PROFILE
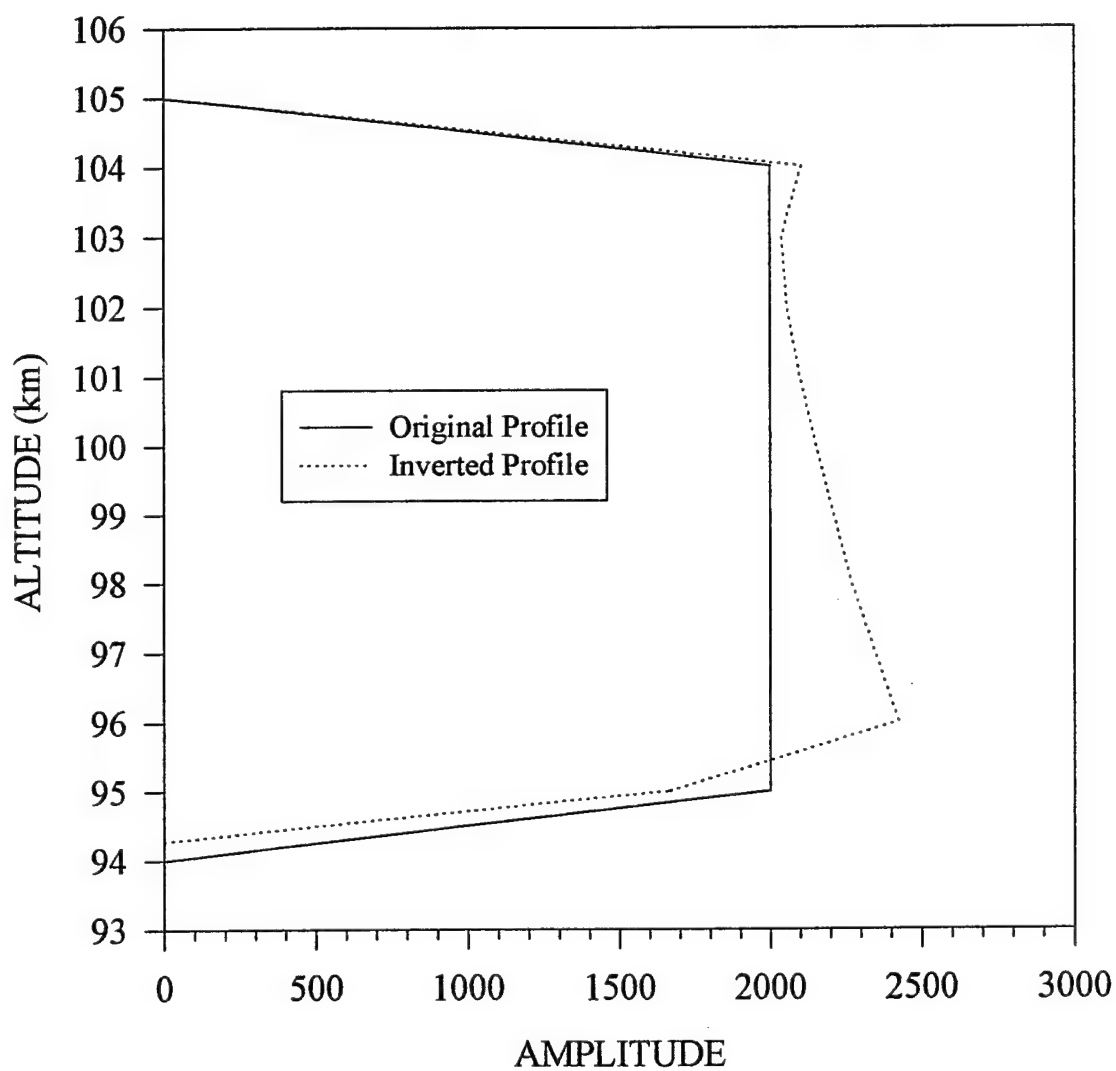
Figure D.2. Comparison of the original box function profile with the profile retrieved by the Dasch algorithm using the previous plot as input.

algorithm further, more realistic input profiles were required. These were computed using a FORTRAN program.

Dasch's method was tested on models of spherical shell layers with gaussian vertical profiles. A FORTRAN program (Appendix E) calculated the resulting vertical line-of-sight profiles associated with these layers, given a Δr of 1 km. Layers were modeled by a simple gaussian function $f(x) = c \exp[(\sigma/2) x^2]$, with layer "thickness" defined as the full width at half maximum (FWHM) and the step size for x (representing the increment Δr) taken to be one unit. Here, FWHM=2σ and values beyond $\pm 3\sigma$ were set to zero. Radial altitude of the peak was varied, and resulted in different line-of-sight path lengths through the layer by changing the curvature of the layer. The σ values were varied to change layer thickness and the gaussians were multiplied by constants c to give different peak values for the various tests. Knowing the original gaussian profile and the integrated LOS profile derived from it allowed a comparison with output from the Dasch algorithm.

INTEGRATED LOS PROFILE USED AS INPUT
BY THE DASCH INVERSION, COMPUTED IN FORTRAN
FOR THE ORIGINAL GAUSSIAN PROFILE
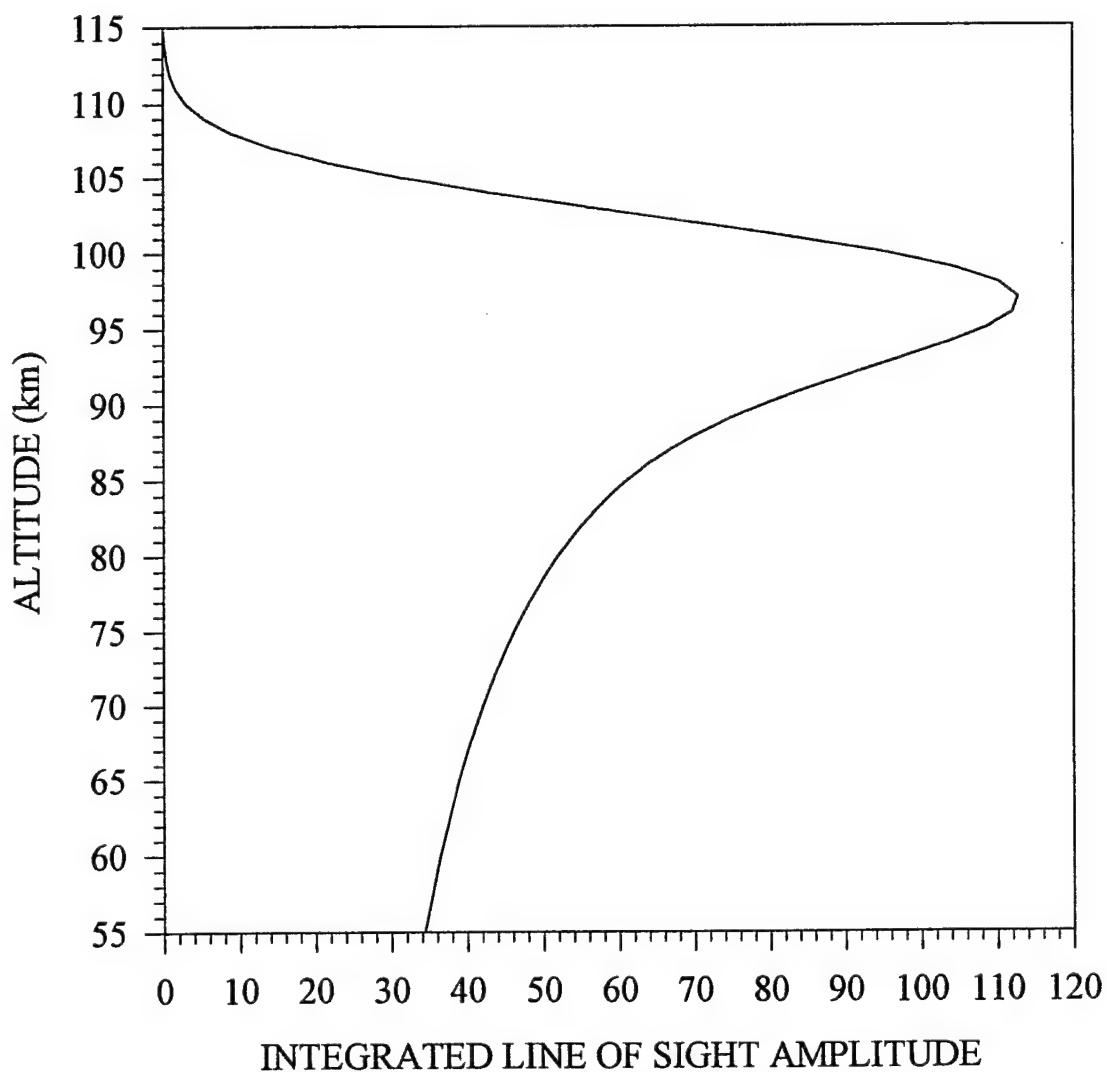
Figure D.3. The integrated line-of-sight profile computed for the gaussian profile by a FORTRAN program and used as input to test the Dasch algorithm.

COMPARISON OF ORIGINAL GAUSSIAN PROFILE TO
PROFILE RETURNED BY THE DASCH INVERSION
OPERATING ON THE INTEGRATED LOS PROFILE
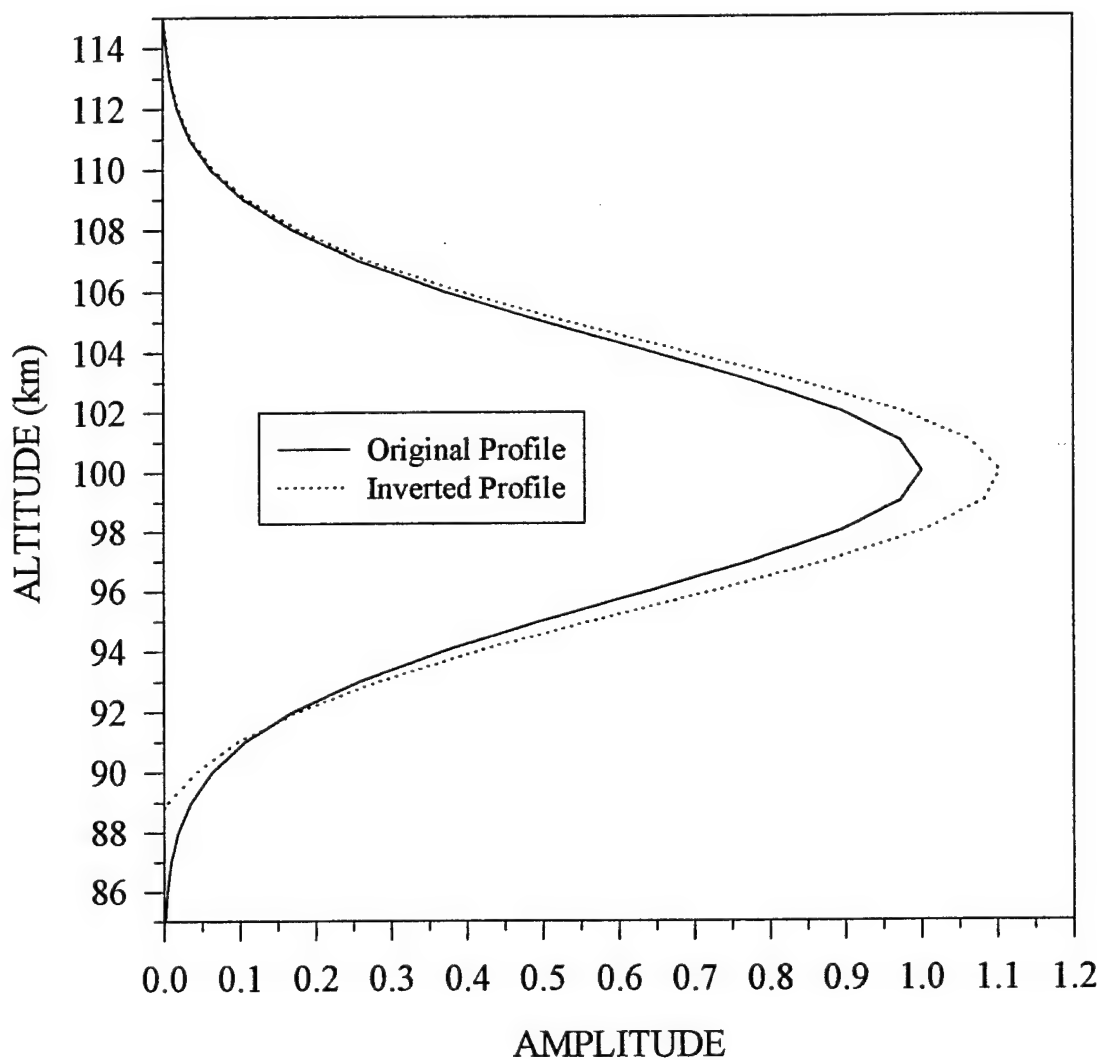
Figure D.4. Comparison of the original gaussian profile with the profile retrieved by the Dasch algorithm using the previous plot as input.

Figures D.3 and D.4 show the results of this test for a gaussian layer with $\sigma = 5$ km and $c = 1$, centered at an altitude of 100 km, and its resulting integrated line-of-sight profile. The test parameters to be retrieved were the *altitude of peak amplitude*, the *peak amplitude*, and the *layer thickness* (FWHM). Performance of the Dasch algorithm is excellent between $\pm 2.5\sigma$, while outside these limits, the method produces negative values which are ignored. The retrieval of the layer geometry is excellent: the altitude of the amplitude peak, layer thickness, and shape of the vertical gaussian profile is accurately preserved. For profile values at the peak, error is 10%. At the top of the layer ($+2.5\sigma$), amplitude error is less than 1%, while at the bottom of the layer (-2.5σ), errors are on the order of 5%, although this depends on layer thickness. Error increases with decreasing thickness, as might be expected due to resolution limits caused by a discrete step size. The Dasch algorithm appears to produce accurate estimates of volume emission rate profiles, as long as Δr is much smaller than the FWHM.

Performing tests on gaussians with the ratio $R = [\Delta r \div \text{FWHM}]$ ranging from 0.10 to 0.90, two of the key parameters proved very sensitive to R.

Retrieval of the *altitude of peak amplitude* is consistently accurate, but not that of the *peak amplitude* or *layer thickness*. The algorithm is best for small R (high resolution) and effectiveness deteriorates with increasing R.

A value of $R = 0.10$ gives retrieved amplitude peak values that are elevated by 10%, while producing minimal errors in peak altitude or thickness. With $R = 0.25$, layer thickness and peak altitude are retrieved with minimal error, but peak amplitude is increased by a factor of 3. For $R = 0.50$, retrieved layer thickness is increased by 1.25 and peak amplitude by 4.8, while for $R = 0.90$, thickness is increased by the factor 1.5 and peak amplitude by 5.8. For values of R greater than 1.0, this method is best used to determine peak altitude only. For GLO data analyzed here, Δr varies from about 6 to 8 km. If the airglow layer thickness is assumed to be about 10 km, then R is about 0.70, and the Dasch algorithm could broaden the retrieved layer thicknesses by up to 35% while increasing the peak emission by about a factor of 5. Only peak emission values presented here have been adjusted. Potential layer broadening of 3 to 5 km is within the current uncertainty in accepted values of airglow thickness and is not systematically corrected here.

APPENDIX E: THE GAUSSIAN LAYER ALGORITHM

```
*****       PROGRAM TO CALCULATE INTEGRATED        *****
*****                 LAYER EMISSIONS              *****
***** USING GAUSSIAN VERTICAL DISTRIBUTIONS        *****
*****               FOR EMITTERS                   *****
*****
*****
***** Paul Bellaire, LPL West, University of Arizona, Apr 95  *****

        DOUBLE PRECISION A(1000,100)
        DOUBLE PRECISION C(1000,100)
        DOUBLE PRECISION COR(1000,100)
        DOUBLE PRECISION TOP(100)
        DOUBLE PRECISION H(1000)
        DOUBLE PRECISION P(100)
        DOUBLE PRECISION V(100)
        DOUBLE PRECISION E(1000)
        DOUBLE PRECISION z,W,SIGMA,BOT,QMID,T,THK,PI

*****   INPUT LAYER MEAN ALTITUDE AND THICKNESS

        write (*,*) ('THIS PROGRAM ASSUMES A GAUSSIAN
                     DISTRIBUTION FOR')
        write (*,*) ('AN EMITTING SPECIES; YOU MUST KNOW THE
                     FULL-WIDTH')
        write (*,*) ('HALF MAXIMUM (FWHM) OF THE LAYER
                     DISTRIBUTION!')
        write (*,*) ('   ')
        write (*,*) ('Input layer mean altitude in km (to nearest 0.1 km AGL):')
        read (*,*) QMID
        write (*,*) ('Input layer thickness (to nearest 0.1 km; max is 100):')
        write (*,*) ('NOTE: thickness = FWHM of the emitter distribution!')
        read (*,*) THK

        QMID=QMID+6378D0
```

```
***    CALCULATE TOP 'T', BOTTOM 'BOT', AND RMS FACTOR
***    'SIGMA', NOTING  THAT OUR GAUSSIAN IS GIVEN BY:
***
***                  F(X) = EXP(-[SIGMA/2]X**2)
***              SIGMA COMES FROM THE FORMULA:
***
***       ln 0.5 = -[SIGMA/2] [X**2], WHERE FWHM = 2X = THK
***
***  NOTE: (3 X FWHM) = 'W' ACCOUNTS FOR >99.7% OF LAYER


        SIGMA=1.3863D0*(2D0/THK)**2
        T=QMID+(1.5D0*THK)
        BOT=QMID-(1.5D0*THK)
        W=3D0*THK
        PI=ACOS(-1D0)
        OPEN (55,FILE='a.out')


****    INITIALIZE ARRAYS AND START DO-LOOP FOR
****              99 1-KM DECREMENTS


        A(1,1)=T
        TOP(1)=T
        j=1

        DO 100 jd=1,99

        jj=j
        j=j+1

        TOP(j)=TOP(jj)-1D0
        A(1,j)=TOP(j)

****    DIRECT PROGRAM FLOW FOR L.O.S. PATHS
****              WITHIN OR BELOW LAYER

        IF (A(1,j).LT.BOT) THEN
```

```
          GOTO 210
          ELSE
          GOTO 50
          END IF


****   CALCULATE GAUSSIAN-WEIGHTED L.O.S. PATHS
****                 WITHIN LAYER


50    n=INT((jj)*10)
      i=1
          DO 200 id=1,n-1

          ii=i
          i=i+1
          A(i,j)=A(ii,j)+0.1D0
          C(i,j)=2D0*(DSQRT(A(i,j)**2-TOP(j)**2))

          IF (i.EQ.2) THEN
          COR(i,j)=C(i,j)
          ELSE
          COR(i,j)=C(i,j)-C(ii,j)
          END IF

****  EVALUATE EXPONENTIAL AT THE MIDPOINT
****          OF THE ALTITUDE INCREMENT

          H(i)=(((((A(i,j)+A(ii,j))/2D0)-QMID)**2)*(SIGMA/2D0)
          E(i)=DSQRT(SIGMA/(2D0*PI))*DEXP(-H(i))
          P(j)=2*COR(i,j)*E(i)+P(j)
          V(j)=DEXP(-(SIGMA/2D0)*(TOP(j)-QMID)**2D0)

          IF (i.EQ.2) THEN
          WRITE (55, 12) P(j)
12        FORMAT (1x,f16.8)
          END IF
```

```fortran
200       END DO

       GOTO 100

****  CALCULATE GAUSSIAN-WEIGHTED L.O.S. PATHS
****              BELOW LAYER

210   m=INT(W*10)
      A(1,j)=BOT
      k=1
      z=0D0

          DO 300 kd=1,m-1

          kk=k
          k=k+1
          z=z+1D0
          A(k,j)=BOT+(z*0.1D0)
          C(k,j)=2D0*(DSQRT(A(k,j)**2-TOP(j)**2))

          IF (k.EQ.2) THEN
          COR(k,j)=C(k,j)-DSQRT(BOT**2-TOP(j)**2)
          ELSE
          COR(k,j)=C(k,j)-C(kk,j)
          END IF

****  EVALUATE EXPONENTIAL AT THE MIDPOINT
****         OF THE ALTITUDE INCREMENT

          H(k)=(((((A(k,j)+A(kk,j))/2D0)-QMID)**2)*(SIGMA/2D0)
          E(k)=DSQRT(SIGMA/(2D0*PI))*DEXP(-H(k))
          P(j)=2*COR(k,j)*E(k)+P(j)

          IF (k.EQ.2) THEN
          WRITE (55, 11) P(j)
11        FORMAT (1x,f16.8)
```

```fortran
          END IF

300       END DO

100    END DO

*****              WRITE TO OUTPUT FILE              *****

       QMID=QMID-6378D0

       OPEN (5,FILE='pgauss.out')
       WRITE (5,9) QMID, THK
9      FORMAT (1x,'Layer altitude =',f8.2,4x,'Layer thickness=',f8.2)

       WRITE (5,10) P
10     FORMAT (1x,f16.8)

       OPEN (8,FILE='vgauss.out')
       WRITE (8,15) V
15     FORMAT (1x,f16.8)

       STOP
       END
```

APPENDIX F: THE JOHNSTON-BROADFOOT MODEL

Following this introduction, the reader will find the code, written in "C," of the Johnston-Broadfoot model (Johnston and Broadfoot, 1993). This program models the night atmosphere from 60 to 120 km altitude, dividing it into 30 finite plane-parallel layers, each of 2 km depth, and uses a time step of 300 seconds. Each layer is homogeneous with a constant particle number density for the major constituents O_2 and N_2, based on the assumption of negligible diurnal variation of these constituents at the altitudes in question (Rodrigo et al., 1991). Output consists of vertical number density profiles, integrated vertical column densities, and altitudes of peak emission for the lines and bands of O_2, OH, and the various species of O (Johnston, 1992).

The number densities of the minor constituents are calculated using the equation of continuity:

$$\frac{\partial N_i}{\partial t} = -\frac{\partial}{\partial z}(N_i w_i) + P(N_i) - L(N_i),$$

where the number density of the minor constituent is N_i, the chemical production and loss terms for the minor constituent are $P(N_i)$ and $L(N_i)$, respectively, t is time, z is altitude, and the term $\partial/\partial z\ (N_i\ w_i)$ represents diffusion. The upward diffusion velocity w_i of a minor constituent is given by

$$w_i = -D\left(\frac{1}{N_i}\frac{\partial N_i}{\partial z}+\frac{M_i g}{k T}+\frac{1}{T}\frac{\partial T}{\partial z}\right)-K\left(\frac{N_i}{N}\frac{\partial}{\partial z}\left[\frac{N_i}{N}\right]\right),$$

where D and K are the molecular and eddy diffusion coefficients, respectively, T is temperature, k is Boltzmann's constant, M_i is the molecular or atomic mass of the minor constituent, z is altitude, g is the acceleration of gravity, and the number densities of the major and minor constituents are N and N_i, respectively (Johnston, 1992).

The HO_x cycle reactions occur sufficiently swiftly that HO_x species concentrations are assumed to reach equilibrium "instantaneously" within each time step. The reactions of the HO_x cycle depend on the number densities of O, O_2, O_3, and N_2, but the reactions do not significantly alter the number densities of these non-HO_x reactants in one time step. The reaction

rates in the HO_x cycle can then be assumed to be proportional only to the amount of HO_x species present. Given the concentrations of HO_x, O, O_2, O_3, and N_2, the equilibrium concentrations of H, OH, and HO_2 are calculated. Below an altitude of 86 km, atomic oxygen in the $O(^3P)$ state is lost during the production of ozone. This loss is approximated by a negative exponential function describing O concentrations during each time step. Eleven reactions for production of O_2, O_3, and OH and twenty-one reactions involving quenching or radiative losses for excited states of O, O_2, and OH are included in the model (Johnston and Broadfoot, 1993).

The standard input profiles for constituent number densities used by the model are based on the 1976 US Standard Atmosphere and the Air Force Geophysics Laboratory's 1985 atmospheric model (see Appendix G for the numerical data in tabular form). Below 90 km, this input profile is representative of middle latitudes, while above 90 km, it is more typical of averaged winter conditions. Thus, we expect this input profile to be more of a general guide than a precise model for low latitude equinox conditions. Reactant concentrations in the actual atmosphere will be different, but are

assumed to follow the altitude dependencies and vertical structure indicated by the Johnston-Broadfoot model output.

Figures F.1 through F.3 provide volume emission rate and brightness profiles for the airglow emissions of interest in this research, namely, the O_2 Atmospheric band, the oxygen line at 5577 Å, and the OH Meinel band. These profiles were derived from the output profiles for excited state emitter number densities produced by the Johnston-Broadfoot model, shown in Figure F.1. Figure F.2 indicates the related volume emission rate profiles, while Figure F.3 shows the resulting line-of-sight (LOS) integrated brightness profiles as seen from the topside (neglecting the optical depth of O_2 (0,0) band). Figure F.3 was developed from output of the Dasch algorithm described in Appendix D. Known transition probabilities were used to compute the volume emission rates and brightnesses in Rayleighs from the output number densities. The probabilities for the O_2 (0,0) and (0,1) bands (0.0793 sec^{-1} and 0.00391 sec^{-1}, respectively) were obtained from Vallance Jones (1974). Turnbull and Lowe (1989) provided the thermally averaged probability of 3.48 sec^{-1} for the OH Meinel (6,2) band at 200 K. The

transition probability of 1.34 sec^{-1} used for the OI (5577 Å) line was given by Tohmatsu (1990).

Note that the profiles of emitter concentrations and volume emission rates can be closely approximated by gaussians. The Johnston-Broadfoot model predicts full widths at half maximum (FWHM) for O_2 Atmospheric and OH Meinel emissions to be about 10 km, while for the 5577 Å line, it predicts a FWHM of about 7 km. The model predicts the altitude of peak emission at approximately 94 km for the O_2 Atmospheric band, at 96 km for the atomic oxygen 5577 Å line, and at about 89 km for the OH Meinel band (see Table 3.3 for a comparison of the model with actual observations).

CONCENTRATION PROFILES PRODUCED BY THE JOHNSTON-BROADFOOT MODEL FOR EXCITED STATE EMITTERS
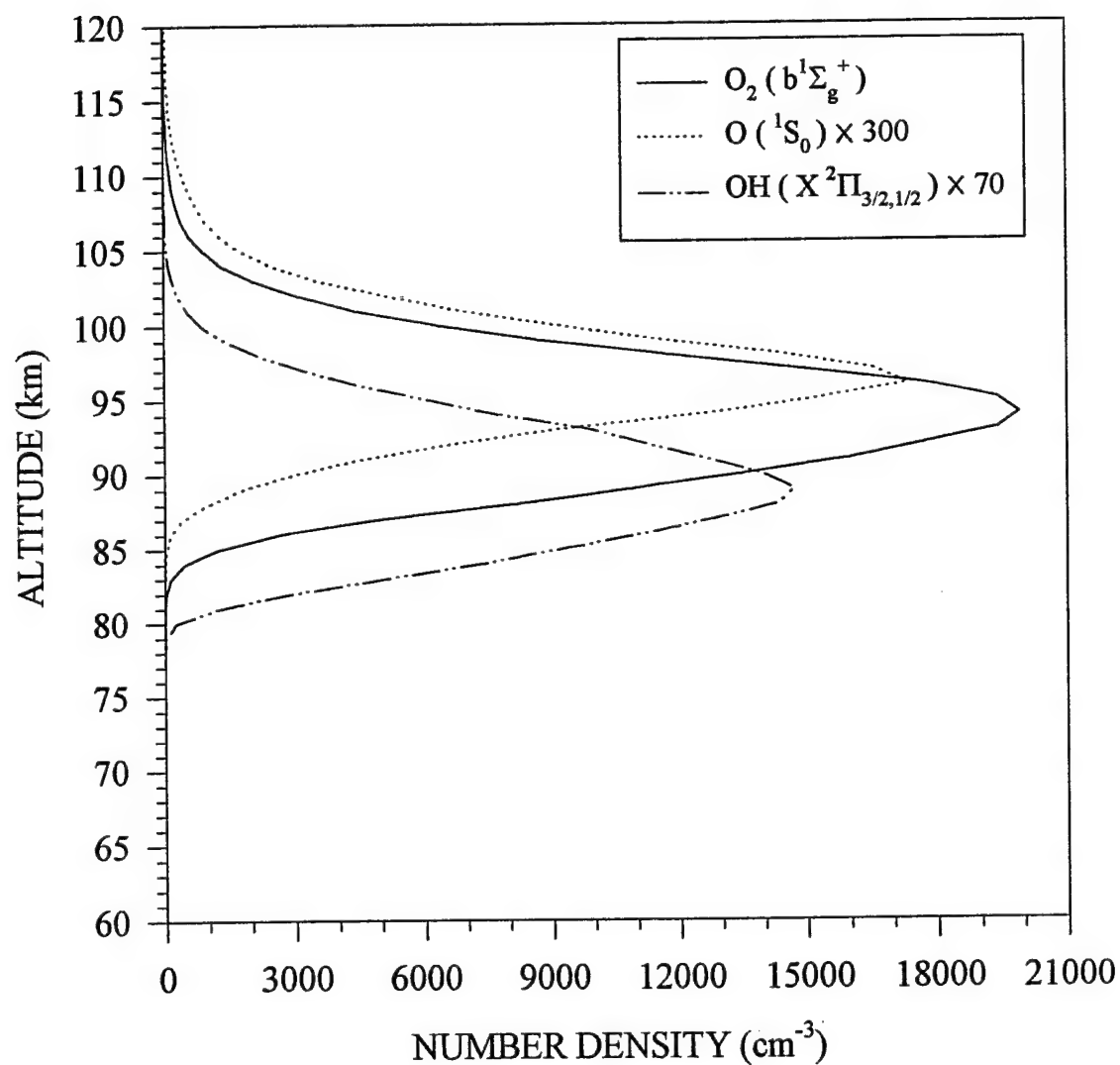
Figure F.1. Profiles of O_2(b $^1\Sigma_g$+), $O(^1S_0)$, and OH (X $^2\Pi_{3/2,1/2}$) produced by the Johnston-Broadfoot model. These excited states emit in the night airglow.

VOLUME EMISSION RATE PROFILES
FOR AIRGLOW EMISSIONS
# BASED ON THE JOHNSTON-BROADFOOT MODEL
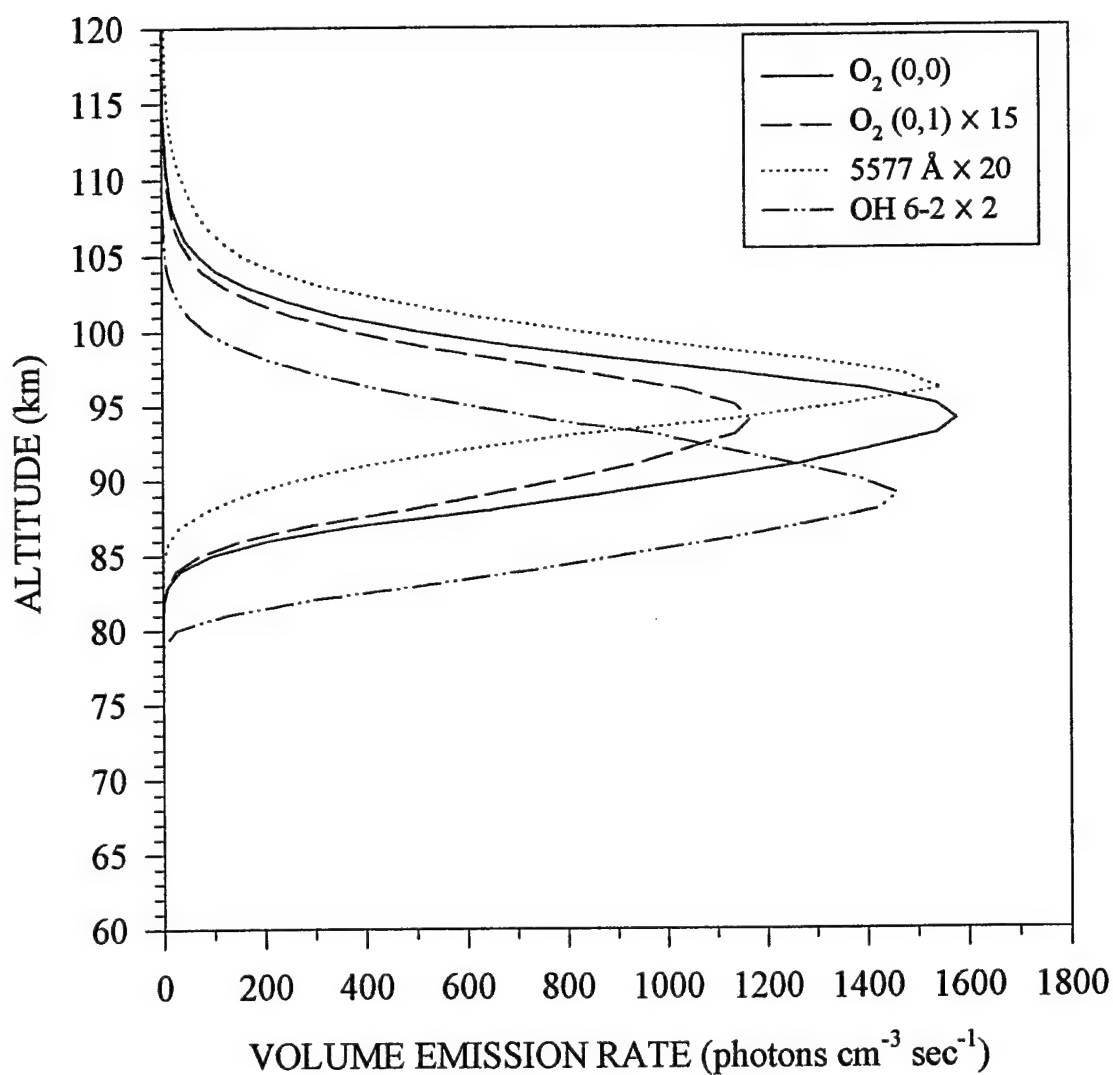
Figure F.2. Volume emission rate profiles for O_2 (0,0), O_2 (0,1), OI (5577 Å), and the OH Meinel (6,2) band, based on the Johnston-Broadfoot model output shown in Figure F.1.

INTEGRATED LINE OF SIGHT BRIGHTNESS PROFILES
FOR AIRGLOW EMISSIONS
BASED ON THE JOHNSTON-BROADFOOT MODEL
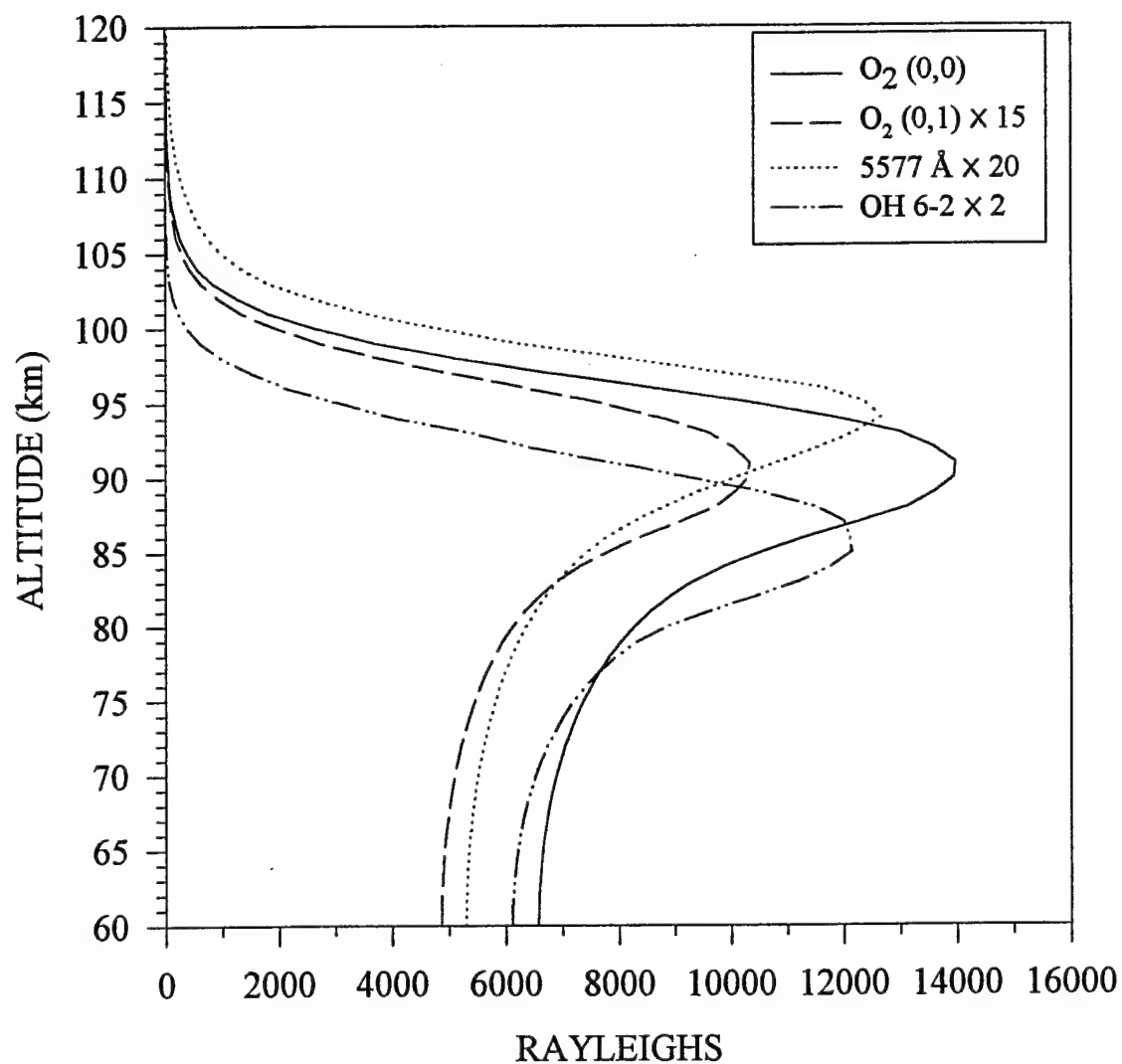
Figure F.3. Integrated line-of-sight (LOS) brightness profiles for the emissions of O_2 (0,0), O_2 (0,1), OI (5577 Å), and the OH Meinel (6,2) band, based on the Johnston-Broadfoot model output shown in Figure F.1.

```
/*  NIGHTGLOW.C
/*
/*                  AN ATMOSPHERIC MODEL FOR
/*          CALCULATING DENSITIES OF NIGHTGLOW SPECIES
/*
/*              MODEL BY DR. JEFF JOHNSTON (1992)
/*           WITH THE GUIDANCE OF DR. A. LYLE BROADFOOT
/*
/*      MODIFICATIONS AND UPDATES TO RATE COEFFICIENTS
/*   AND INPUT/OUTPUT FORMAT BY PAUL BELLAIRE (1995-96)
/*
/*   MODEL ASSUMPTIONS:
/*
/*   1)  THE DOWNWARD FLUX OF O IS CONSTANT
/*       THROUGHOUT THE NIGHT
/*
/*   2)  CONCENTRATION OF O2 AND N2 IS CONSTANT WITH
/*       RESPECT TO TIME
/*
/*   3)  DIFFUSION CAUSED BY TEMPERATURE GRADIENTS IS
/*       NEGLIGIBLE
/*
/*   4)  QUENCHING COEFFICIENTS FOR ALL O* STATES ARE
/*       THE SAME
/*
/*   5)  THE REVERSE CHEMICAL REACTIONS ARE NEGLIGIBLE
/*
/*   6)  THE HOx REACTIONS REACH LOCAL EQUILIBRIUM
/*
/*   7)  O(3P) DISAPPEARS IMMEDIATELY AFTER SUNSET
/*       BELOW 70 KM
/*
/*
/*
/*   PRODUCTION REACTIONS:          REFERENCE:
/*
```

```
/*     1) O + O + M -> O2* + M              Rodrigo et al. 1985
/*     2) O + O2 + M -> O3 + M              Rodrigo et al. 1991
/*     3) O + O3 -> O2 + O2                 Rodrigo et al. 1985
/*     4) H + O3 -> OH* + O2               Rodrigo et al. 1991
/*     5) O + OH -> O2 + H                  Rodrigo et al. 1991
/*     6) O + HO2 -> OH* + O2             Rodrigo et al. 1991
/*     7) OH + O3 -> O2 + HO2             Chamberlain & Hunten 1987
/*     8) H + O2 + M -> HO2 + M           Rodrigo et al. 1991
/*     9) HO2 + O3 -> OH + O2 + O2        Rodrigo et al. 1991
/*    10) OH + HO2 -> H2O + O2            Rodrigo et al. 1991
/*    11) H + HO2 -> H2 + O2              Rodrigo et al. 1991
/*
/*     QUENCHING REACTIONS:               REFERENCE:
/*
/*    12) O(1D) + O2 -> O(3P) + O2         Rodrigo et al. 1991
/*    13) O(1D) + N2 -> O(3P) + N2         Rodrigo et al. 1991
/*    14) O(1D) -> O + hv                  Radzig & Smirnov 1985
/*    15) O(1S) + O2 -> O(3P) + O2         Slanger 1972
/*    16) O(1S) + N2 -> O(3P) + N2         A.V. Jones 1974
/*    17) O(1S) + O -> O(3P) + O           Krauss & Neumann 1975
/*    18) O(1S) -> O(1D) + hv              Radzig & Smirnov 1985
/*    19) O(1S) -> O(3P) + hv              Radzig & Smirnov 1985
/*    20) O2(A3) + O2 -> O2(X3) + O2       Bates 1988
/*    21) O2(A3) + N2 -> O2(X3) + N2       Bates 1988
/*    22) O2(A3) + O -> O2(X3) + O         Bates 1988
/*    23) O2(A3) -> O2(X3) + hv            Bates 1989
/*    24) O2(A'3) + O2 -> O2(X3) + O2      Bates 1988
/*    25) O2(A'3) + N2 -> O2(X3) + N2      Bates 1988
/*    26) O2(A'3) -> O2(X3) + hv           Bates 1989
/*    27) O2(A'3) -> O2(a1) + hv           Bates 1989
/*    28) O2(c1) + O2 -> O2(X3) + O2       Bates 1988
/*    29) O2(c1) + N2 -> O2(X3) + N2       Bates 1988
/*    30) O2(c1) + O(3P) -> O2(X3) + O(1S) Bates 1988
/*    31) O2(c1) -> O2(X3) + hv            Bates 1989
/*    32) O2(b1) + N2 -> O2(X3) + N2       Bates 1988
/*    33) O2(b1) + O -> O2(X3) + O         Bates 1988
```

```
/*   34) O2(b1) -> O2(X3) + hv          Bates 1988
/*   35) O2(a1) + O2 -> O2 + O2         Bates 1988
/*   36) O2(a1) + O -> O2 + O           Bates 1988
/*   37) O2(a1) -> O2 + hv              Bates 1988


#include <stdio.h>
#include <math.h>
#include <string.h>
#include <stdlib.h>


/*      DEFINE CONSTANTS FOR SCALE HEIGHT DETERMINATION

#define AMUG_K 1.15e-5

/*      (AMUG_K, in Kelvin/cm, is given by the following formula:
/*   gravity * mass per particle * particles per mole / gas constant)

/* DEFINE ATOMS, MOLECULES, AND INITIAL CONCENTRATIONS
   (RODRIGO et al.)

/*      LET ALTITUDE [i] BE (i+60)

void set_var();
double T[61], D[61], K[61], N2_conc[61], O2_X3_conc[61], O3_conc[61];
double O_3P_conc[61] , H_conc[61], HO2_conc[61], OH_conc[61];
double O_1D_conc[61], O_1S_conc[61] , O2_a1_conc[61],
O2_b1_conc[61];
double O2_c1_conc[61], O2_A3_conc[61], O2_A3_ch_conc[61],
OH_oz_conc[61];
double O3_new[61], O2_X3_new[61], O_3P_new[61], H_new[61],
HO2_new[61];
double O_1D_new[61], O_1S_new[61], O2_a1_new[61], O2_b1_new[61],
O2_c1_new[61];
double O2_A3_new[61], O2_A3_ch_new[61], OH_new[61];


/*   INITIALIZE COLUMN DENSITIES
```

```c
double O3_col = 0.,O2_X3_col = 0.,O_3P_col = 0.,H_col = 0.,HO2_col =
0.;
double O_1D_col = 0.,O_1S_col = 0.,O2_a1_col = 0.,O2_b1_col =
0.,O2_c1_col = 0.;
double O2_A3_col = 0.,O2_A3_ch_col = 0.,OH_col = 0.;
char garb[20];
double
diff[7],alt,pres_time,delta_t,H_total,kay[4][4],kappa[3],O_const,max[7];
int i,j,k,iter,peak[7],lwn[3];
FILE *outfp,*emitfp,*timefp,*initfp;
main()
{
set_var(max,7,0.);
set_var(O_1D_conc,61,0.); set_var(O_1S_conc,61,0.);
set_var(O2_a1_conc,61,0.);
set_var(O2_b1_conc,61,0.); set_var(O2_c1_conc,61,0.);
set_var(O2_A3_conc,61,0.);
set_var(O2_A3_ch_conc,61,0.); set_var(OH_oz_conc,61,0.);
set_var(H_new,61,0.); set_var(OH_new,61,0.); set_var(HO2_new,61,0.);
set_var(O3_new,61,0.); set_var(O2_X3_new,61,0.);
set_var(O_3P_new,61,0.);
set_var(O_1D_new,61,0.); set_var(O_1S_new,61,0.);
set_var(O2_a1_new,61,0.);
set_var(O2_b1_new,61,0.); set_var(O2_c1_new,61,0.);
set_var(O2_A3_new,61,0.);
set_var(O2_A3_ch_new,61,0.);

printf("Please enter the filename of your initial conditions profile:\t");
scanf("%s",garb);
printf("\n");
initfp = fopen(garb,"r");
fscanf(initfp,"%s %s %s %s %s %s %s %s %s %s %s",garb, garb, garb, garb,
garb,
        garb, garb, garb, garb, garb, garb);
for(i=0; i<=60; i++){
```

```
          fscanf(initfp,"%d %lf %lf %lf %lf %lf %lf %lf %lf %lf %lf",
                  &j, &T[i], &D[i], &K[i], &N2_conc[i], &O2_X3_conc[i],
                  &O_3P_conc[i], &O3_conc[i], &H_conc[i], &OH_conc[i],
&HO2_conc[i]);
}
fclose(initfp);
initfp = fopen("init_conc","w");
fprintf(initfp,"%8s\t%8s\t%8s\t%8s\t%8s\t%8s\t%8s\n",
        "Altitude","[O(3P)] ","[O2]  ","[O3]  ","[OH]  ",
        "[H]   ","  [HO2]\n");
for(i=0;i<=60;i++){
        fprintf(initfp,"%8d\t%8.2e\t%8.2e\t%8.2e\t%8.2e\t%8.2e\t%8.2e\n",
                i+60,O_3P_conc[i],O2_X3_conc[i],O3_conc[i],
                OH_conc[i],H_conc[i],HO2_conc[i]);
}
fclose(initfp);
printf("Please enter the maximum number of time steps desired (dt = 5
min):\t");
scanf("%d",&iter);

/*              THE TIME INCREMENT IS 5 MIN = 300 SEC
/*  MODEL STARTS AT SUNSET AND ASSUMES MIDNIGHT 6 HRS =
    21600 SEC LATER

delta_t = 300.0;
pres_time = 0.0;
printf("\n\n");
timefp = fopen("time_conc","w");
fprintf(timefp,"%8s\t%8s\t%8s\t%8s\t%8s\t%8s\t%8s\t%8s\t%8s\n",
        "Time
(hrs)","[O(1S)]","[O(3P)]","[O2(A3)]","[O2(A'3)]","[O2(c1)]","[O2(b1)]","[
O2(a1)]","[OH']\n");


/*      START TIME LOOP
```

```c
for(j=0;j<iter;j++){

        pres_time += delta_t;
        if(pres_time >= 21600.0){ printf("Midnight!\n"); }

/*      START ALTITUDE LOOP

        for(i=0;i<=60;i++){

/*      CALCULATE MOLECULAR AND EDDY DIFFUSION EFFECTS
/*      AND APPLY BOUNDARY CONDITIONS FOR DIFFUSION

                if(i==0){
                        diff[1] = 0.;
                        diff[2] = 0.;
                        diff[3] = ((((4.0*D[i+1]+K[i+1])/2.0e5)*
                                (H_conc[i+1]-H_conc[i]+
                                (H_conc[i+1]/T[i+1])*(T[i+1]-T[i]))+H_conc[i+1]*
                                (4.0*D[i+1]*(1.0*AMUG_K/T[i+1])+K[i+1]*
                                (28.*AMUG_K/T[i+1]))-3.9e6)/2.0e5;
                        diff[3] = 0.;
                        diff[4] = 0.;
                        diff[5] = 0.;
                }
                if(i==60){
                        diff[1] = (1.4e12-(((D[i]+K[i])/2.0e5)*
                                (O_3P_conc[i]-O_3P_conc[i-1]+
                                (O_3P_conc[i]/T[i])*(T[i]-T[i-1]))+O_3P_conc[i]*
                                (D[i]*(16.*AMUG_K/T[i])+K[i]*
                                (28.*AMUG_K/T[i]))))/2.0e5;
                        diff[2] = 0.;
                        diff[3] = 0.;
                        diff[4] = 0.;
                        diff[5] = 0.;
                }
```

```
/*      O(3P) STATE

        if(i>0 && i<60){
                diff[1] = (((D[i+1]+K[i+1])/2.0e5)*(O_3P_conc[i+1]-
                        O_3P_conc[i]+(O_3P_conc[i+1]/T[i+1])*
                        (T[i+1]-T[i]))+O_3P_conc[i+1]*
                        (D[i+1]*(16.*AMUG_K/T[i+1])+K[i+1]*
                        (28.*AMUG_K/T[i+1]))-
                        (((D[i]+K[i])/2.0e5)*
                        (O_3P_conc[i]-O_3P_conc[i-1]+
                        (O_3P_conc[i]/T[i])*(T[i]-T[i-1]))+O_3P_conc[i]*
                        (D[i]*(16.*AMUG_K/T[i])+K[i]*
                        (28.*AMUG_K/T[i]))))/2.0e5;
```

```
/*      O3 MOLECULE

                diff[2] = (((D[i+1]+K[i+1])/2.0e5)*
                        (O3_conc[i+1]-O3_conc[i]+
                        (O3_conc[i+1]/T[i+1])*
                        (T[i+1]-T[i]))+O3_conc[i+1]*
                        (D[i+1]*(48.*AMUG_K/T[i+1])+K[i+1]*
                        (28.*AMUG_K/T[i+1]))-
                        (((D[i]+K[i])/2.0e5)*
                        (O3_conc[i]-O3_conc[i-1]+
                        (O3_conc[i]/T[i])*(T[i]-T[i-1]))+O3_conc[i]*
                        (D[i]*(48.*AMUG_K/T[i])+K[i]*
                        (28.*AMUG_K/T[i]))))/2.0e5;
```

```
/*      H ATOM

                diff[3] = (((4.0*D[i+1]+K[i+1])/2.0e5)*
                        (H_conc[i+1]-H_conc[i]+
                        (H_conc[i+1]/T[i+1])*(T[i+1]-T[i]))+H_conc[i+1]*
                        (4.0*D[i+1]*(1.0*AMUG_K/T[i+1])+K[i+1]*
                        (28.*AMUG_K/T[i+1]))-
                        (((4.0*D[i]+K[i])/2.0e5)*
```

```
                    (H_conc[i]-H_conc[i-1]+
                    (H_conc[i]/T[i])*(T[i]-T[i-1]))+H_conc[i]*
                    (4.0*D[i]*(1.0*AMUG_K/T[i])+K[i]*
                    (28.*AMUG_K/T[i]))))/2.0e5;
```

/*   HO2 MOLECULE

```
        diff[4] = (((D[i+1]+K[i+1])/2.0e5)*
                    (HO2_conc[i+1]-HO2_conc[i]+
                    (HO2_conc[i+1]/T[i+1])*
                    (T[i+1]-T[i]))+HO2_conc[i+1]*
                    (D[i+1]*(33.*AMUG_K/T[i+1])+K[i+1]*
                    (28.*AMUG_K/T[i+1]))-
                    (((D[i]+K[i])/2.0e5)*
                    (HO2_conc[i]-HO2_conc[i-1]+
                    (HO2_conc[i]/T[i])*(T[i]-T[i-1]))+HO2_conc[i]*
                    (D[i]*(33.*AMUG_K/T[i])+K[i]*
                    (28.*AMUG_K/T[i]))))/2.0e5;
```

/*   OH MOLECULE

```
        diff[5] = (((D[i+1]+K[i+1])/2.0e5)*
                    (OH_conc[i+1]-OH_conc[i]+
                    (OH_conc[i+1]/T[i+1])*(T[i+1]-T[i]))+

OH_conc[i+1]*(D[i+1]*(17.*AMUG_K/T[i+1])+K[i+1]*
                    (28.*AMUG_K/T[i+1]))-(((D[i]+K[i])/2.0e5)*
                    (OH_conc[i]-OH_conc[i-1]+
                    (OH_conc[i]/T[i])*(T[i]-T[i-1]))+OH_conc[i]*
                    (D[i]*(17.*AMUG_K/T[i])+K[i]*
                    (28.*AMUG_K/T[i]))))/2.0e5;
        }
```

/*   CALCULATE CHEMICAL SOURCES/SINKS
/* ASSUME HOx CYCLE EQUILIBRATES IMMEDIATELY

/*   AND CALCULATE CONCENTRATIONS
/* (THIS IS THE EFFECT OF REACTIONS 4 TO 11)
/*   SOURCE: "COMPREHENSIVE CHEMICAL KINETICS"
         (BAMFORD), P.32

```
H_total = H_conc[i]+OH_conc[i]+HO2_conc[i]+
        ((diff[3]+diff[4]+diff[5])-(2.0*OH_conc[i]*
        HO2_conc[i]*1.7e-11*exp(416.0/T[i])+2.0*H_conc[i]*
        HO2_conc[i]*6.66e-12))*delta_t;

kay[1][2] = O3_conc[i]*1.4e-10*exp(-470.0/T[i]);
kay[1][3] = O2_X3_conc[i]*(O2_X3_conc[i]+N2_conc[i])*
                    5.5e-32*pow(T[i]/300.0,-1.6);
kay[2][1] = O_3P_conc[i]*2.2e-11*exp(117.0/T[i]);
kay[2][3] = O3_conc[i]*1.6e-12*exp(-940.0/T[i]);
kay[3][1] = 0.;
kay[3][2] = O_3P_conc[i]*3.0e-11*exp(200.0/T[i])+
        O3_conc[i]*1.4e-14*exp(-580.0/T[i]);

kappa[1] = (kay[1][2]*kay[3][2]+kay[1][2]*kay[3][1]+
        kay[3][2]*kay[1][3])/(kay[2][1]*kay[3][2]+
        kay[2][1]*kay[3][1]+kay[2][3]*kay[3][1]);

kappa[2] = (kay[1][2]*kay[2][3]+kay[2][1]*kay[1][3]+
        kay[2][3]*kay[1][3])/(kay[1][2]*kay[3][2]+
        kay[1][2]*kay[3][1]+kay[3][2]*kay[1][3]);

H_new[i] = H_total/(1+kappa[1]+kappa[1]*kappa[2]);

OH_new[i] = H_new[i]*kappa[1];
```

/*   IN THE CALCULATIONS THAT FOLLOW,
/* CERTAIN RATE COEFFICIENTS HAVE BEEN MODIFIED; SEE

```
/*              JOHNSTON &  BROADFOOT (J&B), 1993
/*                 AND J&B CORRECTION, 1994
/*   CASCADE COEFFICIENT FROM McDADE & LLEWELLYN, 1987


       OH_oz_conc[i] = H_new[i]*kay[1][2]*0.32/(276.0+
              (O2_X3_conc[i]+N2_conc[i])*1.5e-11*0.934+
              1.5e-10*O_3P_conc[i]);


       HO2_new[i] = H_new[i]*kappa[1]*kappa[2];


/*     DETERMINE OZONE CONCENTRATION

/*     SOURCES: REACTION 2      LOSSES:     REACTIONS 3,4,7,9


       if(i<26){
              O3_new[i] = delta_t*(diff[2]-((O_3P_conc[i]*
                     8.0e-12*exp(-2060.0/T[i])+H_conc[i]*1.4e-10*
                     exp(-470.0/T[i])+OH_conc[i]*1.6e-12*
                     exp(-940.0/T[i])+HO2_conc[i]*1.4e-14*
                     exp(-580.0/T[i]))*O3_conc[i]))+
                     O_3P_conc[i]*(1-exp(-6.0e-34*
                     pow((T[i]/300.),-2.3)*O2_X3_conc[i]*
                     (N2_conc[i]+O2_X3_conc[i])*delta_t));
       }else{
              O3_new[i] = delta_t*((diff[2]+O_3P_conc[i]*
                     O2_X3_conc[i]*(N2_conc[i]+ O2_X3_conc[i])*
                     6.0e-34*pow((T[i]/300.0),-2.3))-((O_3P_conc[i]*
                     8.0e-12*exp(-2060.0/T[i])+H_conc[i]*1.4e-10*
                     exp(-470.0/T[i])+OH_conc[i]*1.6e-12*
                     exp(-940.0/T[i])+HO2_conc[i]*1.4e-14*
                     exp(-580.0/T[i]))*O3_conc[i]));
       }

/*     DETERMINE O(3P) CONCENTRATION
/*     SOURCES: NONE CHEMICAL
```

```
/*      LOSSES: REACTIONS 1,2,3,5,6

            if(i<26){
                O_const =
O2_X3_conc[i]*(O2_X3_conc[i]+N2_conc[i])*
                    6.0e-34*pow((T[i]/300.0),-2.3)+
                    OH_conc[i]*2.2e-11*exp(117.0/T[i])+
                    HO2_conc[i]*3.0e-11*exp(200.0/T[i]);

                O_3P_new[i] = delta_t*((diff[1])-
                    (2.0*O_3P_conc[i]*O_3P_conc[i]*(N2_conc[i]+
                    O2_X3_conc[i])*9.4e-34*exp(484.0/T[i])+
                    O_3P_conc[i]*O3_conc[i]*8.0e-12*
                    exp(-2060.0/T[i])))+
                    O_3P_conc[i]*(exp(-O_const*delta_t)-1.);
            }else{
                O_3P_new[i] = delta_t*((diff[1])-
                    (2.0*O_3P_conc[i]*O_3P_conc[i]*(N2_conc[i]+
                    O2_X3_conc[i])*9.4e-34*exp(484.0/T[i])+
                    O_3P_conc[i]*O2_X3_conc[i]*(N2_conc[i]+
                    O2_X3_conc[i])*6.0e-34*pow((T[i]/300.0),-2.3)+
                    O_3P_conc[i]*O3_conc[i]*8.0e-12*
                    exp(-2060.0/T[i])+O_3P_conc[i]*OH_conc[i]*
                    2.2e-11*exp(117.0/T[i])+O_3P_conc[i]*
                    HO2_conc[i]*3.0e-11*exp(200.0/T[i])));
            }

/*      DETERMINE O(1S) CONCENTRATION (STEADY STATE)
/*      SOURCE: REACTION 30      LOSSES:  REACTIONS 15-19

        O_1S_conc[i] = (O2_c1_conc[i]*O_3P_conc[i]*3.7e-12)/
            (O2_X3_conc[i]*4.0e-12*exp(-870.0/T[i])+
            N2_conc[i]*5.0e-17+O_3P_conc[i]*2.0e-14+
            1.28+0.078);

/*      DETERMINE O(1D) CONCENTRATION (STEADY STATE)
```

```
/*      SOURCE: REACTION 18      LOSSES:  REACTIONS 12-14

      O_1D_conc[i] = (O_1S_conc[i]*1.28)/(O2_X3_conc[i]*
             3.2e-11*exp(67.0/T[i])+N2_conc[i]*1.8e-11*
             exp(107.0/T[i])+9.1e-3);

/* THE FACTORS 0.07, 0.03, 0.04, 0.18, AND 0.06 THAT FOLLOW ARE
/*   THE APPROPRIATE RATIOS FOR THE VARIOUS STATES OF O2

/* DETERMINE O2(a1) CONCENTRATION (STEADY STATE)
/* SOURCES: REACTIONS 1,27,32,33     LOSSES: REACTIONS 35-37


         O2_a1_conc[i] =
(0.07*O_3P_conc[i]*O_3P_conc[i]*(N2_conc[i]+
             O2_X3_conc[i])*9.4e-34*exp(484.0/T[i])+
             O2_A3_ch_conc[i]*5.2e-1+O2_b1_conc[i]*
             N2_conc[i]*2.2e-15+O2_b1_conc[i]*O_3P_conc[i]*8.0e-
14)/
             (O2_X3_conc[i]*1.5e-18+O_3P_conc[i]*1.6e-16+1.9e-
4);

/* DETERMINE O2(b1) CONCENTRATION (STEADY STATE)
/* SOURCES: REACTION 1        LOSSES:  REACTIONS 32-34

         O2_b1_conc[i] =
(0.03*O_3P_conc[i]*O_3P_conc[i]*(N2_conc[i]+
             O2_X3_conc[i])*9.4e-34*exp(484.0/T[i]))/
             ((N2_conc[i]*2.8e-15+ O_3P_conc[i]*1.0e-13)+8.7e-2);




/* DETERMINE O2(c1) CONCENTRATION (STEADY STATE)
/* SOURCES: REACTION 1        LOSSES:  REACTIONS 28-31
```

```
              O2_c1_conc[i] =
(0.04*O_3P_conc[i]*O_3P_conc[i]*(N2_conc[i]+
              O2_X3_conc[i])*9.4e-34*exp(484.0/T[i]))/
              ((O2_X3_conc[i]*9.3e-12+ N2_conc[i]*2.5e-12)+
              O_3P_conc[i]*2.7e-12+0.55);


/*  DETERMINE O2(A'3) CONCENTRATION (STEADY STATE)
/*  SOURCES: REACTION 1          LOSSES:  REACTIONS 24-27


              O2_A3_ch_conc[i] = (0.18*O_3P_conc[i]*O_3P_conc[i]*
              (N2_conc[i]+O2_X3_conc[i])*9.4e-34*exp(484.0/T[i]))/
              ((O2_X3_conc[i]*6.7e-11+N2_conc[i]*
              1.8e-11)+8.8e-1+8.4e-1);


/*  DETERMINE O2(A3) CONCENTRATION (STEADY STATE)
/*  SOURCES: REACTION 1          LOSSES:  REACTIONS 20-23


              O2_A3_conc[i] =
(0.06*O_3P_conc[i]*O_3P_conc[i]*(N2_conc[i]+
              O2_X3_conc[i])*9.4e-34*exp(484.0/T[i]))/
              ((O2_X3_conc[i]*1.0e-10+ N2_conc[i]*2.5e-11)+
              O_3P_conc[i]*1.5e-11+10.7);
       }


/*      REINITALIZE COLUMN DENSITIES

              O_3P_col=0.;              O_1D_col=0.;
              O_1S_col=0.;              O2_X3_col=0.;
              O2_a1_col=0.;             O2_b1_col=0.;
              O2_c1_col=0.;             O2_A3_ch_col=0.;
              O2_A3_col=0.;             OH_col=0.;
              O3_col=0.;                HO2_col=0.;
              H_col=0.;

              for(i=0;i<=60;i++){
```

```
/*      CALCULATE COLUMN DENSITIES

            O_3P_col += O_3P_conc[i]*2.0e5;
            O_1D_col += O_1D_conc[i]*2.0e5;
            O_1S_col += O_1S_conc[i]*2.0e5;
            O2_X3_col += O2_X3_conc[i]*2.0e5;
            O2_a1_col += O2_a1_conc[i]*2.0e5;
            O2_b1_col += O2_b1_conc[i]*2.0e5;
            O2_c1_col += O2_c1_conc[i]*2.0e5;
            O2_A3_ch_col += O2_A3_ch_conc[i]*2.0e5;
            O2_A3_col += O2_A3_conc[i]*2.0e5;
            OH_col += OH_oz_conc[i]*2.0e5;
            HO2_col += HO2_conc[i]*2.0e5;
            H_col += H_conc[i]*2.0e5;
            O3_col += O3_conc[i]*2.0e5;

/*      DETERMINE CONCENTRATIONS FOR NEXT TIME STEP

            O3_conc[i] += O3_new[i];
            O_3P_conc[i] += O_3P_new[i];
            H_conc[i] = H_new[i];
            OH_conc[i] = OH_new[i];
            HO2_conc[i] = HO2_new[i];

            if(O_3P_conc[i] <= 1.0e-4){ O_3P_conc[i] = 1.0e-4; }
            if(O3_conc[i] <= 1.0e-4){ O3_conc[i] = 1.0e-4; }
            if(H_conc[i] <= 1.0e-4){ H_conc[i] = 1.0e-4; }
            if(OH_conc[i] <= 1.0e-4){ OH_conc[i] = 1.0e-4; }
            if(HO2_conc[i] <= 1.0e-4){ HO2_conc[i] = 1.0e-4; }
        }


/*      PRINT SPECIFIC COLUMN DENSITIES
```

```
      if(j == 0){
             printf("Program completed!\n");
/*       printf("Iteration  O(1S)    O(3P)    O2[A3]   O2[A'3]   O2[c1]
O2[b1]    O2[a1]     OH'\n"); */

      }
/*       printf("    % 3d % 8.2e % 8.2e % 8.2e % 8.2e % 8.2e % 8.2e % 8.2e
% 8.2e\n",*/
/*             j,O_1S_col,O_3P_col,O2_A3_col,O2_A3_ch_col,O2_c1_col,*/
/*             O2_b1_col,O2_a1_col,OH_col);*/

      fprintf(timefp,"%8.4f\t%8.2e\t%8.2e\t%8.2e\t%8.2e\t%8.2e\t%8.2e\t%
8.2e\t%8.2e\n",

      (float)(j+1)/12.,O_1S_col,O_3P_col,O2_A3_col,O2_A3_ch_col,O2_c
1_col,
             O2_b1_col,O2_a1_col,OH_col);
}
outfp = fopen("reac_conc","w");
emitfp = fopen("emit_conc","w");
printf("\nThe initial concentration altitude profiles are in the file
'init_conc'.\n");
printf("The end-of-run emitter altitude profiles are in the file 'emit_conc'.\n");
printf("The end-of-run reactant altitude profiles are in the file 'reac_conc'.\n");
printf("The time-dependent vertical column densities and end-of-run altitudes
of peak emissions are in the file 'time_conc'.\n");
printf("\n");
fprintf(outfp,\
      "%8s\t%8s\t%8s\t%8s\t%8s\t%8s\t%8s\n",
      "Altitude","[O(3P)]","[O2] ","[O3] ",
      "[OH] ","[H]   "," [HO2]\n");
fprintf(emitfp,\
      "%8s\t%8s\t%8s\t%8s\t%8s\t%8s\t%8s\t%8s\n",\
      "Altitude","[O2(A3)]","[O2(A'3)]",
      "[O2(c1)]","[O2(b1)]","[O2(a1)]"," [O(1S)]"," [OH'] \n");
for(i=0;i<=60;i++){
      fprintf(outfp,"%8d\t%8.2e\t%8.2e\t%8.2e\t%8.2e\t%8.2e\t%8.2e\n",
```

```c
                i+60,O_3P_conc[i],O2_X3_conc[i],O3_conc[i],
                OH_conc[i],H_conc[i],HO2_conc[i]);
        fprintf(emitfp,"%8d\t%8.2e\t%8.2e\t%8.2e\t%8.2e\t%8.2e\t%8.2e\t%8.2e\n",
                i+60,O2_A3_conc[i],O2_A3_ch_conc[i],O2_c1_conc[i],
                O2_b1_conc[i],O2_a1_conc[i],O_1S_conc[i],OH_oz_conc[i]);
        if(O2_A3_conc[i]>max[0]){
                max[0]=O2_A3_conc[i];
                peak[0]=i;
        }
        if(O2_A3_ch_conc[i]>max[1]){
                max[1]=O2_A3_ch_conc[i];
                peak[1]=i;
        }
        if(O2_a1_conc[i]>max[6]){
                max[6]=O2_a1_conc[i];
                peak[6]=i;
        }
        if(O2_c1_conc[i]>max[2]){
                max[2]=O2_c1_conc[i];
                peak[2]=i;
        }
        if(O2_b1_conc[i]>max[3]){
                max[3]=O2_b1_conc[i];
                peak[3]=i;
        }
        if(O_1S_conc[i]>max[4]){
                max[4]=O_1S_conc[i];
                peak[4]=i;
        }
        if(OH_oz_conc[i]>max[5]){
                max[5]=OH_oz_conc[i];
                peak[5]=i;
        }
}
fprintf(timefp,"\nAltitudes of peak emission (in kms):\n");
```

```c
fprintf(timefp,"\t\tHerzberg I\t\t%d\n",peak[0]+60);
fprintf(timefp,"\t\tHerzberg II\t\t%d\n",peak[2]+60);
fprintf(timefp,"\t\tChamberlain\t\t%d\n",peak[1]+60);
fprintf(timefp,"\t\tOI 5577\t\t\t%d\n",peak[4]+60);
fprintf(timefp,"\t\tAtmospheric\t\t%d\n",peak[3]+60);
fprintf(timefp,"\t\tIR Atmospheric\t\t%d\n",peak[6]+60);
fprintf(timefp,"\t\tMeinel\t\t\t%d\n\n",peak[5]+60);
fclose(outfp);
fclose(timefp);
fclose(emitfp);
}
void set_var(a, max, set_no)
double *a, set_no;
int max;
{
      int i;
      for(i=0; i<max; i++){
              a[i] = set_no;
      }
}
```

END OF JOHNSTON-BROADFOOT MODEL

APPENDIX G: THE ATMOSPHERIC VERTICAL PROFILE INPUT TO THE JOHNSTON-BROADFOOT MODEL

Alt km	Temp K	Molec cm^2/s	Eddy cm^2/s	$[N_2]$ cm^{-3}	$[O_2]$ cm^{-3}	$[O]$ cm^{-3}	$[O_3]$ cm^{-3}	$[H]$ cm^{-3}	$[OH]$ cm^{-3}	$[HO_2]$ cm^{-3}
60	243.	1.0e3	2.2e5	5.0e15	1.4e15	6.0e9	6.0e9	2.5e6	1.0e7	4.3e6
61	240.	1.1e3	2.2e5	4.4e15	1.2e15	5.8e9	4.7e9	2.7e6	9.0e6	3.9e6
62	238.	1.3e3	2.3e5	3.9e15	1.1e15	5.7e9	3.5e9	3.0e6	8.1e6	3.4e6
63	236.	1.5e3	2.4e5	3.5e15	9.7e14	5.5e9	2.7e9	3.5e6	7.6e6	3.2e6
64	234.	1.7e3	2.5e5	3.0e15	8.5e14	5.3e9	2.0e9	4.0e6	7.2e6	3.1e6
65	231.	1.9e3	2.6e5	2.7e15	7.5e14	5.1e9	1.6e9	5.4e6	6.8e6	3.0e6
66	229.	2.2e3	2.7e5	2.4e15	6.6e14	4.9e9	1.2e9	6.7e6	6.5e6	2.9e6
67	227.	2.5e3	2.8e5	2.1e15	5.8e14	4.8e9	9.7e8	8.3e6	6.3e6	2.8e6
68	225.	2.8e3	3.0e5	1.8e15	5.1e14	4.8e9	7.5e8	1.0e7	6.2e6	2.7e6
69	222.	3.2e3	3.2e5	1.6e15	4.5e14	4.9e9	6.1e8	1.4e7	6.2e6	2.7e6
70	220.	3.6e3	3.4e5	1.4e15	4.0e14	4.9e9	4.9e8	1.7e7	6.2e6	2.7e6
71	219.	4.1e3	3.5e5	1.3e15	3.5e14	5.3e9	4.1e8	2.2e7	5.6e6	2.4e6
72	218.	4.6e3	3.6e5	1.1e15	3.0e14	5.7e9	3.3e8	2.7e7	5.0e6	2.2e6
73	218.	5.3e3	3.7e5	9.6e14	2.7e14	7.3e9	3.0e8	3.3e7	4.1e6	1.7e6
74	218.	6.0e3	3.8e5	8.2e14	2.3e14	9.0e9	2.8e8	3.9e7	3.2e6	1.3e6
75	217.	6.9e3	3.8e5	7.1e14	2.0e14	1.1e10	2.4e8	4.1e7	2.3e6	9.5e5
76	216.	7.7e3	3.9e5	6.1e14	1.7e14	1.2e10	2.1e8	4.3e7	1.5e6	5.9e5
77	214.	9.0e3	4.0e5	5.3e14	1.5e14	1.4e10	1.8e8	4.2e7	1.1e6	3.6e5
78	213.	1.0e4	4.0e5	4.6e14	1.3e14	1.5e10	1.5e8	4.2e7	6.6e5	2.3e5
79	211.	1.2e4	4.1e5	4.1e14	1.1e14	2.2e10	1.7e8	3.8e7	4.3e5	1.4e5
80	209.	1.4e4	4.1e5	3.6e14	1.0e14	3.0e10	1.9e8	3.4e7	2.0e5	5.3e4
81	207.	1.7e4	4.2e5	3.1e14	8.7e13	4.7e10	2.1e8	3.0e7	1.1e5	3.1e4
82	206.	1.9e4	4.2e5	2.6e14	7.3e13	6.5e10	2.3e8	2.5e7	4.3e4	8.7e3
83	204.	2.3e4	4.3e5	2.2e14	6.3e13	9.2e10	2.2e8	2.1e7	2.6e4	5.0e3
84	202.	2.7e4	4.5e5	1.9e14	5.3e13	1.2e11	2.2e8	1.7e7	1.2e4	1.3e3
85	200.	3.2e4	4.6e5	1.6e14	4.5e13	1.7e11	2.1e8	1.5e7	7.7e3	8.0e2
86	199.	3.7e4	4.8e5	1.4e14	3.8e13	2.2e11	1.9e8	1.3e7	3.4e3	3.0e2
87	197.	4.4e4	4.9e5	1.2e14	3.3e13	2.8e11	1.5e8	1.5e7	2.8e3	2.1e2
88	195.	5.2e4	5.0e5	1.0e14	2.8e13	3.5e11	1.2e8	1.7e7	2.2e3	1.3e2
89	193.	6.2e4	5.5e5	8.5e13	2.4e13	3.8e11	1.1e8	2.6e7	2.2e3	1.2e2
90	192.	7.2e4	6.0e5	7.1e13	2.0e13	4.1e11	9.0e7	3.5e7	2.3e3	1.2e2
91	194.	8.6e4	6.2e5	6.0e13	1.7e13	4.6e11	7.2e7	4.4e7	1.9e3	9.6e1
92	196.	1.0e5	6.5e5	5.0e13	1.4e13	5.2e11	5.4e7	5.2e7	1.5e3	7.1e1
93	194.	1.2e5	6.7e5	4.2e13	1.2e13	5.4e11	4.1e7	5.4e7	1.1e3	4.9e1
94	192.	1.5e5	7.0e5	3.4e13	9.4e12	5.6e11	2.8e7	5.5e7	7.6e2	2.7e1
95	193.	1.9e5	7.5e5	2.8e13	7.9e12	6.0e11	2.0e7	5.2e7	5.2e2	1.9e1

Alt km	Temp K	Molec cm²/s	Eddy cm²/s	[N₂] cm⁻³	[O₂] cm⁻³	[O] cm⁻³	[O₃] cm⁻³	[H] cm⁻³	[OH] cm⁻³	[HO₂] cm⁻³
96	195.	2.2e5	8.0e5	2.3e13	6.4e12	6.3e11	1.3e7	5.0e7	2.9e2	1.1e1
97	197.	2.7e5	1.0e6	1.9e13	5.4e12	6.1e11	9.7e6	4.5e7	2.0e2	7.5
98	198.	3.2e5	1.3e6	1.6e13	4.4e12	5.9e11	6.4e6	4.0e7	1.2e2	4.0
99	202.	3.9e5	1.3e6	1.3e13	3.7e12	5.6e11	4.4e6	3.6e7	8.5e1	2.5
100	206.	4.6e5	1.4e6	1.1e13	3.0e12	5.2e11	2.4e6	3.2e7	5.0e1	1.1
101	209.	5.7e5	1.4e6	8.5e12	2.5e12	4.9e11	1.7e6	2.8e7	3.3e1	1.0
102	212.	6.8e5	1.4e6	7.1e12	2.0e12	4.5e11	1.0e6	2.4e7	1.7e1	0.9
103	216.	8.4e5	1.4e6	5.8e12	1.7e12	3.9e11	6.5e6	2.1e7	1.2e1	0.6
104	220.	1.0e6	1.4e6	4.6e12	1.3e12	3.4e11	3.0e5	1.8e7	7.0	0.3
105	224.	1.3e6	1.4e6	3.8e12	1.1e12	3.1e11	1.9e5	1.5e7	5.0	0.2
106	229.	1.6e6	1.4e6	3.0e12	8.3e11	2.9e11	9.0e4	1.2e7	2.8	0.11
107	234.	2.0e6	1.3e6	2.4e12	6.9e11	2.6e11	5.8e4	1.1e7	2.0	0.07
108	240.	2.5e6	1.2e6	1.9e12	5.4e11	2.3e11	2.6e4	9.3e6	1.0	3.8e-2
109	246.	3.2e6	1.4e6	1.6e12	4.4e11	2.2e11	1.7e4	8.5e6	0.7	2.5e-2
110	252.	4.0e6	1.7e6	1.4e12	3.5e11	2.2e11	8.0e3	7.7e6	0.3	1.2e-2
111	260.	5.2e6	1.9e6	1.2e12	2.9e11	2.0e11	5.2e3	6.8e6	0.16	1.0e-2
112	268.	6.3e6	2.1e6	1.1e12	2.4e11	1.8e11	2.4e3	5.9e6	1.0e-2	8.0e-3
113	275.	8.1e6	2.2e6	9.7e11	2.1e11	1.6e11	1.6e3	5.1e6	8.0e-3	6.0e-3
114	283.	1.0e7	2.4e6	8.5e11	1.7e11	1.5e11	7.6e2	4.4e6	6.0e-3	4.0e-3
115	290.	1.1e7	1.5e6	7.5e11	1.4e11	1.4e11	5.5e2	4.0e6	3.7e-3	2.0e-3
116	302.	1.2e7	6.0e5	6.6e11	1.2e11	1.3e11	3.4e2	3.5e6	1.5e-3	1.0e-4
117	311.	1.4e7	4.6e5	5.8e11	1.0e11	1.2e11	2.6e2	3.3e6	1.1e-3	7.3e-5
118	320.	1.5e7	3.2e5	5.1e11	8.0e10	1.2e11	1.7e2	3.1e6	7.0e-4	4.8e-5
119	330.	1.7e7	2.4e5	4.5e11	6.7e10	1.1e11	1.3e2	2.8e6	4.2e-4	2.7e-5
120	341.	1.8e7	1.6e5	4.0e11	5.5e10	1.1e11	9.0e1	2.5e6	1.5e-4	1.1e-5

Data Sources (from Johnston, 1992):

•Temperature: 1976 US Standard Atmosphere (January) for 60-90 km; AFGL (1985) for 92-120 km, interpolated such that temperatures matched at 90 km.

•Molecular Diffusion Coefficient: Rodrigo et al. (1986)

•Eddy Diffusion Coefficient: Rodrigo et al. (1986)

•[N₂]   : Chamberlain and Hunten (1987), logarithmic interpolation.

•[O₂]   : Constant proportion of N_2 number density.

•[O]   : Rodrigo et al. (1991)

•[O₃]   : Rodrigo et al. (1991)

•[H]   : Rodrigo et al. (1991)

•[OH]   : Rodrigo et al. (1991)

•[HO₂] : Rodrigo et al. (1991)

REFERENCES

Air Force Geophysics Laboratory, <u>Handbook of Geophysics and the Space Environment</u>, Adolph S. Jursa, editor; AFGL, Air Force Systems Command, Hanscom AFB, Massachusetts, 1985.

Akmaev, R. A., and G. M. Shved, "Modelling of the composition of the lower thermosphere taking into account of the dynamics with applications to tidal variations of the [OI] 5577 Å airglow," J. Atm. Terr. Phys., 42, 705, 1980.

Allen, M., J. I. Lunine, and Y. L. Yung, "The vertical distribution of ozone in the mesosphere and lower thermosphere," J. Geophys. Res., 89, 4841, 1984.

Barr, W. L., "Method for computing the radial distribution of emitters in a cylindrical source," J. Opt. Soc. Amer., 52, 885, 1962.

Bates, David R., "Nightglow emissions from oxygen in the lower thermosphere," Planet. Sp. Sci., 40, #2/3, 211, 1992.

Bates, David R., "Emission of forbidden red and green lines of atomic oxygen from the nocturnal F region," Planet. Sp. Sci., 40, #7, 893, 1992.

Bilitza, D., "International Reference Ionosphere 1990," Technical Report NSSDC/WDC-A-R&S 90-22, National Space Science Data Center, World Data Center A for Rockets and Satellites, NASA Goddard Space Flight Center, Greenbelt, Maryland, 1990.

Bowhill, S. A., and E. R. Dyer, eds., <u>The Upper Atmosphere</u>, D. Reidel Publishing, 1972.

Breig, E. L., "Thermospheric ion and neutral composition and chemistry," Rev. Geophys., 25, #3, 455, 1987.

Brenton, J. G., and S. M. Silverman, "A study of the diurnal variations of the 5577 Å [OI] airglow emission at selected IGY stations," Planet. Sp. Sci., 8, 641, 1970.

Broadfoot, A. Lyle, "Spectral Analysis of the Shuttle Glow: AIS Experiment Science Report," PL-TR-92-2172, Phillips Laboratory, Air Force Systems Command, Hanscom Air Force Base, Massachusetts, 1992.

Broadfoot, A. Lyle, and Kenneth R. Kendall, "The airglow spectrum, 3100-10,000 Å," J. Geophys. Res., 73, #1, 426, 1968.

Broadfoot, A. Lyle, and B. R. Sandel, "Application of the intensified CCD to airglow and auroral measurements," Applied Optics, 31, #16, 3097, 1992.

Broadfoot, A. Lyle, B. R. Sandel, D. J. Knecht, R. Viereck, and E. Murad, "Panchromatic spectrograph with supporting monochromatic imagers," Applied Optics, 31, #16, 3083, 1992.

Burrage, M. D., N. Arvin, W. R. Skinner, and P. B. Hays, "Observations of the O_2 atmospheric band nightglow by the High Resolution Doppler Imager," J. Geophys. Res., 99, #A8, 15017, 1994.
Chamberlain, Joseph W., Theory of Planetary Atmospheres, Academic Press, 1978.

Chamberlain, Joseph W., Physics of the Aurora and Airglow, Classics in Geophysics, American Geophysical Union, 1995.

Chamberlain, Joseph W., and Donald M. Hunten, Theory of Planetary Atmospheres, 2nd Edition, Academic Press, 1987.

Chapman, Sydney, "History of Aurora and Airglow," in Aurora and Airglow, Billy M. McCormac, editor, Reinhold Publishing, 1967.

Cogger, L. L., and R. Khaneja, "Characteristics of the midlatitude maximum in the OI 5577 Å airglow emission rate," Can. J. Phys., 57, 926, 1979.

Dasch, Cameron J., "One-dimensional tomography: a comparison of Abel, onion-peeling, and filtered backprojection methods," Applied Optics, 31, #8, 1146, 1992.

Dewan, E. M., and R. E. Good, "Saturation and the 'universal' spectrum for vertical profiles of horizontal scalar winds in the atmosphere," J. Geophys. Res., 91, 2742, 1986.

Donahue, T. M., B. Guenther, and R. J. Thomas, "Distribution of atomic oxygen in the upper atmosphere deduced from Ogo 6 airglow observations," J. Geophys. Res., 78, 6662, 1973.

Farley, D. T., and B. B. Balsley, "Instabilities in the equatorial electrojet," J. Geophys. Res., 78, 227, 1973.

Forbes, J. M., "Tidal and planetary waves," in The Upper Mesosphere and Lower Thermosphere: A Review of Experiment and Theory, Johnson and Killeen, eds., Geophysical Monograph 87, American Geophysical Union, Washington D.C., 1995.

Forbes, J. M., R. G. Roble, and C. G. Fesen, "Acceleration, heating, and compositional mixing of the thermosphere due to upward propagating tides," J. Geophys. Res., 98, 311, 1993.

Frederick, J. E., "Influence of gravity wave activity on lower thermospheric photochemistry and composition," Plan. Sp. Sci., 27, 1469, 1979.

Fritts, David C., Robert C. Blanchard, and Lawrence Coy, "Gravity wave structure between 60 and 90 km inferred from Space Shuttle reentry data," J. Atm. Sci., 46, #3, 423, 1989.

Garcia, R. R., and S. Solomon, "A numerical model of the zonally averaged dynamical and chemical structure of the middle atmosphere," J. Geophys. Res., 88, 1379, 1983.

Gardner, Chester S., "Diffusive filtering theory of gravity wave spectra in the atmosphere," J. Geophys. Res., 99, 20601, 1994.

Gardner, Chester S., "Testing theories of atmospheric gravity wave saturation and dissipation," J. Atm. Terr. Phys., 58, #14, 1575, 1996.

Gattinger, R. L., "Interpretation of Airglow in Terms of Excitation Mechanisms: D Region Nightglow," in The Radiating Atmosphere, Billy M. McCormac, editor, D. Reidel Publishing, 1971.

Hargreaves, John K., The Solar-Terrestrial Environment, Cambridge University Press, 1992.

Hassani, Sadri, Foundations of Mathematical Physics, Allyn & Bacon, 1991.

Hedin, A. E., "MSIS-86 thermospheric model," J. Geophys. Res., 92, 4649, 1987.

Hedin, A. E., "Extension of the MSIS thermospheric model into the middle and lower atmosphere," J. Geophys. Res., 96, 1159, 1991.

Herzberg, Gerhard, Atomic Spectra and Atomic Structure, Dover, 1944.

Herzberg, Gerhard, Molecular Spectra and Molecular Structure, Volume I: Spectra of Diatomic Molecules, 2d Edition, Krieger Publishing, 1950.

Herzberg, Gerhard, The Spectra and Structures of Simple Free Radicals: An Introduction to Molecular Spectroscopy, Dover, 1971.

Hickey, Michael P., G. Schubert, and R. L. Walterscheid, "Gravity wave-driven fluctuations in the O_2 Atmospheric (0-1) nightglow from an extended, dissipative emission region," J. Geophys. Res., 98, #A8, 13717, 1993.

Hines, Colin O., "Geomagnetism and the Ionosphere," in Proceedings of the International Conference on the Ionosphere, The Institute of Physics and the Physical Society, London, 1963.

Hines, Colin O., ed., The Upper Atmosphere in Motion, Geophysical Monograph 18, American Geophysical Union, Washington D.C., 1974.

Huber, Klaus-Peter, and Gerhard Herzberg, Molecular Spectra and Molecular Structure, Volume IV: Constants of Diatomic Molecules, Van Nostrand Reinhold, 1979.

Hunten, Donald M., "Airglow -- Introduction and Review," in The Radiating Atmosphere, Billy M. McCormac, editor, D. Reidel Publishing, 1971.

Jackson, J. D., Classical Electrodynamics, John Wiley and Sons, Inc., 1975.

Johnston, Jeffrey E., Spectroscopic Observations of the Night Airglow from 3000 Å to 9200 Å, Ph.D. Dissertation, University of Arizona, 1992.

Johnston, Jeffrey E., and A. Lyle Broadfoot, "Midlatitude observations of the night airglow: implications to quenching near the mesopause," J. Geophys. Res., 98, #A12, 21593, 1993.

Kendall, D. J. W., E. J. Llewellyn, M. R. Gale, S. B. Mende, G. R. Swenson, and R. L. Gattinger, "High-resolution spectroscopic measurements from the Space Shuttle: orbiter glow and atmospheric emissions," Can. J. Phys., 69, 1209, 1991.

Kita, K., N. Iwagami, and T. Ogawa, "Rocket observations of oxygen night airglows: excitation mechanisms and oxygen atom concentration," Planet. Sp. Sci., 40, #9, 1269, 1992.

Knecht, D. J., E. Murad, R. Viereck, C. P. Pike, A. L. Broadfoot, E. R. Anderson, D. B. Hatfield, T. C. Stone, and B. R. Sandel, "The Arizona Airglow Experiment as flown on four Space Shuttle missions," in press, 1997.

Lagos, C. Pablo, "Note on the Mechanism of the 5577 OI Nightglow Emission at 100 km," in Atmospheric Emissions, Billy M. McCormac, editor, Reinhold Book Corporation, 1969.

López-González, M. J., J. J. López-Moreno, and R. Rodrigo, "Altitude profiles of the Atmospheric system of O_2 and of the green line emission," Planet. Sp. Sci., 40, #6, 783, 1992a.

López-González, M. J., J. J. López-Moreno, and R. Rodrigo, "Altitude and vibrational distribution of the O_2 ultraviolet nightglow emissions," Planet. Sp. Sci., 40, #7, 913, 1992b.

López-González, M. J., J. J. López-Moreno, and R. Rodrigo, "Atomic oxygen concentrations from airglow measurements of atomic and molecular oxygen emissions in the nightglow," Planet. Sp. Sci., 40, #7, 929, 1992c.

López-González, M. J., J. J. López-Moreno, and R. Rodrigo, "The altitude profile of the Infrared Atmospheric system of O_2 in twilight and early night: derivation of ozone abundances," Planet. Sp. Sci., 40, #10, 1391, 1992d.

McDade, I. C., "The Altitude Dependence of the OH ($X^2\Pi$) Vibrational Distribution in the Nightglow: Some Model Expectations," Planet. Sp. Sci., 39, #7, 1049, 1991.

McDade, I. C., and E. J. Llewellyn, "Rocket measurements of the O_2 Infrared Atmospheric (0,0) band in the nightglow: the vestigial day components," in Progress in Atmospheric Physics, Rodrigo, López-Moreno, López-Puertas, and Molina, editors, Kluwer Academic Publishers, 1988.

McDade, I. C., W. E. Sharp, P. G. Richards, and D. G. Torr, "On the inversion of $O^+(^2D-^2P)$ 7320 Å twilight airglow observations: a method for recovering both the ionization frequency and the thermospheric oxygen atom densities," J. Geophys. Res., 96, #A1, 259, 1991.

McEwen, D. J., and D. A. Harrington, "Polar airglow and aurora," Can. J. Phys., 69, 1055, 1991.

McLandress, C., Y. Rochon, G. G. Shepherd, B. H. Solheim, G. Thuillier, and F. Vial, "The meridional wind component of the thermospheric tide observed by WINDII on UARS," Geophys. Res. Lett., 21, #22, 2417, 1994.

Meier, R. R., "Thermospheric aurora and airglow," Rev. Geophys., 25, #3, 471, 1987.

Meier, R. R., "Ultraviolet spectroscopy and remote sensing of the upper atmosphere," Sp. Sci. Rev., 58, nos. 1/2, 1, 1991.

Mende, S. B., G. R. Swenson, S. P. Geller, R. A. Viereck, E. Murad, and C. P. Pike, "Limb view spectrum of the Earth's airglow," J. Geophys. Res., 98, #A11, 19117, 1993.

Mlynczak, Martin G., Susan Solomon, and Daphne S. Zaras, "An updated model for O_2 $(a^1\Delta_g)$ concentrations in the mesosphere and lower thermosphere and implications for remote sensing of ozone at 1.27 mm," J. Geophys. Res., 98, #D10, 18639, 1993.

Murtagh, Donal P., "The state of O_2 in the Mesopause Region," in The Upper Mesosphere and Lower Thermosphere: A Review of Experiment and Theory, Johnson and Killeen, eds., Geophysical Monograph 87, American Geophysical Union, Washington D.C., 1995.

Neupert, Werner M., Gabriel L. Epstein, James Houston, Kenneth J. Meese, William S. Muney, Thomas B. Plummer, and Frank P. Russo, "The Orbiter Stability Experiment on STS-40," unpublished manuscript, Laboratory for Astronomy and Solar Physics, NASA Goddard Space Flight Center, 1992.

Noxon, John F., "Interpretation of F Region Nightglow," in The Radiating Atmosphere, Billy M. McCormac, editor, D. Reidel Publishing, 1971.

O'Brien, B. J., F. R. Allum, and H. C. Goldwire, "Rocket measurement of midlatitude airglow and particle precipitation," J. Geophys. Res., 70, 161, 1965.

Omholt, A., "The red and near-infrared auroral spectrum," J. Atm. Terr. Phys., 10, 320, 1957.

Omholt, A., "The Spectrum and Excitation Mechanisms in Aurora," in Aurora and Airglow, Billy M. McCormac, editor, Reinhold Publishing, 1967.

Omholt, A., The Optical Aurora, Springer-Verlag, 1971.

Rees, M. H., Physics and Chemistry of the Upper Atmosphere, Cambridge University Press, 1989.

Roble, R. G., and P. B. Hays, "A technique for recovering the vertical number density profile of atmospheric gases from planetary occultation data," Planet. Sp. Sci., 20, 1727, 1972.

Roble, R. G., and G. G. Shepherd, "An analysis of wind imaging interferometer observations of $O(^1S)$ equatorial emission rates using the thermosphere-ionosphere-mesosphere-electrodynamics general circulation model," J. Geophys. Res., 102, #A2, 2467, 1997.

Rodrigo, R., J. J. López-Moreno, M. López-Puertas, and A. Molina, editors, Progress in Atmospheric Physics, Kluwer Academic Publishers, 1988.

Rodrigo, R., J. J. López-Moreno, M. López-Puertas, F. Moreno, and A. Molina, "Neutral atmospheric composition between 60 and 220 km: a theoretical model for mid-latitudes," Planet. Sp. Sci., 34, #8, 723, 1986.

Rodrigo, R., M. J. López-González, and J. J. López-Moreno, "Variability of the neutral mesospheric and lower thermospheric composition in the diurnal cycle," Planet. Sp. Sci., 39, #6, 803, 1991.

Sharma, R. D., "Infrared Airglow," in Progress in Atmospheric Physics, Rodrigo, López-Moreno, López-Puertas, and Molina, editors, Kluwer Academic Publishers, 1988.

Shepherd, G. G., G. Thuillier, B.H. Solheim, Y. J. Rochon, J. Criswick, W. A. Gault, R. N. Peterson, R. H. Wiens, and S.-P. Zhang, "WINDII on UARS - status report and preliminary results," in The Upper Mesosphere and Lower Thermosphere: A Review of Experiment and Theory, Johnson and Killeen, eds., Geophysical Monograph 87, American Geophysical Union, Washington D.C., 1995a.

Shepherd, G. G., C. McLandress, and B. H. Solheim, "Tidal influence on $O(^1S)$ airglow emission rate distributions at the geographic equator as observed by WINDII," Geophys. Res. Lett., 22, #3, 275, 1995b.

Shepherd, G. G., G. Thuillier, B. H. Solheim, S. Chandra, L. L. Cogger, M. L. Duboin, W. F. J. Evans, R. L. Gattinger, W. A. Gault, M. Herse, A. Hauchecorne, C. Lathuilliere, E. J. Llewellyn, R. P. Rowe, H. Teitelbaum, and F. Vial, "Longitudinal structure in atomic oxygen concentrations observed with WINDII on UARS," Geophys. Res. Lett., 20, #12, 1303, 1993.

Silverman, Sam M., "Night Airglow Phenomenology," in <u>Atmospheric Emissions</u>, Billy M. McCormac, editor, Reinhold Book Corporation, 1969.

Solomon, S. C., P. B. Hays, and V. J. Abreu, "The auroral 6300 Å emission: observations and modeling," J. Geophys. Res., 93, 9867, 1988.

Stegman, J. and D. P. Murtagh, "The molecular oxygen band systems in the U.V. nightglow: measured and modelled," Planet. Sp. Sci., 39, #4, 595, 1991.

Swenson, G. R., and S. B. Mende, "OH emission and gravity waves (including a breaking wave) in all-sky imagery from Bear Lake, UT," Geophys. Res. Lett., 21, #20, 2239, 1994.

Swenson, G. R., and P. J. Espy, "Observations of 2-dimensional airglow structure and Na density from the ALOHA, October 9, 1993, 'storm flight'," Geophys. Res. Lett., 22, #20, 2845, 1995.

Swenson, G. R., M. J. Taylor, P. J. Espy, C. Gardner, and X. Tac, "ALOHA-93 measurements of intrinsic AGW characteristics using airborne airglow imager and groundbased Na wind/temperature lidar," Geophys. Res. Lett., 22, #20, 2841, 1995.

Swenson, G. R., S. B. Mende, and E. J. Llewellyn, "Imaging observations of lower thermospheric $O(^1S)$ and O_2 airglow emissions from STS 9: implications of height variations," J. Geophys. Res., 94, #A2, 1417, 1989.

Takahashi, H., P. P. Batista, Y. Sahai, and B. R. Clemesha, "Atmospheric wave propagations in the mesopause region observed by the OH (8,3) band, O_2 A (8645 Å) band, and O I 5577 Å nightglow emissions," Plan. Sp. Sci., 33, #4, 381, 1985.

Takahashi, H., Y. Sahai, B. R. Clemesha, D. M. Simonich, N. R. Teixeira, R. M. Lobo, and A. Eras, "Equatorial mesospheric and F-region airglow emissions observed from latitude 4° south," Plan. Sp. Sci., 37, 649, 1989.

Tatum, J. B., "The interpretation of intensities in diatomic molecular spectra," Astrophys. J., XIV, #124, 21, 1967.

Taylor, M. J., M. B. Bishop, and V. Taylor, "All-sky measurements of short period waves imaged in the O I (557.7 nm), Na (589.2 nm), and near infrared OH and O_2 (0,1) nightglow emissions during the ALOHA-93 campaign," Geophys. Res. Lett., 22, #20, 2837, 1995.

Taylor, M. J., D. C. Fritts, and J. R. Isler, "Determination of horizontal and vertical structure of an unusual pattern of short period gravity waves imaged during ALOHA-93," Geophys. Res. Lett., 22, #20, 2837, 1995.

Taylor, M. J., M. A. Hapgood, and P. Rothwell, "Observations of gravity wave propagation in the O I (557.7 nm), Na (589.2 nm), and the near infrared OH nightglow emissions," Plan. Sp. Sci., 35, #4, 413, 1987.

Thomas, Lance, "Ionospheric Phenomena Related to the Airglow," in Atmospheric Emissions, Billy M. McCormac, editor, Reinhold Book Corporation, 1969.

Tohmatsu, Takao, Compendium of Aeronomy, Terra Scientific Publishing Company, Kluwer Academic Publishers, 1990.

Torr, Marsha R., and D. G. Torr, "The role of metastable species in the thermosphere," Rev. Geophys. Sp. Phys., 20, #1, 91, 1982.

Turnbull, D. N., and R. P. Lowe, "New hydroxyl transition probabilities and their importance in airglow studies," Plan. Sp. Sci., 37, #6, 723, 1989.

Vallance Jones, Alister, Aurora, D. Reidel Publishing, 1974.

Viereck, R. A., "A review of mesospheric dynamics and chemistry," Rev. Geophys. Supplement, 1132, April 1991.

Viereck, R. A., and C. S. Deehr, "On the interaction between gravity waves and the OH Meinel (6-2) and the O_2 Atmospheric bands in the polar night airglow," J. Geophys. Res., 94, #A5, 5397, 1989.

Viereck, R. A., D. J. Knecht, A. L. Broadfoot, and B. R. Sandel, "The AIS, A Spectrograph/Imager Ensemble for Space Flight," GL-TR-90-0158, Space Physics Division, Geophysics Laboratory, Hanscom Air Force Base, Massachusetts, 1990.

Ward, W. E., E. J. Llewellyn, Y. Rochon, C.C. Tai, W. S. C. Brooks, B. H. Solheim, and G. G. Shepherd, "Spatial variability in $O(^1S)$ and $O_2(b^1\Sigma_g^+)$ emissions as observed with the Wind Imaging Interferometer (WINDII) on UARS," in The Upper Mesosphere and Lower Thermosphere: A Review of Experiment and Theory, Johnson and Killeen, eds., Geophysical Monograph 87, American Geophysical Union, Washington D.C., 1995.

Wasser, B., and T. M. Donahue, "Atomic oxygen between 80 and 120 km: Evidence for a latitudinal variation in vertical transport near the mesopause," J. Geophys. Res., 84, 1297, 1979.

Weill, G. M., "Airglow Observations Near the Equator," in Aurora and Airglow, Billy M. McCormac, editor, Reinhold Publishing, 1967.

Wertz, James R., and Wiley J. Larson, eds., Space Mission Analysis and Design, Kluwer Academic Publishers, 1991.

Yee, J. H., and V. J. Abreu, "Mesospheric 5577 Å green line and atmospheric motions - Atmospheric Explorer satellite observations," Plan. Sp. Sci., 35, 1389, 1987.